Dispositifs électrooptique assistés plasmon en silicium

Siddhath Nambiar

To cite this version:

Siddhath Nambiar. Dispositifs électrooptique assistés plasmon en silicium. Autre [cond-mat.other]. Université de Grenoble, 2012. Français. NNT : 2012GRENY099 . tel-00845672

UNIVERSITÉ DE GRENOBLE

THÈSE

Pour obtenir le grade de

DOCTEUR DE L'UNIVERSITÉ DE GRENOBLE

Spécialité : **Nanophysique**

Arrêté ministériel : 7 août 2006

Présentée par

Siddharth NAMBIAR

Thèse dirigée par **Marc SANQUER**
et co-encadrée par **Roch ESPIAU de LAMAESTRE**

préparée au sein **Département d'Optronique (DOPT) CEA-LETI**
dans **l'École Doctorale de Physique de Grenoble**

Dispositifs électro optique assistés plasmon en silicium

Thèse soutenue publiquement le **20 decembre 2012**,
devant le jury composé de :

Dr. Kuntheak KHENG
Professeur, Université Joseph Fourier, Président
Dr. Renaud BACHELOT
Directeur du LNIO, Université de Technologie de Troyes, Rapporteur
Dr. Alexandre BOUHELIER
HDR Chercheur, Université de Bourgogne, Rapporteur
Dr. Laurent VIVIEN
CNRS Researcher, IEF Paris Sud, Examinateur
Dr. Marc SANQUER
Chef de laboratoire, LaTEQS CEA-INAC, Directeur de thèse
Dr. Roch ESPIAU de LAMAESTRE
Docteur-Ingenieur, CEA-LETI, Co-encadrant de thèse

Acknowledgement

First of all I'd like to express my sincere gratitude to my thesis supervisor Dr. Roch Espiau de Lamaestre for his invaluable guidance and constant encouragement to complete this work. I have very much benefited from his intelligence, critical thinking, creativity and rigorous approach to science. I am thankful for your patience and high expertise in field of plasmonics. I have enjoyed working with you.

I am also grateful to my director Dr. Marc Sanquer who inspite of his busy schedule always made time for individual meetings to discuss about the progress and problem of projects and always gave his invaluable guidance and suggestions.

My sincere thanks to Dr. Renaud Bachelot and Dr. Alexandre Bouhelier for accepting to be my reviewers. Their insightful comments and suggestions have definitely helped to improve my dissertation.

I'd like to acknowledge the financial assistance provided by the Fondation Nanoscience under the RTRA grant which has enabled me to pursue research in such a world class facility.

I'd also like to express my thanks to Dr. Salim Boutami for his constructive inputs in implementing the BEM technique. Salim was always forthcoming for any discussion, academic and likewise. It was a pleasure working with him.

A special note of thanks to Dr. Alain Gliere for his valuable assistance in dealing with cluster related issues.

Thanks a lot to my colleagues, Alexandros, Clement and Aparna as well as others who have made my stay here in France most memorable and unforgetable.

Finally I express my deepest gratitude to my parents and family for their strong faith and moral support which enabled me to take up the challenge of pursuing research abroad.

Contents

Acronyms

SPPs	Surface plasmon polaritons
CMOS	Complementary Metal Oxide Semiconductor
EM	Electromagnetic
TE	Transverse Electric
TM	Transverse Magnetic
IC	Integrated Circuit
BEM	Boundary Element Method
FEM	Finite Element Method
FDTD	Finite Difference Time Domain
FIT	Finite Integration Technique
MoM	Method of Moments
PML	Perfectly Matched Layer
SOI	Silicon on Insulator
MOS	Metal Oxide Semiconductor
DLSPPs	Dielectric loaded SPPs
MIM	Metal Insulator Metal
MISM	Metal Insulator Semiconductor Metal
$\mathbf{N_{eff}}$	Effective Index
FP	Fabry Perot
MMI	Multimode Interference
EA	Electro-absorption
FCPD	Free Carrier Plasma Dispersion
MZI	MachZehnder interferometer
FK	Franz Keldysh

MD	Modulation Depth
LSPRs	Localized Surface Plasmon Resonances
PD	Photodetector

Chapter 1

Introduction

The rapid progress of optical communication systems in the last twenty years has sparked a wide interest in the field of photonics. As a result of increasing need for broadband facilities, optical fibers now, form the backbone of current high speed data transmission networks. When compared to electron transport in semiconductor ICs, photonic systems exhibit lower heat dissipation, better cross-talk tolerance and enormous bandwidth capacity at optical frequencies. This remarkable ability of optical fibers to transmit signals has led researchers to explore the possibility of replacing electronic ICs with photonic processors. Moreover, building photonic chip interconnects with all optical processing may offer a long term solution to the problem of bottleneck in microelectronics, which may soon reach their physical limit in speed as indicated by Moore's law.

Crucial to realising the goal of building photonic circuits is to have a reliable optical design for processing elements such as modulators, detectors, multiplexers, chip integrated sources etc. While some of these elements have already been demonstrated, the possibility of integrating them at chip level remains elusive. This is due to the fact that owing to the diffraction limit constraints, the size required to confine the optical field scales with the wavelength and hence is of several μm dimensions. One way to bridge this size gap can be to use surface plasmons to channel light. The surface plasmons polaritons(SPPs) are coherant oscillations of conduction electrons on a metal dielectric interface that are excited by an electromagnetic field. Surface plasmons can overcome the diffraction limit by channeling electromagnetic energy into sub-wavelength volumes. The plasmon modes are strongly bound to the interface and exponentially decay in a direction normal to it. This confinement of light into small volumes in metallic nanostructures can provide for large enhancements of local electromagnetic fields which can be useful for probing a number of linear and non-linear optical effects.

The past decade, has seen enormous research activity in this domain due to its potential applications encompassing several domains. The unique properties of surface plasmons has been demonstrated in some of these such as enhanced Raman scattering(SERS)[1, 2], fluoroscence sensing[3–9], photovoltaics[10, 11] and many more. The strong field enhancement provided by plasmons may be used to probe many weak effects, that were hitherto not possible. This period also coincides with significant advances in the arena of nanofabrication tehniques, which has led to the realization of nanostructures with precise control over varied shapes, sizes and spacings. Yet however considerable hurdles remain to achieve near total chip level integration of these components.

1.1 Need for Silicon photonics

Si based photonic components working in the C-band range of 1.3-1.55μm wavelengths has always been a topic of intense research. The SOI platform of CMOS photonics with its high optical confinement due index contrast and extremely low losses(0.2-0.3 dB/cm)[12], as well as compatibility with mature CMOS fabrication technology, is a leading choice of integrated optics technology that can deliver large communication bandwidth, low latency along with low power consumption for chip level interconnects(fig. 1.1). Several key passive building elements, including low loss waveguides bends, routers, wavelength multiplexers, and fiber grating couplers have been successfully demonstrated using CMOS compatible processes. However, in part due to its indirect band structure, the goal of developing Si-based active photonic devices has been particularly challenging. Si having a higher bandgap, is fairly transparent in this frequency range. As far as active devices, such as source, modulators are concerned, devices based on III-V materials remain the best performing candidates. Unlike silicon, these compound materials have a direct band-gap, which can also be tuned depending on their chemical composition. In spite of this, III Vs have yet not emerged as the preferred choice for large scale integration of nanophotonic circuits. The answer lies in the economics of fabrication. Monolithic integration of circuits is much more difficult and expensive to achieve with III Vs than with silicon. III-V semiconductors present different processing challenges and material complexities than silicon and economically producing integrated devices in volume is a major issue. Another drawback is the non-availability of high quality oxides and issues of purity of compound materials. Due

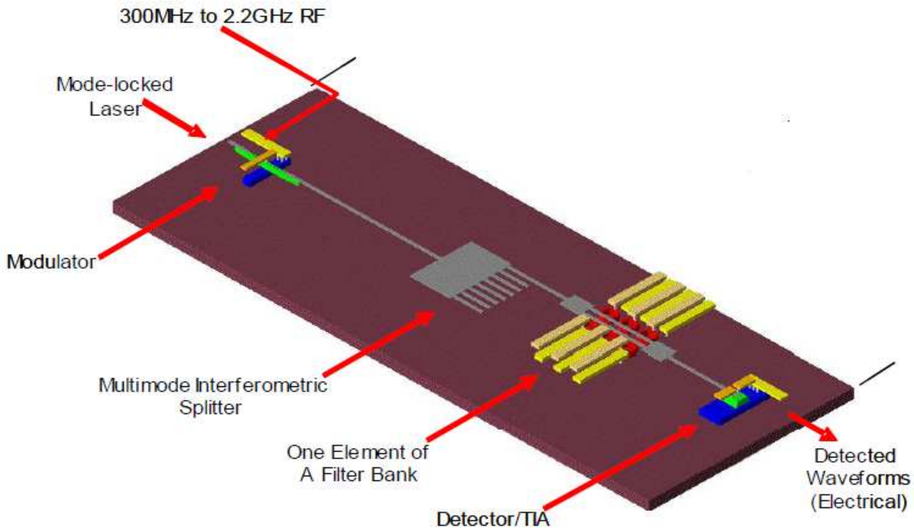

Figure 1.1: *Schematic of a single optical channeliser link on a hybrid electronic photonic integrated circuit.(adopted from[13])*

to these aforementioned reasons, optoelectronic devices would continue to be designed using Si based components.

The problem of platform combatibility can be addressed in two ways i.e either by bonding III-Vs on Si, or by using other CMOS materials such as Ge. As an example in the case of light sources, an InP based device has been developed by the PICMOS consortium(of which CEA Leti is a partner)[14] by first bonding it to Si and then processing it to a microdisk laser. In case of latter, both erbium coupled Si nanocrystals[15] as well as highly doped tensile strained Ge[16] are now regarded as potential candidates for near infra-red light emission.

1.2 Plasmonics

The above factors mean that Si-based technology will remain as the back bone of any optical integrated solution. The challenge is to use this technology to build compact power efficient photonic circuits. Using plasmon based Si photonic elements, optical interconnects can be scaled down to nanoscale dimensions that are compatible with current Si electronic devices[17–19]. The highly localised nature of plasmon modes is remarkably different from photonic modes in dielectric guides and presents a new means of channeling optical signals. Furthermore, unlike in electronic circuits, the use of metal

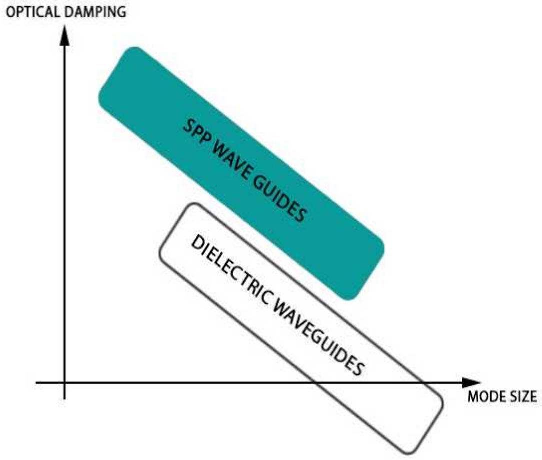

Figure 1.2: *Comparison between photonic and plasmonic waveguides.*

in plasmonic waveguides would not contribute to an increase in RC delay times. Also the current front-end line of techniques is capable of depositing nanoscale metallic features of Al and Cu interconnects on Si which may be useful to integrate both dielectric and plasmonic waveguides. A typical hybrid photonic-plasmonic interconnect would consist of photonic guides to transmit optical signals between various circuits, passive plasmonic elements such as waveguides, routers, multiplexers to transmit these signals within a circuit, active plasmonic elements such as modulators to encrypt the data stream, photodetectors to convert the incoming light into electrical signal.

A key issue when dealing with plasmon based components is the unavoidable damping of metals at optical frequencies. For certain plasmon based waveguide structures such as MIM, MISM, this damping could be as high as several dB/microns. The effect of this damping enabled losses especially needs to be considered while desigining high speed compact active devices whereby a critical tradeoff necessary between losses and mode confinement(see fig. 1.2). This unavoidable losses means that plasmon based components are not wholly expected to replace their photonic counterparts but instead supplement them in a optical integrated circuit. Furthermore, it must be pointed out that it is difficult to implement a waveguide configuration that combines a system supporting nanoscale SPP modes that can be readily coupled to photonic modes. A clear understanding is still lacking to define the propagation characteristics of these SPP modes in various waveguide geometries. Out of the several plasmon guide geometries, the metal oxide semiconductor(MOS) configuration is particularly interesting due to its platform compatibility and low loss features. There is tremendous potential to develop this design as an alternative to passive photonic elements in an integrated circuit. This MOS design has been extensively analyzed and discussed in the third chapter.

Active elements like modulators also form a vital link for integration. Here compact plasmonic designs are more favourable due to the benefit of low power consumption. Standard electro-optic modulation mechanisms in Si are however are weak and require the devices to be of several hundred microns length. It has recently been shown in several works that Ge can provide a strong electroabsorption in the near infrared region. When combined with a highly confining plasmonic structure, a compact modulator could readily be developed. To that end, chapter four reviews the different semiconductor modulation schemes that have been implemented and analyses a probable plasmon based Ge modulator design that could be incorporated in a photonic circuit.

A photodetector is another active component of an optoelectronic circuit that transforms the incident light into electrical signals. Generally here too III-V materials are preferred due to their strong absorption in the near infrared region. However due to the aforementioned reasons Ge based detectors are favoured even though they have a low absorption cross section which means increasing the detector size. One way to address the size problem is by squeezing light into nanoscale using plasmons. Chapter five discusses a novel approach to design a plasmon assisted nanoantenna based Ge photodetector.

1.3 Metals at optical frequencies

Metals are widely used for designing as waveguides and resonators for Rf and microwave applications. In this region of electromagnetic spectrum, the attenuation of EM fields inside the metal layer is negligible, and so they can be assumed to have perfect conductor behaviour. However, in the near-infra red to visible part of the spectrum, the field penetration increases significantly. The complex dielectric properties of metals in this regime can be readily described within the framework of Maxwell's equations by the employing the Drude model, where free electrons of density N and effective mass m move through a periodic array of positive cores[21]. The high density of free carriers in metals results in negligible electron energy level spacing as compared to the thermal excitations k_BT. These electrons oscillate about the more heavy positive ion cores, when impacted upon by an external EM field. This oscillation is damped due to collision with the positive cores with a collision frequency $\gamma = \frac{1}{\tau}$, τ being the free electron relaxation time. The frequency ω of these longtitudinal fluctuations is related to its wave-vector k by its dispersion relation $\omega(k)$. The charged electron oscillations are localised in a direction normal to the interface with a maximum at the interface. The electron motion in a sea of plasma driven by an external electric field $\mathbf{E}$ can be described by the following equation:

$$m\frac{d^2x}{dt^2} + m\gamma\frac{dx}{dt} = -e\mathbf{E} \tag{1.1}$$

where x is the electron displacement about the core position. Assuming an explicit time dependence for both the applied field $\mathbf{E}(t) = \mathbf{E}_0e^{-i\omega t}$ as well as the displacement $\mathbf{x}(t) = x_0e^{i\omega t}$, so that the above equation results in:

$$\mathbf{x}(t) = \frac{e}{m(\omega^2 + i\gamma\omega)}\mathbf{E}(t) \tag{1.2}$$

The displaced electrons lead to a polarization $\mathbf{P} = -ne\mathbf{x}$, espressed as:

$$\mathbf{P} = -\frac{ne^2}{m(\omega^2 + i\gamma\omega)}\mathbf{E} \tag{1.3}$$

Since the electric displacement vector $\mathbf{D} = \epsilon_0\mathbf{E} + \mathbf{P}$, inserting the above relation for P, we have:

$$\mathbf{D} = \epsilon_0\left(1 - \frac{\omega_p^2}{\omega^2 + i\gamma\omega}\right)\mathbf{E} \tag{1.4}$$

Here $\omega_p^2 = \frac{ne^2}{\epsilon_0 m}$ denotes the bulk plasma frequency of free-electron gas. The complex dielectric function of the metal can now be expressed as:

$$\epsilon(\omega) = 1 - \frac{\omega_p^2}{\omega^2 + i\gamma\omega} \tag{1.5}$$

Seperating the real and imaginary part of this function as $\epsilon = \epsilon' + i\epsilon''$ we obtain:

$$\epsilon'(\omega) = 1 - \frac{\omega_p^2 \tau^2}{1 + \omega^2 \tau^2} \tag{1.6}$$

$$\epsilon''(\omega) = \frac{\omega_p^2 \tau}{\omega(1 + \omega^2 \tau^2)} \tag{1.7}$$

At large freqencies close to the ω_p, the term $\omega\tau >> 1$ thereby leading to negligible attenuation and the dielectric function becomes predominantly real

$$\epsilon(\omega) = 1 - \frac{\omega_p^2}{\omega^2} \tag{1.8}$$

ω_p is the characteristic plasma frequency above which the dielectric constant of the metal becomes positive and it behaves like a dielectric.

Generally speaking the Drude model is fairly accurate for metals from the infra red to visible regime. Above the boundary of this region however, interband transitions begin to take precedence, leading to an increase in ϵ''. This region is better described by the Lorentz-Drude, model which is a good approximation for dispersive materials having multiple resonant frequencies that takes into account both inter and intraband transitions.

1.4 Plasmons on a metal dielectric Interface

At the interface of a metal and a dielectric, longtitudinal surface plasmons can be excited by an time varying incident EM field. The dispersion relationship of these plasmons can be very well obtained by solving the Maxwell's equations and applying appropriate boundary conditions for the two mediums. The Maxwell's equations for an isotropic, linear, homogenous medium is expressed as:

$$\begin{aligned} \nabla.\mathbf{D} &= \rho && (1.9a) \\ \nabla.\mathbf{B} &= 0 && (1.9b) \\ \nabla \times \mathbf{E} &= -\frac{\partial \mathbf{B}}{\partial t} && (1.9c) \\ \nabla \times \mathbf{H} &= \mathbf{J} + \frac{\partial \mathbf{D}}{\partial t} && (1.9d) \end{aligned}$$

Where $\mathbf{B} = \mu\mu_0\mathbf{H}$. For the simplified case of a charge and source free medium, $\rho = 0$ and $\mathbf{J} = 0$.

Now, taking the last two equations and replacing the expression for $\mathbf{B}$, we obtain the wave equation:

$$\nabla \times (\nabla \times \mathbf{E}) = -\mu_0 \frac{\partial^2 \mathbf{D}}{\partial t^2} \tag{1.10}$$

Which can be simplified further to:

$$\nabla^2 \mathbf{E} - \frac{\epsilon}{c^2}\frac{\partial^2 \mathbf{E}}{\partial t^2} = 0 \tag{1.11}$$

By taking out the dependence for time variance($\frac{\partial}{\partial t} = -i\omega$), the above equation leads to:

$$\nabla^2 \mathbf{E} + k_0^2 \epsilon \mathbf{E} = 0 \tag{1.12}$$

Where k_0 is the free space wave-vector.

TM Polarization

For any bounded mode that propagates along the interface, there must be a component of electric field normal to the interface. Since this criteria is fulfilled only for TM modes, plasmons cannot be excited by TE modes(having a transverse E field). Taking the case of a 1D problem, where the co-ordinate system is chosen with x as propagation direction and z to be the axis with varying dielectric constant($\epsilon = \epsilon(z)$) with z=0 defining the interface. The Maxwell's curl equations for TM waves, with transverse magnetic field

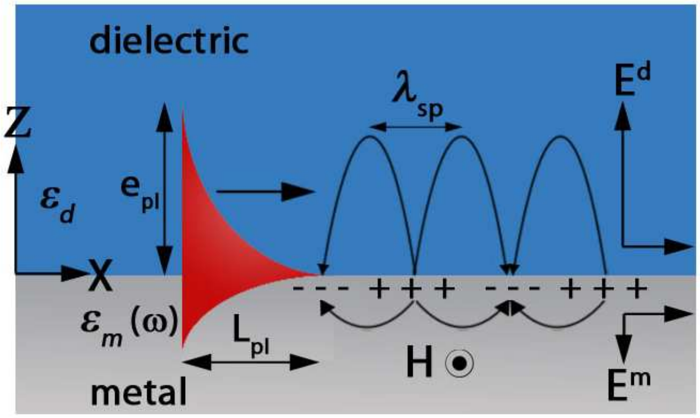

Figure 1.3: *Schematic representation of surface plasmon distribution at a metal dielectric interface.*

profile having H_y, E_z and E_x components is given as:

$$E_x = -i\frac{1}{\omega\epsilon_0\epsilon}\frac{\partial H_y}{\partial z} \tag{1.13}$$

$$E_z = -i\frac{1}{\omega\epsilon_0\epsilon}\frac{\partial H_y}{\partial x} \tag{1.14}$$

Since x is the propagation direction and $H_y(x,z) = H_y(z)e^{ik_x x}$, $\frac{\partial H_y}{\partial x} = ik_x H_y$. The wave-equation can now be written as:

$$\frac{\partial^2 H_y}{\partial z^2} + (k_0^2\epsilon - k_x^2)H_y = 0 \tag{1.15}$$

Solving for this equation, the corresponding field components for both dielectric($z > 0$) and metal($z < 0$) regions are given as:

$$H_y = H_0^d e^{ik_x x} e^{-k_d z} \tag{1.16}$$

$$E_x = iH_0^d \frac{1}{\omega\epsilon_0\epsilon_d} k_{zd} e^{ik_x x} e^{-k_{zd} z} \tag{1.17}$$

$$E_z = -H_0^d \frac{k_x}{\omega\epsilon_0\epsilon_d} e^{ik_x x} e^{-k_{zd} z} \tag{1.18}$$

in the dielectric region and

$$H_y = H_0^m e^{ik_x x} e^{k_m z} \tag{1.19}$$

$$E_x = iH_0^m \frac{1}{\omega\epsilon_0\epsilon_d} k_{zm} e^{ik_x x} e^{k_{zm} z} \tag{1.20}$$

$$E_z = -H_0^m \frac{k_x}{\omega\epsilon_0\epsilon_d} e^{ik_x x} e^{k_{zm} z} \tag{1.21}$$

in the metal region. k_d and k_m are the wavevectors in the z direction for the dielectric and metal regions respectively.

Continuity of the tangential field component H_y and the normal field component $\epsilon_i E_z^i$ leads to:

$$H_0^d = H_0^m \tag{1.22}$$

$$\frac{k_{zd}}{k_{zm}} = -\frac{\epsilon_d}{\epsilon_m} \tag{1.23}$$

The above relation seems to indicate that surface plasmons only exist at the interfaces of two mediums having dielectric constants with opposite sign. Hence only a metal-dielectric interface can support plasmon propagation. Replacing the value of H_y in the wave-equation in the two regions:

$$k_{zd}^2 = k_x^2 - k_0^2\epsilon_d \tag{1.24}$$

$$k_{zm}^2 = k_x^2 - k_0^2\epsilon_m \tag{1.25}$$

Solving for this equation, the dispersion relation for the propagation constant $k_x = k_{sp}$ can be derived as a function of the dielectric constants:

$$k_{sp(\omega)} = k_0\sqrt{\frac{\epsilon_d\epsilon_{m(\omega)}}{\epsilon_d + \epsilon_m}} \tag{1.26}$$

Now for a bounded mode, the normal component of propagation constants k_{zi} in both the mediums must be imaginary.

$$k_{zi}^2 = \frac{\omega}{c}^2 - k_x^2 < 0 \tag{1.27}$$

$$k_x^2 > \frac{\omega}{c}^2 \tag{1.28}$$

Which implies that the plasmon wave-vector for surface bounded modes will always be greater than the light wave-vector in a dielectric. Since in real metals, the dielectric constant is a complex quantity, there is always some loss associated with the plasmon wavevector $k_{sp} = k'_{sp} + ik''_{sp}$. In view of the fact that in most metals $|\epsilon''| < |\epsilon'|$, the real and imaginary part of the complex propagation constant can be expressed as:

$$\begin{aligned} k'_{sp} &= \frac{\omega}{c}\left(\frac{\epsilon'_m \epsilon_d}{\epsilon'_m + \epsilon_d}\right)^{\frac{1}{2}} \\ k''_{sp} &= \frac{\omega}{c}\left(\frac{\epsilon'_m \epsilon_d}{\epsilon'_m + \epsilon_d}\right)^{\frac{3}{2}} \frac{\epsilon''_m}{2\epsilon'^2_m} \end{aligned} \tag{1.29}$$

Conditions for the SPP mode to be bounded requires that the real part of the complex propagation constant be positive which leads to $Re\{\epsilon_d \epsilon_m\} < 0$ and $Re\{\epsilon_d + \epsilon_m\} < 0$. This condition is satisfied for most metals and dielectrics in the long wavelength part of the visible and infrared regions. The dispersion relation is depicted in the fig.1.4. For the small wavevector limit($\epsilon'_m >> \epsilon_d$), the plasmon wavelength is close to the light line. In the large wave-vector limit(where $\epsilon'_m \to \epsilon_d$), the plasmon wave-vector approaches the characteristic surface plasmon frequency $\omega_{sp} = \frac{\omega_p}{\sqrt{1+\epsilon_d}}$. Between the region of the bulk-plasma frequency ω_p and ω_{sp}, the plasmon wave-vector is purely imaginary and no propagation modes exist in this region. Above the range of the bulk plasma frequency($> \omega_p$), the metal behaves as a dielectric.

The plasmon propagation vector is primarily characterised by two quantities namely, the propagation length L_p and the the penetration depth e_{pl}. The propagation length is the distance, upto which the plasmon mode intensity is reduced to $\frac{1}{e}$ of its original value.

$$L_p = \frac{1}{2k''_{sp}} \tag{1.30}$$

Similarly, the plasmon penetration depth e_{pl} is the distance from the normal interface

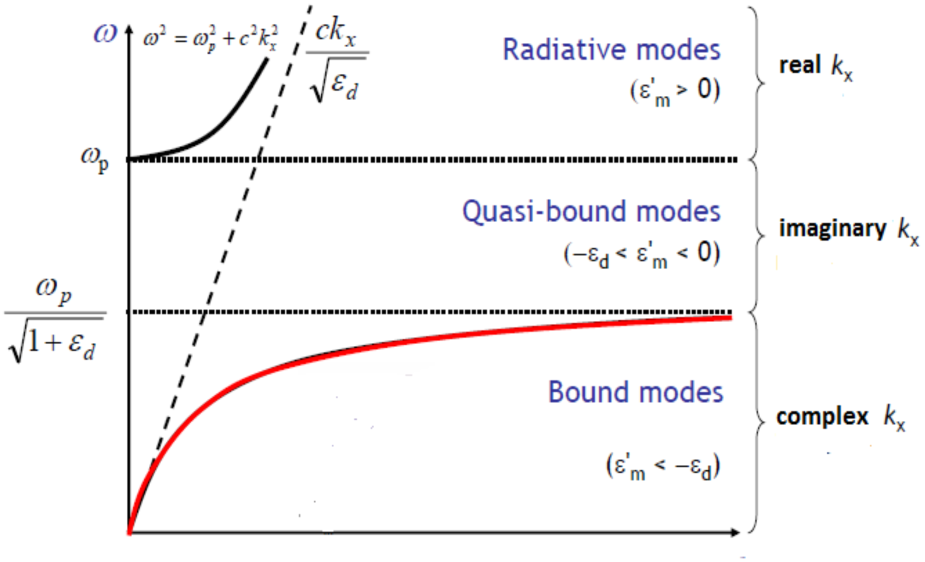

Figure 1.4: *The plasmon dispersion curve for different frequency regions.*

to where the plasmon mode intensity dreases to $\frac{1}{e}$ value.

$$e_{pl} = \frac{1}{2k''_z} \tag{1.31}$$

1.5 Plasmon Coupling

Since the plasmon wavevector lies right of the lightline, appropriate phase matching techniques are required to couple SPP waves at the interface. Some of these methods are briefly decribed below.

One of the earliest methods to facilitate this coupling was proposed by Andreas Otto[22]. Otto suggested that the incident free-space wavevector could be increased by propagating it in a high index dielectric. The field from this photon in a dielectric would then leak out through a thin layer of low index dielectric to couple to plasmon waves at the interface of a metal and this low index dielectric. The EM wave of p polarization is incident at an angle θ to a high index material which in this case is a prism and is refracted to its bottom surface. A low index dielectric spacer of thickness δ separates the prism bottom from a metal. At a certain angle of incidence θ, the incident wave will undergo total internal reflection and a leaky wave will be excited in the low index spacer. At appropriate energy and phase matching conditions, this leaky wave will excite a plasmon wave at the spacer-metal interface. The resulting energy loss due to the SPP coupling will then be detected in the reflected beam.

Another common method also using prism coupling is the Kretschmann and Raether configuration[23, 24]. In this method, the plasmon supporting thin film metal is deposited on the high index prism. Again under proper conditions, the incident light at an angle above the critical angle, will generate an evanescent tail having a longitudinal k vector along the metal film under the prism base that eventually penetrates and couples to the plasmon mode at metal-low index interface. The two prism coupling schemes are depicted in fig. 1.5. Yet another method to couple plasmons is through a metal grating fabricated on a dielectric guide(fig. 1.6(a)). This grating can facilitate both coupling and decoupling by providing an additional k-vector that equals the multiple grating vector $k_{\mathbf{GR}} = 2\pi/\Lambda$, where Λ is the grating period. If light with a wave-vector $k_L = 2\pi/\lambda_L$, where λ_L being the light wavelength in the adjacent medium, is incident on this grating at angle θ, then at a particular angle:

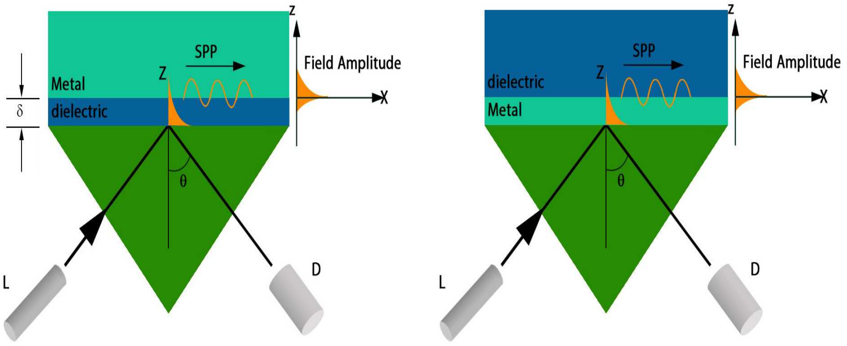

(a) **Otto** (b) **Kretschmann**

Figure 1.5: *Coupling light to plasmons using the prism phase matching techniques.*

$$\frac{2\pi}{\lambda_L}\sin\theta + n\frac{2\pi}{\Lambda} = k_{spp} \tag{1.32}$$

Where n is an integer. A similar relation also exists for the decoupling process. The equation however does not take into account realistic absorption and scattering associated with the finite size of grating profile.

Yet another common method of coupling surface plasmons is the End-fire coupling[25].

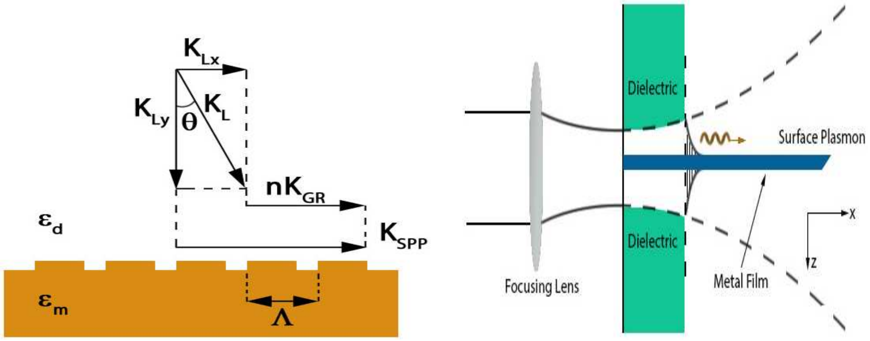

(a) (b)

Figure 1.6: *(a)Light coupling to an SPP wave using a grating to compensate the momentum mismatch. The SP wavevector equals the* x *component of the incident light vector* k_L *and* n *times* k_{GR}*, (b) End fire coupling.*

In this technique, a laser beam is focussed at the edge end of a thin metal film bounded on either sides by dielectrics. If the incident beam is p polarized, it would excite single or multiple plasmon modes at the metal-dielectric interface due to its large field overlap with these modes at the focal spot. This technique is quite useful when investigating proof of concept plasmonic devices. A schematic is shown in fig. 1.6(b).

Chapter 2

Numerical Techniques in Nanophotonics

This chapter deals with a detailed analysis of finite difference time domain and boundary element method numerical techniques that were extensively used in the thesis for modeling plasmonic structures.

One of the challenging tasks that remain to realize the goal of designing novel nanophotonic devices is to accurately model the electromagnetic response of nanostructures. The use of rigorous Maxwell's solvers in designing of rf and microwave antennas is already known for quite some time. In the optical regime however, in part due to the high contrasting dielectric properties of metals, the electromagnetic field may lead to excitation of strong localised surface plasmon resonances(LSPRs). At certain frequencies, these LSPRs exhibit very strong enhancement of the electromagnetic field, with a distribution that may present a fairly complex structure, thus demanding more accurate numerical modeling schemes.

The most conventional way till date to accurately model the optical behaviour of micro and nanostructures has been through the use of differential equation formulations like finite difference time domain(FDTD), finite element methods(FEM)[26–30] or finite integration techniques(FIT)[31, 32]. Other not so widely used techniques in plasmonics are the dyadic Green's tensor approach[33, 34] and the multiple multipole program(MMP)[35]. The FEM technique was developed initially for problems such as stress analysis, fluid flow and heat transfer. It gives approximate solutions of partial differential and integral equations. In this method, the simulation region is divided into a number of small units called elements, which are in turn connected to each other at specific points called nodes. Within the elements, the unknown field variables are expressed in terms of the approximate functions, mostly polynomials. In order to obtain an approximate solution for the whole system, the equations expressing the elements are first gathered. Then the system of equations is solved by employing the boundary conditions to obtain the unknown values at the nodes. The FDTD technique(which will be discussed in detail in the following section) is another widely used technique to solve electromagnetic problems. It uses the finite difference algorithm for solving the differential form of Maxwell's equations by discretizing them in both space and time. The FIT technique is considered as a general form of FDTD except that it is used to solve the integral form of Maxwell's equations.

The main advantage of field based techniques is that they can be easily implemented from Maxwells equations. The problem with these techniques however is that they are highly volumetric formulations strongly burdened with the discretization of the object and the surrounding space, and that they need to impose perfect matched layers(PML) like artificial boundary conditions. As a consequence, the precise analysis of extended three-dimensional (3D) plasmonic systems often exceeds current computational limits. Besides this, in some practical cases that involve sharp wedges or very small gaps, the rapid field variations due to the strong plasmon resonances are also cumbersome to determine for these field-based techniques. This can result in numerical dispersions, thereby affecting the accuracy of calculations.

Another useful method to compute the electromagnetic response of metals is to use the 2D boundary element method(BEM)[36]. This technique belongs to a class of method of moments(MoM) techniques. It is based on solving the Green's function surface integral equations. The basic idea behind BEM is that the final solution can be approximated to a partial differential equation(PDE) by extracting its solution on the boundary and then using this information to find the solution inside the domain. Although not yet widespread in optics, this approach brings important advantages in the case of homogeneous and piecewise homogeneous penetrable bodies, because these problems can be formulated in terms of surface integral equations (SIEs) defined over the material boundary surfaces and interfaces. This avoids the discretization of volumes and strongly reduces the required number of unknowns, which now scales linearly with the electrical size of the surfaces. Moreover unlike field based techniques where entire domain solution is calculated for a particular problem, BEM can be tailored for specific use as the solution on the boundary is calculated first followed by the solution in the domain, so the number of unknowns can be selected as per requirement.

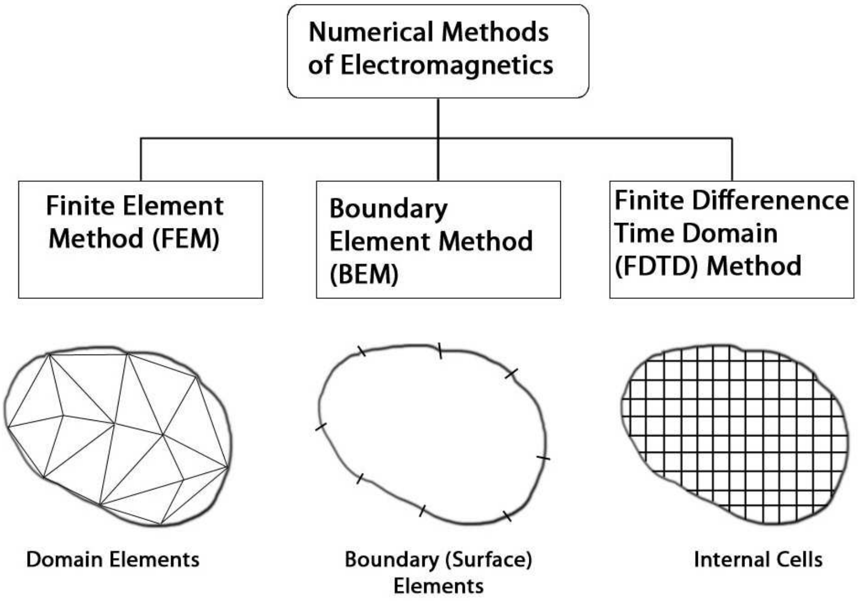

Figure 2.1: *Classification of different methods used for numerical analysis in electromagnetics*

2.1 FDTD

The FDTD technique has been established as a powerful numerical tool for modelling electromagnetic problems including those concerned with integrated optics devices. Its unique features include the ability to model light propagation, scattering reflection and polarization effects apart from incorporating material anisotropy and dispersion. The original FDTD algorithm was derived in 1966 by Yee[42]. Apart from nanophotonics, FDTD has since been used extensively in various domains such as in modelling microwave circuits, antennas. The FDTD uses centre-difference representations of the continuous partial differential equations to create iterative numerical models of wave propagation. The method involves the discretization of the field variables E, B, D, H in both space and time and converting the continuous space and time derivatives into finite differences in space and time. Spatial discretization occurs in the form of tiny discrete cubes. Each of these cubes will have six fields 3 each of electric and magnetic components. The field in each cube evolves in a way depending on the field history of the cube and its surrounding peers. Now in FDTD, a grid point in the solution region may be defined as[45]:

$$(i, j, k) = (i\Delta x, j\Delta y, k\Delta z) \tag{2.1}$$

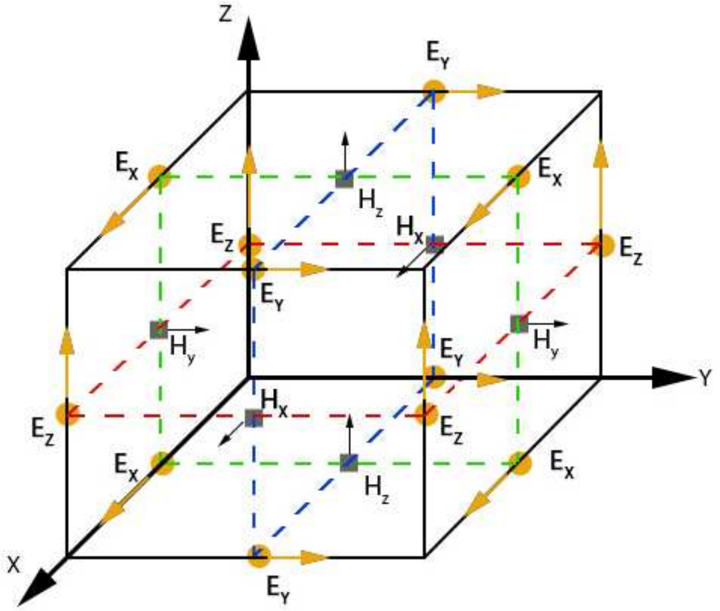

Figure 2.2: *Positions of field components in a Yees lattice depicting the FDTD grid*

And any function of space and time maybe given as:

$$F^n(i,j,k) = F(i\delta, j\delta, k\delta, n\Delta t) \tag{2.2}$$

Here $\delta = \Delta x = \Delta y = \Delta z$ is the space increment and t is the step wise time increment, also i, j, k and n are just integers. The space and time derivates are computed using the central finite difference approximation that is second order accurate:

$$\frac{\partial F^n(i,j,k)}{\partial x} = \frac{F^n(i+1/2,j,k) - F^n(i-1/2,j,k)}{\delta} + O(\delta^2) \tag{2.3}$$

$$\frac{\partial F^n(i,j,k)}{\partial x} = \frac{F^{n+1/2}(i,j,k) - F^{n-1/2}(i,j,k)}{\Delta t} + O(\Delta t^2) \tag{2.4}$$

Now again looking at the differential form of Maxwells equations:

$$\nabla \times H = J + \frac{\partial D}{\partial t} \tag{2.5a}$$

$$\nabla \times E = -\frac{\partial B}{\partial t} \tag{2.5b}$$

$$J = J_{source} + \sigma E \tag{2.5c}$$

$$M = M_{source} + \sigma * H \tag{2.5d}$$

Where σ is the electrical conductivity and J and M are the electrical and magnetic current densities. Suppose if we take the x component of the magnetic field from the above equation, we have:

$$\frac{\partial H_x}{\partial t} = \frac{1}{\mu}\left(\frac{\partial E_y}{\partial z} - \frac{\partial E_z}{\partial y} - M^x_{source} - \sigma^* H^x\right) \tag{2.6}$$

On applying the above equation of space derivatives to eq., we have the explicit finite difference approximation as:

$$\begin{aligned} H_x^{n+1/2}(i,j+1/2,k+1/2) \;&=\; H_x^{n-1/2}(i,j+1/2,k+1/2) + \frac{\Delta t}{\mu(i,j+1/2,k+1/2)\delta} \times \\ &\begin{cases} E_y^n(i,j+1/2,k+1) - E_y^n(i,j+1/2,k) \\ +E_z^n(i,j,k+1/2) - E_z^n(i,j+1,k+1/2) \end{cases} \end{aligned} \tag{2.7}$$

Similarly the other relations can also be derived.

2.1.1 PML

In FDTD, the size of the simulated area is limited by computational resources. It is required to have an artificial truncation condition at the boundary. If we suppose a wave generated from point source propagating in free space, as it propagates outward, it will eventually come to the edge of the simulating space, which is determined by the number of matrices fed in the program. If left like this, unpredictable reflections can be generated, that would go back inward. This way, we cannot determine the real wave from the unwanted reflections. One way to address this issue is by implementing a perfectly matched layer (PML) at the boundary of the simulation domain. This technique was initially developed by Berenger[43]. The fundamental idea of PML technique is to truncate one of the Maxwellian medium, by means of a non Maxwellian one, which is perfectly absorbing for all frequencies, polarizations and angles of incidence, and able to totally attenuate, from a practical point of view, the field propagated in its interior, after the propagation of just a few cells. In this technique, an artificial layer of absorbing material(either perfect electrically/magnetically conducting (PEC/PMC)) is placed around the outer boundary of the computational domain. The goal here is to make sure that a plane wave that is incident from FDTD free space to the PML region at an arbitrary angle is completely absorbed there without reflection. The basic idea is that, if a wave propagating in medium a impinges upon medium b, the amount of reflection is determined by the intrinsic impedances of the two media given by:

$$\Gamma = \frac{\eta_a - \eta_b}{\eta_a + \eta_b} \tag{2.8}$$

Which are in turn determined by the dielectric constants and the permeabilities of the two media:

$$\eta = \sqrt{\frac{\mu}{\epsilon}} \tag{2.9}$$

However, this still wouldnt solve the problem since the EM field would continue propagating in the new medium. What we need is a medium that is also lossy so that the field would die out before it hits the boundary. This can be accomplished by making both ϵ and μ complex by choosing appropriate values as the imaginary part would cause rapid decay causing truncation at the boundary.

2.1.2 Issue of Metals

Up until 1990s, it was not possible to model metals as the FDTD algorithm required the permitivity and conductivity to be frequency independent constants. Also the negative permittivity caused a positive feedback in the time iteration of the field components causing numerical instability. As metals form a critical component of any plasmon structure, it is important to include negative permittivity in any model. This problem was later solved by Lubber's *et al*[44] who assumed the metal simulated as a vacuum containing free electrons, i.e. the Drudes model by using the recursive convolution approach. The movement of electrons is thus factored into the discretization of Maxwells equations as an extra contribution of the electric field. Additionaly, Taflove[46] proposed the use of an auxillary differential equation in which the dielectric function is fitted with a function that obeys KramersKronig relations to be considered in the frequency domain so as to ensure causality of the FDTD simulation. In the Lumerical software, used in this work, it is possible to incorporate the model subject to the fitting condition of sampled data of the material dielectric constants.

2.1.3 Simulation Stability and Accuracy

The choice of cell size as well as time step is extremely important as enough no. of sampling points must be available in order to make adequate representation of the design components. As a thumb rule 20 mesh points per wavelength is suggested. To ensure the stability of the finite difference scheme, the time increment Δt must satisfy the following condition:

$$u_{max}\Delta t \leq \sqrt{\left(\frac{1}{\Delta x^2}+\frac{1}{\Delta y^2}+\frac{1}{\Delta z^2}\right)} \tag{2.10}$$

Here u_{max} denotes the maximum phase velocity of the model. It is to be however noted that in the case of metal structures it will be required to have an even finer mesh owing to a penetration depth small compared to the wavelength, thus leading to large discretization volumes along with very small grid spacings.

2.2 2D BEM

The fourth chapter of the thesis deals with an extensive study on the design and optimisation of optical absorption of an antenna assisted quantum dot photodetector by applying BEM formulation. The 2D code used in this study was developed by Salim Boutami of DOPT LETI, inorder to solve for the Maxwell's equation in the presence of arbitrarily shaped dielectric media having abrupt interfaces. In the perspective of plasmonics, BEM has been previously applied mostly to compute the scattering EM field off particles having spherical, cylindrical shaped geometries[37, 38]. Essentially this scattering problem is solved by computation of equivalent surface currents on the boundaries between different media in a unit sell.

For this particular study the 2D BEM method of calculation based on the Green's second integral theorem[38–40] was used. By choosing a 2D geometry, the formulation is further simplified since the 3D vectorial problem is reduced to a 2D scalar one. The physical system consists of n homogenious penetrable objects, each described by a frequency dependent dielectric function ϵ_j(j=1,2,...n). Ω_j is taken to be the surface profile of the jth scatterer. which is represented by the continious vector valued function $r_j \equiv (\xi, \eta)$ in the xz plane where $r = \sqrt{(\xi - x)^2 + (\eta - z)^2}$ being singular at the point $(\xi, \eta) \equiv \Omega$.

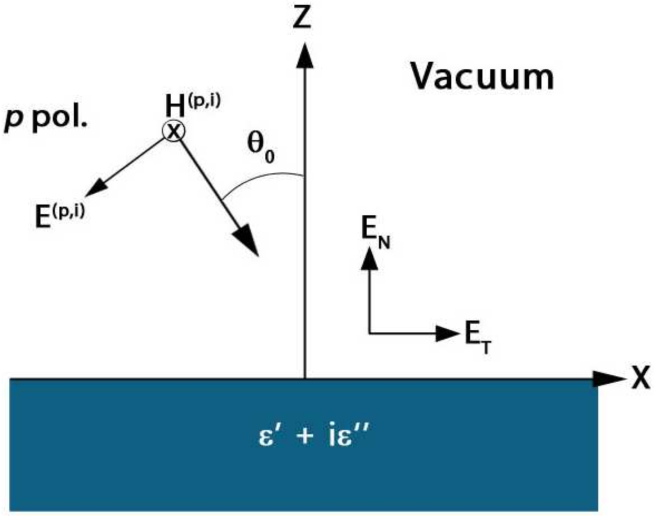

Figure 2.3: *The Co-ordinate system for BEM calculation*

A linearly polarised monochromatic EM field of frequency ω is chosen to be impinging on the system at an angle θ along the z-axis. For our case the angle θ is chosed to be zero implying normal incidence. Since the focus is on exciting plasmons(along the metal dielectric boundary), the incident field is chosen to be p polarised with the magnetic field perpendicular to the xz plane. This incident field in the case of normal incidence is given by:

$$H_y^{(p,inc)} = exp\left(-ik_0 z[1+w(x)]\right) exp\left(-\frac{x^2}{W^2}\right) \tag{2.11}$$

where w(x) signifies the beam waist. The integral equations for the magnetic field outside the scatterer are obtained from the Green's second integral theorem as:

$$\begin{aligned} H^{(inc)}(r) \quad &+ \quad \frac{1}{4\pi}\sum_j \int_{\Omega_j} \left\{ H^o\left[r_j(s)\right] \frac{\partial G^o\left[r, r_j(s)\right]}{\partial n_j} \right. \\ &- \quad \left. G^o\left[r, r_j(s)\right] \frac{\partial H^o(r_j)}{\partial n_j} \right\} ds \\ & \begin{cases} = H^o(r) & \text{for r outside scatterer} \\ = 0 & \text{for r inside scatterer} \end{cases} \end{aligned} \tag{2.12}$$

The corresponding equations for field inside the scatterer are:

$$-\frac{1}{4\pi}\sum_j \int_{\Omega_j} \left\{ H^i\left[r_j(s)\right] \frac{\partial G^i\left[r, r_j(s)\right]}{\partial n_j} - G^i\left[r, r_j(s)\right] \frac{\partial H^i(r_j)}{\partial n_j} \right\} ds$$

$$\begin{cases} = 0 & \text{for r outside scatterer} \\ = H^{(i)}(r) & \text{for r inside scatterer} \end{cases} \qquad (2.13)$$

Here the symbols H^{inc}, H^o, H^i represents incident field, scattered field outside media, and scattered field inside media respectively. The respective Green's functions $G^{(o,i)}(r, r')$ may be defined in terms of Hankel function of the first kind as:

$$G^{(o)} = i\pi H_0^1\left[\frac{\omega}{c}\sqrt{\epsilon^{(o)}}|r - r'|\right] \qquad (2.14)$$

$$G^{(i)} = i\pi H_0^1\left[\frac{\omega}{c}\sqrt{\epsilon^{(i)}}|r - r'|\right] \qquad (2.15)$$

For further simplicity, the source functions $\mathcal{H}_j(s)$ and $\mathcal{L}_j(s)$ are defined in terms of the parametric surface profile $r_j(s)$. As per the equation of continuity across the interface of the jth scatterer:

$$\mathcal{H}_j(s) = H^{(o)}(r)|_{r \to r_j^>(s)} = H^{(i)}(r)|_{r \to r_j^<(s)} \qquad (2.16)$$

$$\mathcal{L}_j(s) = \left[\frac{\partial H^{(o)}(r)}{\partial n_j}\right]_{r \to r_j^>(s)} = \frac{\epsilon^{(o)}}{\epsilon_j^i}\left[\frac{\partial H^{(i)}(r)}{\partial n_j}\right]_{r \to r_j^<(s)} \qquad (2.17)$$

The superscripts $<$ ($>$) signifying the limit of **r** taken from inside(outside) the scatterer. Now expanding the above equations 1.16 and 1.18 in terms of the source functions applying the continuity condition at the interfaces we obtain the following coupled integral equations:

$$\begin{aligned} H^{(i)}(r_l) \quad &+ \quad \frac{1}{4\pi}\sum_j \int_{\Omega_j} \mathcal{H}_j(s)\frac{\partial G^{(o)}\left[r_m r_j(s)\right]}{\partial n_j} \\ &- \quad G^{(o)}\left[r_m r_j(s)\right]\mathcal{L}_j(s)ds = \mathcal{H}_m(s) \end{aligned} \tag{2.18}$$

$$\begin{aligned} -\frac{1}{4\pi}\sum_j \int_{\Omega_j} \mathcal{H}_j(s)\frac{\partial G^{(i)}\left[r_m r_j(s)\right]}{\partial n_j}\frac{\epsilon_j^{(i)}}{\epsilon^{(o)}}G^{(i)}\left[r_m r_j(s)\right]\mathcal{L}_j(s)ds & \\ = \quad 0 & \\ m = 1, 2, ...n & \end{aligned} \tag{2.19}$$

The above integrals are converted into matrix form and evaluated using the Gaussian quadrature with a varying number of quadrature points. The source functions $\mathcal{H}_j(t)$ and $\mathcal{L}_j(t)$ are numerically evaluated from these matrix equations which can then further be used to find the near and far-field amplitudes.

Near field

The electric field is expressed in terms of the fourth Maxwell's equation as:

$$\nabla \times \mathbf{H} = -i\frac{\omega}{c}\epsilon\mathbf{E} \tag{2.20}$$

Once the source functions are determined, the corresponding E field for the x and z components may be obtained outside the scatterer using the above relation.

The surface electric field tangential($E_t^{(p,o)}$) and normal components($E_n^{(p,o)}$) is obtained from the source functions as:

$$E_t^{(p,o)}(\mathbf{r}_j(s)) = -\frac{ic}{\gamma\omega\epsilon^{(o)}}\mathcal{L}_j(s) \tag{2.21a}$$

$$E_n^{(p,o)}(\mathbf{r}_j(s)) = \frac{ic}{\gamma\omega\epsilon^{(o)}}\frac{d\mathcal{H}_j(s)}{ds} \tag{2.21b}$$

where $\gamma = \sqrt{(\xi')^2 + (\eta')^2}$.

The total power absorbed in any domain of interest is calculated from the total EM

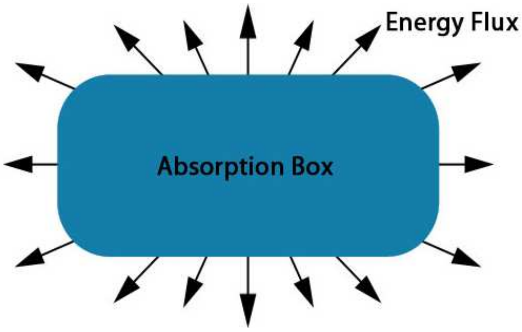

Figure 2.4: *Absorption in a particular domain calculated by extracting the outward Poynting vector*

flux across this region by real part of the time averaged Poynting vector:

$$\overrightarrow{\langle S \rangle} = \frac{1}{2} Re \left(E \times H^{*} \right) \tag{2.22}$$

2.3 FDTD vs BEM

Both techniques may provide for highly accurate solutions, and can be applied to arbitrarily complex geometries. Apart from this both methods provide an option for adaptive meshing.

Since FDTD calculates the field in the entire domain as part of the solution, it requires paramterization of the volume space. In BEM, only the surface is meshed so the computation time is correspondingly less. Moreover in BEM, the solution is first calculated at the boundaries, and then if required the domain fields are calculated seperately. On the bright side however, the computation time in FDTD scales linearly with the mesh($\sim N$) FDTD as compared to BEM($\sim N^2$).

FDTD requires artificial truncation at boundaries, and so unknown values may not be accurately calculated at boundaries. To avoid this, the truncation must be set at far away points to avoid numerical artifacts. One the other hand BEM doesn not require any truncation, it calculates exterior points same way as those within the boundary, so only the geometry of the boundaries need to be considered.

BEM has an issue that its solutions result in fully populated dense matrices. While FDTD solutions result in sparse matrices. This problem can be addressed by using techniques like the fast multipole method[48] which uses a multipole expansion of the Green's function.

Generally there is no problem while working with dispersive materials in BEM. In FDTD however, such materials should be approximated by suitable analytical expressions, which can cause significant problems in bradband calculations. The choice of using either FDTD or BEM methods depends mostly on the nature of problem. When dealing with integrated waveguides, field based techniques like FDTD, are arguably the best option since here the fields in the entire volume needs to be factored in while estimating the optical response of system. On the contrary, while working with problems like antenna design, BEM is the more favoured option, since here only the fields in a particular domain need to be considered.

Chapter 3

Numerical Investigation and Characterization of MOS Plasmonic Waveguides

3.1 Introduction

Plasmonic waveguides, given their sub-wavelength features may provide for an efficient means to channel optical energy in photonic interconnects. In the past, several waveguide geometries have been investigated which include planar (Dionne) as well as channel based structures. Out of these, the modal characteristics of plasmonic waveguides such as dielectric loaded SPP (DLSPP)guides[49–53], metal insulator metal (MIM)[55, 56], metal slot[57–61], metal insulator semiconductor metal(MISM)[62] ande even metal oxide semiconductor(MOS)[63] designs have been described in detail. Among the aforementioned plasmonic designs,the MOS plasmon waveguide is of particular interest as these structures could be easily fabricated using the mature Si based CMOS technology. Also, as compared to the gap waveguides, this design has relatively higher propagation lengths along with a reasonably good mode confinement. Moreover, the metals supporting plasmon modes can additionally serve as electrodes, making those MOS structures ideal candidates for transmitting electrical and optical signals in active devices. In this work we have numerically investigated a CMOS compatible MOS plasmon waveguide.

Coupling problem

In most of the previous works involving plasmonic waveguides the focus was mainly on studying their modal properties. One critical issue not fully addressed in these works has been that of coupling to the various modes of a MOS plasmonic waveguide. By and large, a plasmon waveguide is mostly characterised by its mode confinement and propagation length. In order to better understand the propagation characteristics of this structure, a detailed numerical analysis of both the modal as well transmission properties of plasmonic MOS structures of varied dimensions is required. The primary focus of this study is to investigate in detail this coupling mechanism when light is coupled to a MOS waveguide from an SOI photonic guide. The first part is dedicated to describing the waveguide geometry that includes sections of the SOI and MOS designs. The second part will describe in detail the modal and transmission analysis with fully vectorial FDTD simulations. The final part will include the experimental results as well as a discussion on the guiding mechanism of such waveguides as well as their potential applications in nanoscale optical communication systems.

3.2 Design Layout

A schematic of the device with cross sections of the SOI and MOS guides is shown in the figure. 3.1. The device consists of an SOI photonic guide resting on either sides of a MOS plasmonic guide. The input SOI photonic waveguide consists of a Si 220X500 nm cross section encapsulated by silicon nitride on all sides. The top part of this Si covered by 60 nm thick oxide followed by 100 nm of nitride. This entire stack is embedded in oxide layer. The plasmon waveguide consists of a 300 x 800 nm Cu metal deposited on a 3nm thick nitride barrier [24] to block any diffusion. The nitride layer rests on a 10 nm SiO2 followed by the Si layer. We will denote the width of the plasmon guide by the width w_{si} of the silicon guide. We denote the different material indexes as $N_{Si} = 3.46$ for silicon $N_{SiO2} = 1.44$ for oxide $N_{SiN} = 2$ for nitride, and $N_{Cu} = 0.2 + 11i$ for copper. As Si absorption is negligible in the C band, the SPP mode propagation loss is primarily determined by the choice of metal. A salient feature in this device is the incorporation of a low loss Cu[83] for deposition and a thin nitride barrier[84] to prevent Cu diffusion in Si. Although silver has a lower propagation loss at the C band, it is also a known contaminant in the CMOS process.

3.3 Simulations

The simulations were performed FDTD package from Lumerical Inc. At first a comprehensive mode analysis was performed using the built in mode solver for both SOI and MOS waveguides. When speaking of the case of finite guides, in reality there are no pure transverse modes, only hybrid modes exist. So a TE mode will always have

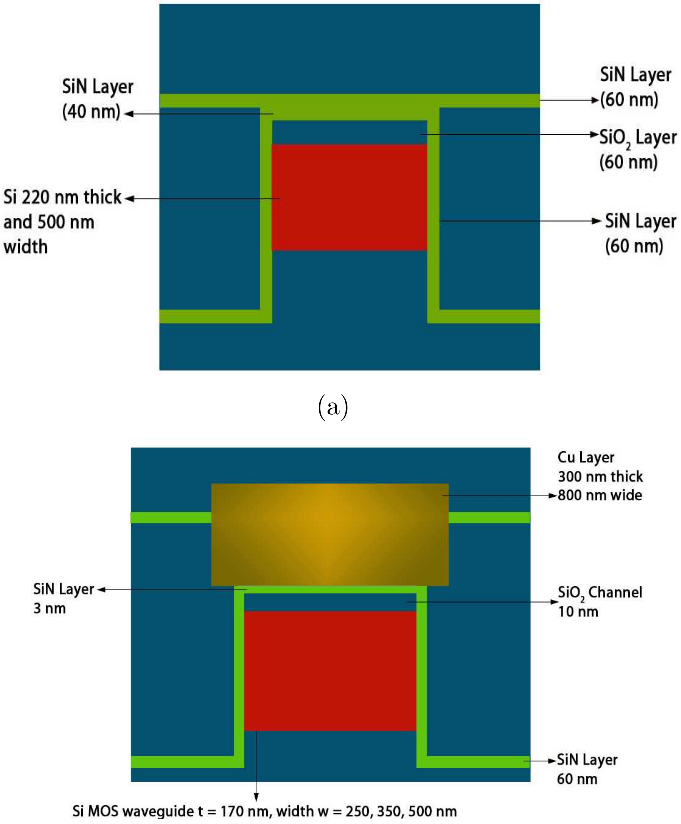

(a)

(b)

Figure 3.1: *(a) cross section of the SOI waveguide and (b) cross section of the MOS waveguide.*

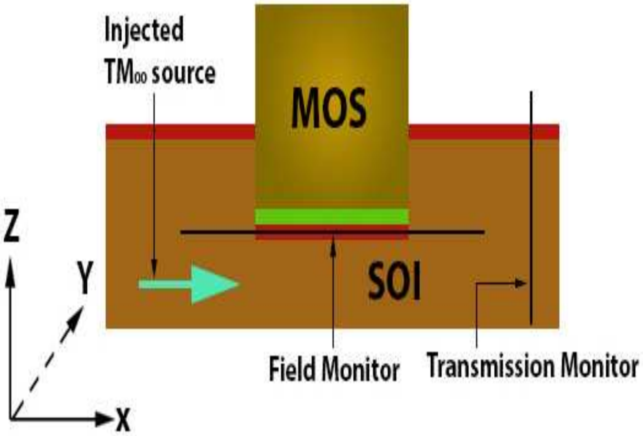

Figure 3.2: *Schematic of the device used in FDTD simulation consisting of the MOS structure in between two SOI guides. Field monitors are placed in the oxide layer and output interfaces.*

some component of TM and the converse is also true. The SOI guide was found to have two fundamental modes. A predominantly TM_{00} mode at 1.92 and a TE_{00} mode at 2.52. Since only the TM mode will couple to plasmons, we choose this to be the excitation mode in our transmission analysis. The meshing chosen for the plasmon guide was adaptive, ie. 1 nm in regions close to the metal interface and is global in the bulk regions. The MOS waveguide was found to have several modes including a fundamental SPP mode. Some of these are guided modes and others have a leaky profile.

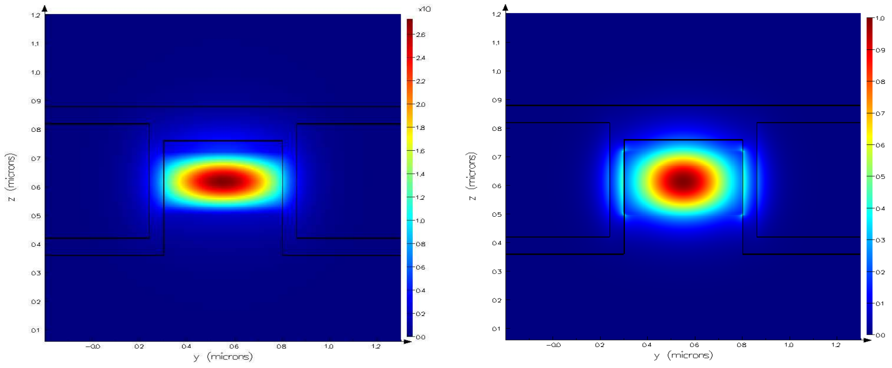

(a) *SOI TM mode* (b) *SOI TE mode*

Figure 3.3: *(a) Magnetic field intensity of fundamental TM mode of SOI guide(*$N_{eff} = 1.9$*) and (b) E field intensity profile of fundamental TE mode(*$N_{eff} = 2.52$*) in linear scales.*

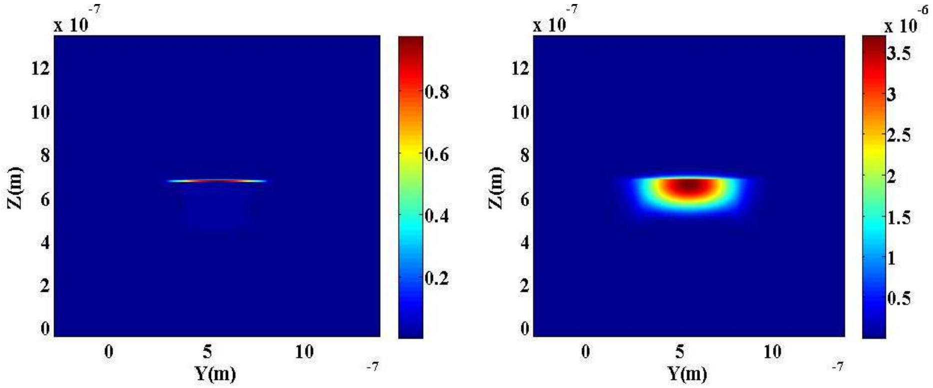

(a) *E field* (b) *H field*

Figure 3.4: *The fundamental SPP mode(*$N_{eff} = 2.49 + 0.0056i$*) for MOS guide of* w_{Si} *=500 nm and thickness 170nm. (a) The electric field and (b) magnetic field intensity profiles(right). The fundamental mode always exists for any waveguide dimension.*

3.3.1 Transmission analysis

A fully vectorial simulation is now performed to gauge the coupling between the SOI and MOS guides. The input mode launched in the SOI waveguide(fig. 3.2) is a TM_{00} polarized in the y direction at 1.55 μm with a predominant transverse magnetic field profile so as to be able to couple to the fundamental SPP mode of the MOS waveguide. The injected mode source is placed about 2.6 μm from the MOS/SOI interface. The simulation volume was chosen to be big enough to avoid any boundary artifacts. First of all a convergence test was performed with the output power monitors to see if there is any transmission variation as a function of monitor position in the output SOI guide. This is necessary to eliminate any unavoidable contributions from scattered fields close to the MOS/SOI interface. These results are shown in fig. 3.5. The total transmitted power seems to saturate after a distance of 2 μm. For further analysis, the distance between the output interface and the position of the monitors in the SOI guide will be fixed at 2.6 μm. Usually while simulating a device of several microns, which also includes fine meshing, the computation time is large. One way to reduce this time is to select symmetric boundary conditions(BC). Since our device is symmetric about the y-axis and the input TM mode is also launched at the equilibrium position of this axis, selecting a boundary condition with y-symmetry would halve the region of computation. From table 3.1, it is clear that choosing a symmetric boundary does not

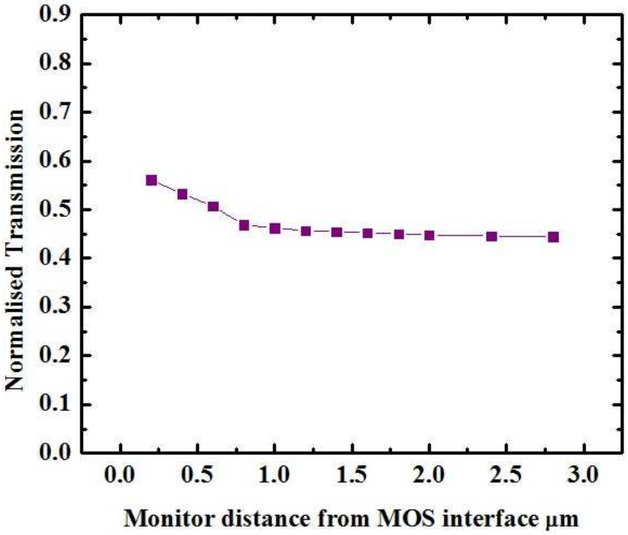

Figure 3.5: *Convergence study of transmission for field monitors as a function of distance from output interface.*

BC Symmetricity(of y)	N_{eff} SOI	N_{eff}(Spp)	Im(Spp)	Power(2μm)	Power(3μm)
Symmetric BC	1.9	2.49	0.0057	0.3219	0.3094
No Symmetric BC	1.9	2.49	0.0056	0.324	0.3084

Table 3.1: Comparison of device transmission and mode properties for symmetric and no symmetric boundary conditions

alter the transmission and modal properties of the device. While no change is observed in the mode values of either the photonic or fundamental plasmon mode, only a slight variation of less than 1% is observed in transmission. Therefore for the remaining analysis, the option of symmetricity will be utilized. The average time required for a single simulation was observed to be around 7-8 hrs. The power transmission was plotted as a function of the MOS device length. A 50 nm device sampling was chosen. These results are summarized in the following figures 3.6

All plots depict two distinct oscillations. The small period oscillations in each case is roughly 330 nm which indicates that it is the cause of Fabry-Perot effect of the fundamental SPP mode at the two interfaces. The origin of the big period oscillations at this point is not clear. A simple linear fit of the transmission plot pegs the losses at 0.22 dB/μm which is close to the 0.2 dB loss of the fundamental plasmon mode. Moreover a slight improvement in transmission is observed when moving from 250 to 500 nm width MOS guides. To further analyse the big period oscillations, the electric field is extracted from the monitor placed in the oxide layer. This profile is shown in the fig. 3.7. It is seen that even in this case, a two mode behaviour is observed with the same periodicity of oscillations as seen in the transmission plots. It might now be interesting to study the power coupling to various modes of the MOS waveguide which is described in detail in the next section.

3.3.2 Power coupling analysis

Fundamental SPP mode

While for a single isolated waveguide, the electromagnetic fields may be accurately described as a superposition of the orthogonal modes, the modes of the two constituent waveguides in a coupler configuration do not comprise an orthonormal basis set. Therefore, the input field profile ψ_{inp} of the incoming guide can be expanded into a basis of eigenmode solutions of the output guide.

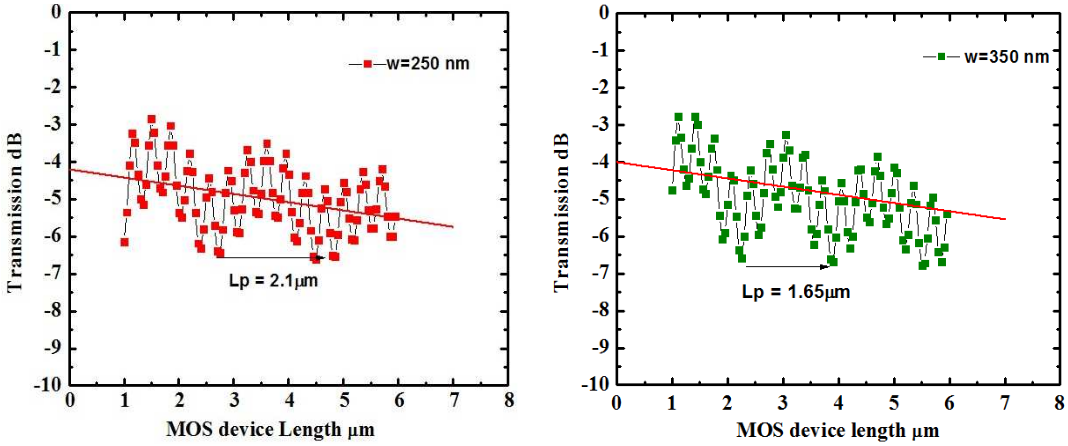

(a) *MOS width 250 nm* (b) *MOS width 350 nm*

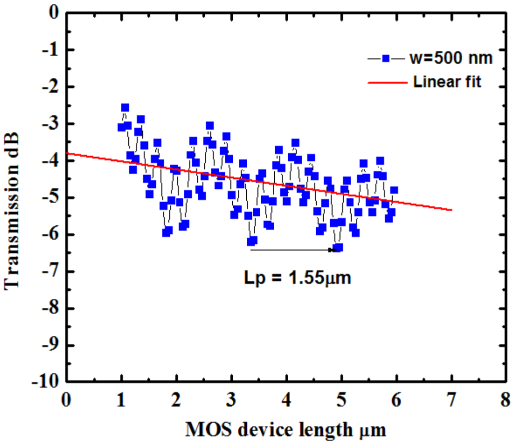

(c) *MOS width 500 nm*

Figure 3.6: *Device transmission in dB as a function of MOS device length. The small oscillation corresponds to the Fabry Perot oscillation of the fundamental SPP.*

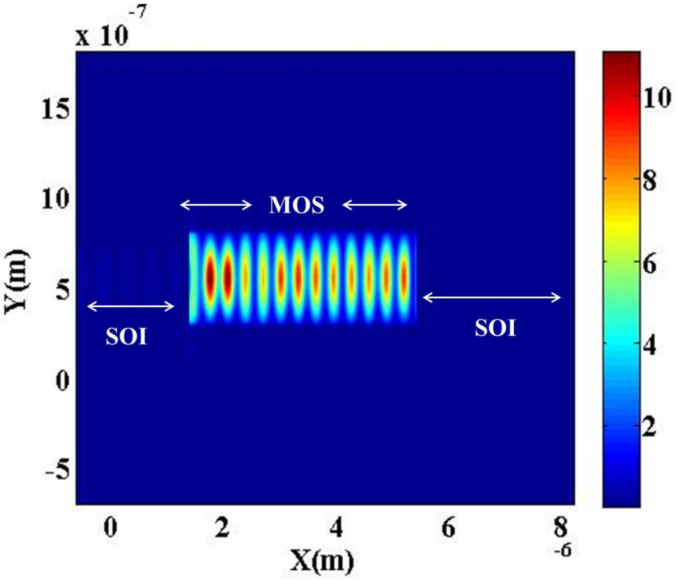

Figure 3.7: *E field intensity (linear) in the oxide layer of a MOS guide 500 nm wide. The field profile shows a dual contribution which on the onset looks similar to the transmission plot.*

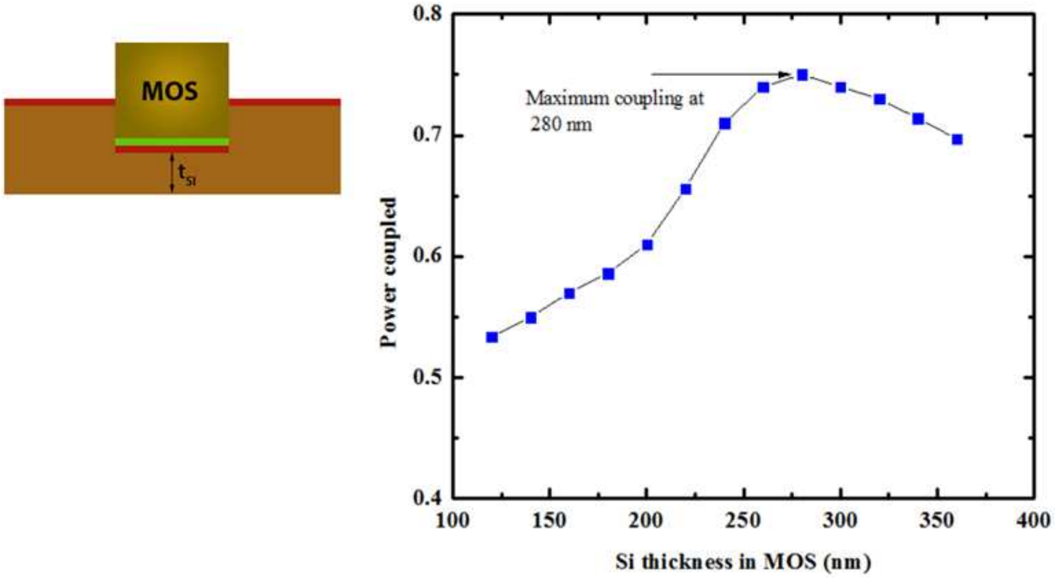

Figure 3.8: *Power coupled between fundamental Spp mode with photonic mode of SOI guide as a function of* t_{Si}.

$$\psi_{inp} = \sum_i c_i \psi_i \tag{3.1}$$

Where C_i is the correlation coefficient that defines the overlap integral between the input field and the corresponding eigenmodes.

$$C_i^2 = \frac{|\int\int \psi_{inp}\psi^{\star}_{plas} dS|^2}{\int\int \psi_{inp}\psi^{\star}_{inp} dS \int\int \psi_{plas}\psi^{\star}_{plas} dS} \tag{3.2}$$

The overlap integral expression has been evaluated in detail in Appendix A. A deeper analysis of this expression can also be found in [68]. The total power coupled is the product of the overlap integral with the Fresnles's transmission coefficient.

$$P_{coupl} = C_i^2 \frac{4n_{phot}n_{plas}}{(n_{phot} + n_{plas})^2} \tag{3.3}$$

where n_{phot} and n_{plas} are the effective indexes of the incoming mode and the output eigenmode respectively. Consequently a study was conducted to calculate the power coupled from the SOI photonic mode to the fundamental TM_{00} SPP mode as a function of the MOS Si thickness from the etch. A simulation was first performed by choosing a particular eigenmode and then extracting its corresponding fields. These results are plotted in fig. 3.8. The coupled power depends the overlap integral which is a function of the field displacement between the input and output guides. At lower MOS thickness, the SPP mode is not only more deconfined due to a lower Si layer thickness, but also has a less overlap with the input photonic mode. As the Si layer is increased, the SPP mode becomes more confined and its overlap also increases with the photonic mode. There is an observed increment of the coupled power to the fundamental mode which peaks at 75 % at 280 nm and then starts to decrease. The subsequent decrease can be explained due to the field overlap mismatch between the input and output guides. Interestingly, no significant dependence of the coupled power to the TM_{00} mode is observed as a function of MOS Si width.

Edge modes

Apart from the fundamental SPP mode, the MOS guides also support some edge modes and leaky modes. Since in our MOS design these edge modes are close to the cladding index, they may be classified as having quasi-leaky behavior. The MOS waveguide supports two such modes that we choose to designate as N_{e1} (N_{eff}=1.42+4.5e-4i) and N_{e2} (N_{eff}=1.55+1.44e-3i) both depicted in fig. 3.9. The power coupled these modes as calculated from the above relations is shown in table 3.2. There appears to be some coupling to mode N_{e1} at about 5% which does not significantly change with MOS width. It may be pointed out that the study of leaky modes that exist well below the oxide cladding index has been excluded as given the divergent nature of such modes, they are not easily derived using the built in mode solver. A further issue is that, the overlap integral formulation would not be a valid approximation in this region and so power coupling to these modes would be difficult to ascertain. One way to check if the above observed edge modes are responsible for the big period oscillations is to carry out a simulation where the metal has been pushed into the PML boundary laterally (as shown in fig. 3.10(a) as well as in the direction of propagation. In doing so the edge modes will no longer be supported by the MOS guide. The result of this simulation is shown in fig. 3.10(b). As expected the Fabry-Perot oscillations are no longer observed. However the other oscillatory effect still persists albeit with the same periodicity as observed in the transmission analysis despite the fact that the MOS guide in this case supports only a single mode. It would be interesting to compare this effect with that observed in the case of higher order TM modes as shown in the next section.

Si width in MOS (nm)	Power coupling	
	N_{e1}=1.42	N_{e2}=1.55
250	0.0425	0.0019
350	0.0534	0.00124
500	0.0594	0.0009

Table 3.2: Power coupling to edge modes as a function of MOS width.

3.3.3 MMI effect in MOS

The multimode interference (MMI) phenomenon has already been known to occur in both in the case of photonic[64–67] as well as recently in plasmonic waveguides[69–74].

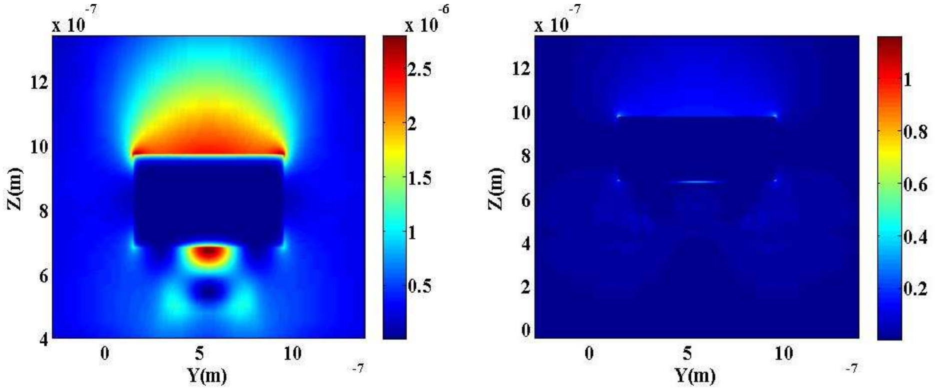

(a) **H field** (b) **E field**

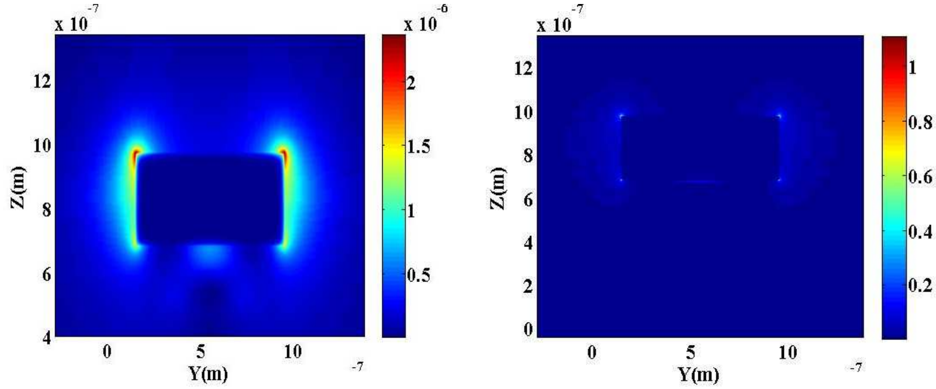

(c) **H field** (d) **E field**

Figure 3.9: *Field profiles of the quasi leaky edge modes,(a)-(b) for* N_{e1} *and (c)-(d) for* N_{e2}.

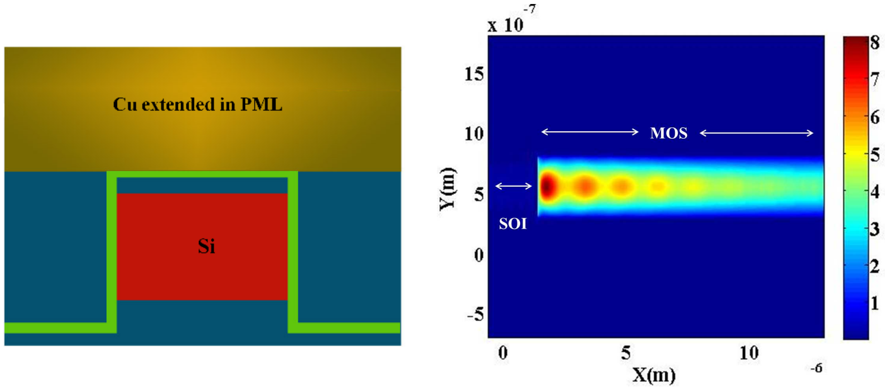

(a) *MOS layout* (b) *Extracted field*

Figure 3.10: *(a) Cross sectional view of the MOS guide with metal extended into PML. (b) E intensity profile in the oxide layer of the MOS guide. The big period oscillations are still observed.*

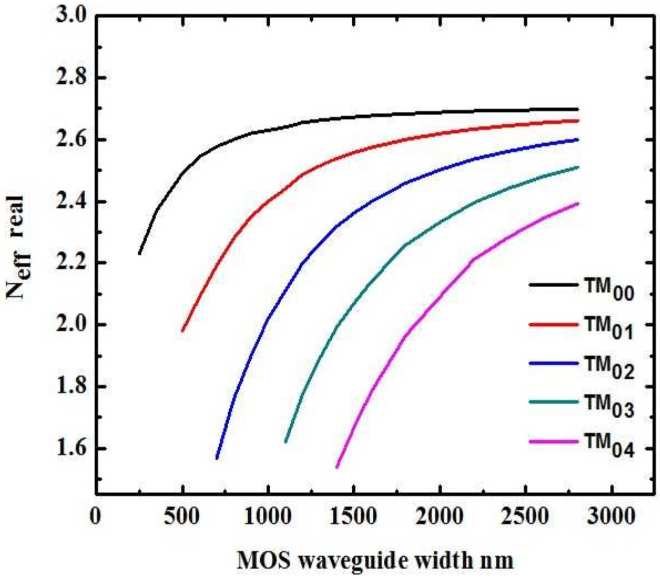

Figure 3.11: *Variation of effective index of higher order modes with MOS width.*

In these studies a multimode interference is observed due to beating between two lowest order modes supported by the plasmon guide. In our case however, the limited width of plasmon guide do not permit the occurrence of any higher order modes. Fig. 3.11 clearly shows that the first of the higher order modes(TM_{01}), starts to appear only beginning at a waveguide width of 500 nm. The extracted field patterns as shown in figures 3.12 with different MOS widths, seem to indicate a complicated oscillatory feature between 600-1000 nm. This is also the region where higher order modes start to appear in the MOS guide. At higher MOS widths, MMI effect due to *self imaging* begins to take precedence and dominates the transmission. This dual behavior of the MOS guide at different regions would point out to the contribution of leaky modes with a lower than cladding effective index at lower widths. Interference between guided and leaky modes is not uncommon and has been reported before[75–77].

Self Imaging

Self imaging occurs when an input field is reproduced in single or multiple images at periodic intervals along the direction of propagation. Self imaging is akin to a similar general phenomenon known to exist in near field optics called the *Talbot effect* [78,79], whereby due to a superposition of modes, the field repeats itself after a distance called the Talbot length. This effect can exist in both free space as well as waveguides. In

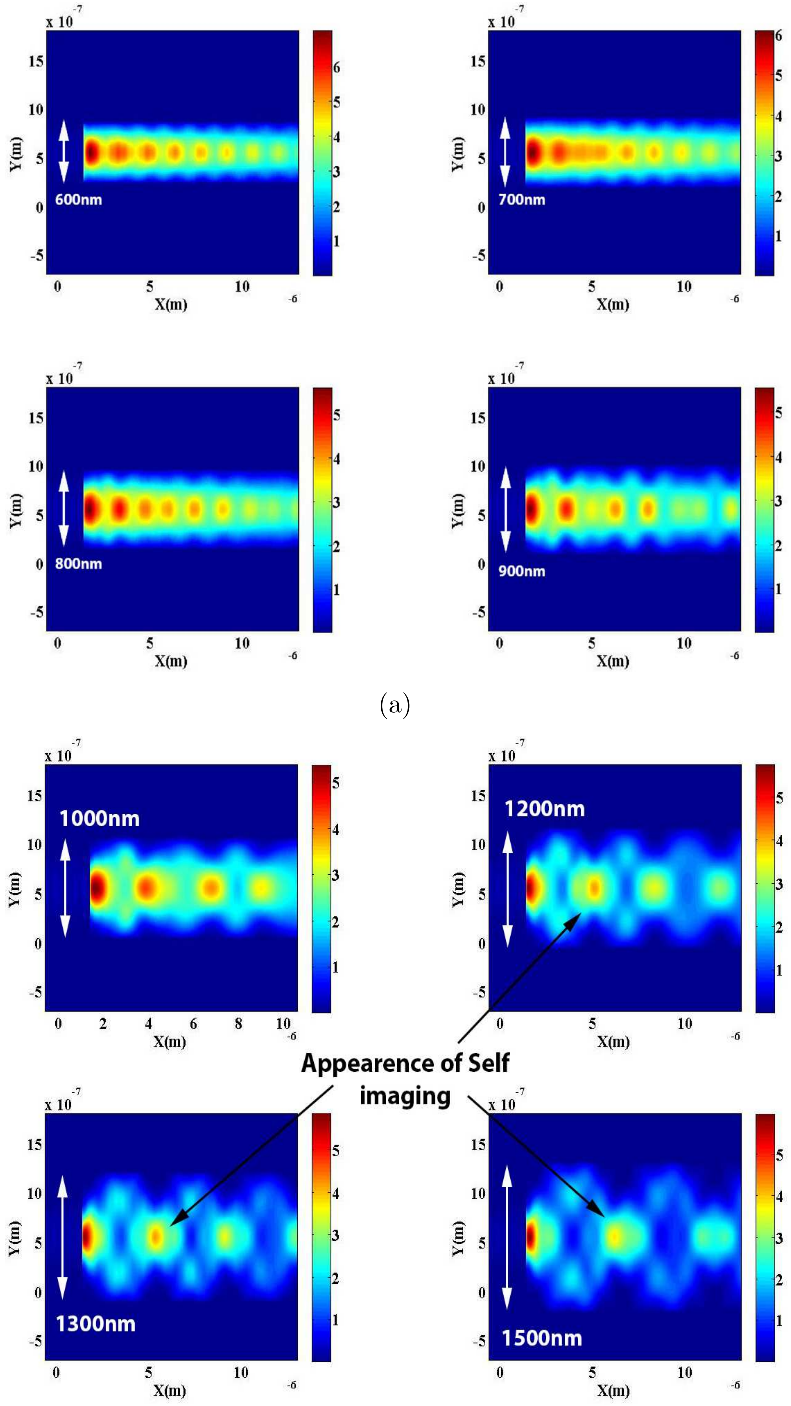

(b)

Figure 3.12: *Extracted E intensities at different MOS widths at thickness 170 nm for (a) 0.6-0.9μm and (b) 1-1.5μm. MMI effect starts to become more prominent at widths greater than 1 μm.*

the case of free space, Talbot distance z occurs in multiples of $2\frac{g^2}{\lambda}$ where g is the grating period. Many applications have been suggested using this effect, such as in interfereometry[80,81] and temporal filtering[82]. Essentially the field profile of an input wave travelling in a guide at a certain distance L can be written as a superposition of all guided fields:

$$\Psi(L) = \sum_{i=0}^{m-1} c_i \psi_i exp\left(j\frac{i(i+2)}{3L_\pi}L\right) \tag{3.4}$$

Where L_π is the beating length between the two lowest order modes $L_\pi = \frac{1}{n_0 - n_1}$. The condition for self imaging exists when the exponential term is either 1 or (-1^i). The first condition means that a single image is in 2π phase with its input field while the seond condition means that π phase mirrored image is formed. Some of the higher order TM

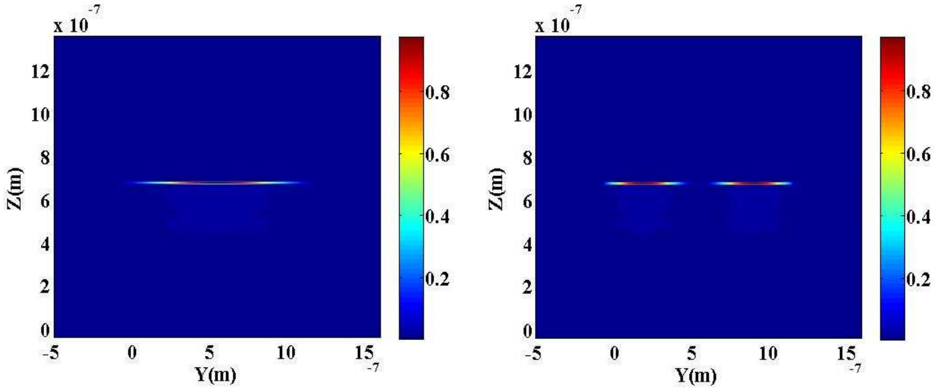

(a) TM_{00} (b) TM_{01}

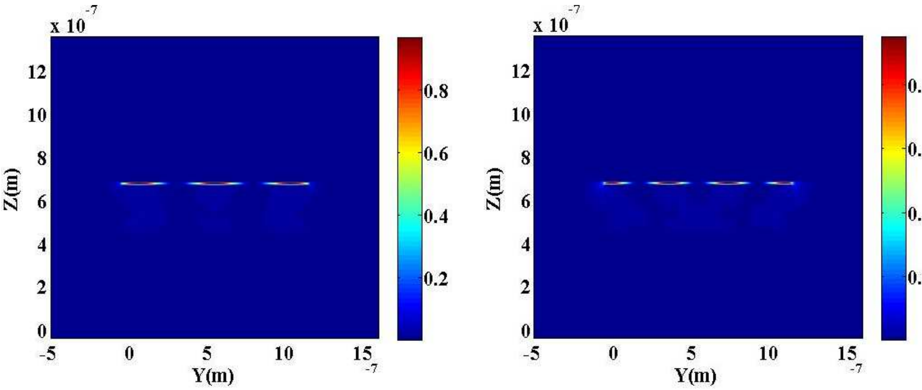

(c) TM_{02} (d) TM_{03}

Figure 3.13: *The E field intensity profiles of different higher order modes supported by a MOS of 1200 nm width.*

Width (MOS)	N_0 (TM_{00})	N_1 (TM_{01})	L_{self} $= \frac{3}{8}\frac{\lambda}{N_0-N_1}$	L_{self} simulation
1200	2.65	2.48	3.42	3.6
1300	2.66	2.515	4	4
1500	2.67	2.55	4.84	4.8

Table 3.3: The position of first self imaging length from expression and simulations for the case of restricted MMI effect. At higher widths, there is a convergence between the analytical and simulated values.

mode profile supported by a 1200 nm width MOS guide are depicted in fig. 3.13. All of the modes show a similar field distribution with most of the electromagnetic energy being confined in the oxide layer. The self imaging distance for an N fold image is generally given by the relation :

$$L_{self} = \frac{p}{N} 3L_\pi \tag{3.5}$$

Where p denotes the periodicity of imaging. Accordingly a single image of the input field is formed at a distance L_{self}=p($3L_\pi$). Since in this case the launch of the input field is symmetric, only even order modes are launched along the waveguide. This corresponds to the restricted multimode interference. The self imaging distance is much shorter: An N fold image for this condition occurs at:

$$L_{self} = \frac{p}{N}\frac{3L_\pi}{4} \quad p = \mathit{0}, \mathit{1}, \mathit{2}... \tag{3.6}$$

Which means the first single image will occur at $3L_\pi/4$. Table 3.3 gives a comparison between the calculated analytical and simulation values of the self imaging distance of the MOS device. It is observed that as the MOS width increases, there is a convergence between the two values. Multimode interference based passive components like beam splitters, routers of photonic structures are are routinely made use of in integrated device applications. The self imaging nature of MOS plasmonic guides can be exploited to develop passive elements like compact 3 dB couplers, routers. Typical photonic elements of such components are several tens of microns wide and hundreds of microns long. With plasmon based components, these features can be brought down to only a few microns size.

SOI wafer consisting of 220 nm Si on 120 nm Burried oxide

Channel Si etched down to substrate by photolithography

Planar encapsulation by 60 nm thick conformal Si_3N_4 layer

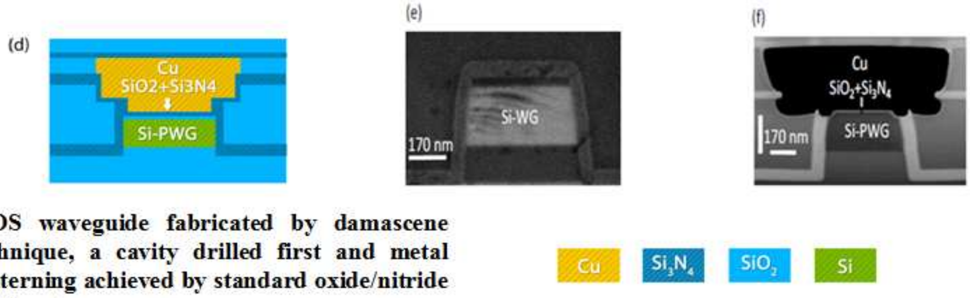

MOS waveguide fabricated by damascene technique, a cavity drilled first and metal patterning achieved by standard oxide/nitride etching steps

Figure 3.14: *Schematic showing different steps involved in device fabrication for SOI(top) and MOS(bottom).*

3.4 Experimental Characterization

3.4.1 Device Fabrication

The MOS plasmonic waveguide fabrication was done on a 8 inches silicon-on-insulator (SOI) platform. The seed wafer consisted of a 220 nm layer of Si on a 120 nm buried oxide (BOX). Firstly, in order to couple to the fundamental TM mode of the Si photonic waveguide, the coupler gratings of of 950 nm period, 70 nm depth and 50 duty cycle were dry etched into the top silicon layer. The channel silicon waveguides were fabricated by photolithography and etching down to the silicon substrate. Planar encapsulation of this layer was performed with a conformal 60 nm thick Si_3N_4 layer and TEOS(tetraethyl orthosilicate) oxide followed by chemical mechanical planarization step.

Fabrication of the MOS plasmonic waveguide is done by the damascene technique. Initially the silicon wafer was deposited with a 800 nm thermal oxide layer. A cavity was then drilled into this oxide layer followed by dry and wet etching steps. After etching down to a 10 nm thick oxide layer, a thin stoichiometric Si_3N_4 layer was deposited atop thix oxide. Subsequently the Cu layer was then deposited atop this nitride layer

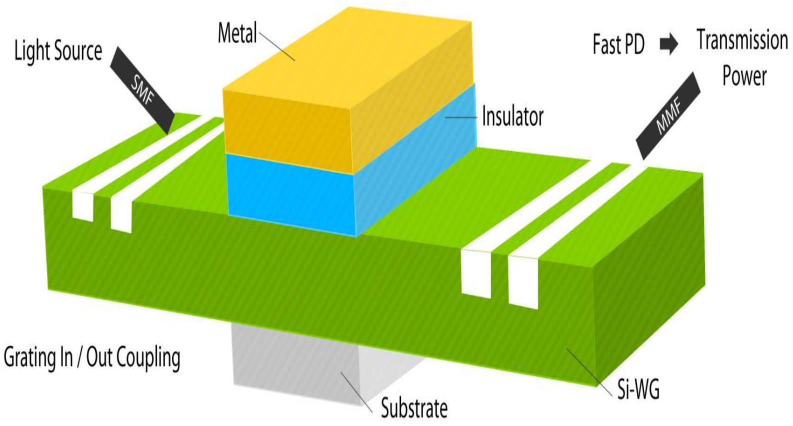

Figure 3.15: *The experimental setup used for optical characterization. SMF and MMF are single and multimode fibers respectively.*

by plasma vapour deposition and electrochemical deposition before being polished by chemical mechanical polishing. This step is then followed by encapsulating the MOS region into nitride and oxide deposition. The wafer was then directly bonded to a 2 μm carrier wafer and the Si substrate of the initial wafer was removed by mechanical grinding and chemical etching. Further details on the device fabrication procedure are available in [84].

3.4.2 Transmission Measurements

Optical characterization to gauge the transmission through a MOS coupled SOI waveguide was performed using a fiber laser source of 1.55 μm. The output of this laser source fed to a monomode fiber was coupled to the TM photonic mode of the SOI guide through grating couplers. The monomode fiber was fixed with an optical axis of 10 deg with respect to that of wafer. The output transmission was retrieved by a multimode fiber which was positioned at the output grating using a ANDO AQ2140 optical multimeter. The device measurements were carried out automatically using a KARL SUSS automatic wafer probe station. The output data was normalised to the reference data of a wholly SOI guide that was placed at the beginning of each cluster of 34 MOS waveguides. The MOS guide length is varied between 1 and 7 μm with step sizes of 150 nm. The advantage of having a wafer scale testing with a large number of devices is that the measurements can be done with a huge sampling which is useful for a statistical analysis of the fabricated device parameters. In this case, for each device

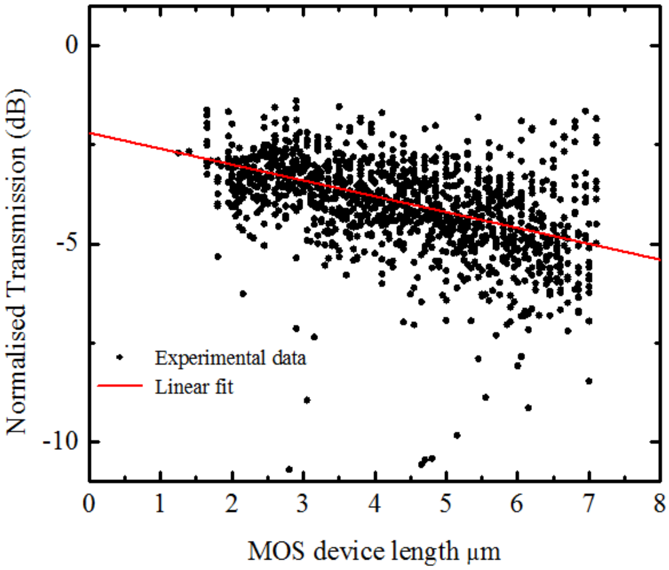

Figure 3.16: *The transmission results of similar devices of varied lengths fitted exponentially[84].*

that was tested, there were 18 identical devices of similar dimensions spread among several dyes.

3.4.3 Results and discussion

The results of transmission are plotted in fig. 3.16. An experimental fit gives, plasmon propagation loss of around 0.4 db/μm, which is considerably higher than those observed in simulations. One cause of this is that the ellipsometric values of the Cu index used in the device were later confirmed to be 0.3+11i. Another cause of the higher propagation losses may be attributed to device fabrication imperfections. Given the higher losses, and the considerable spread of transmission data, it is difficult to ascertain if there is an associated oscillatory feature like the one observed in simulations. In another work however, we have experimentally[85] shown that at certain optimized lengths of MOS waveguides, the coupling between an SOI guide and a MISM waveguide can be considerably improved. The experimental evidence from this work does show traces of complex oscillatory features like the one observed in simulations Further experimental investigation would however be required to shed more light on the impact of leaky modes in plasmonic guides.

3.5 Conclusion

The chapter has largely focused on a numerical analysis of the transmission and modal characteristics of a MOS plasmonic waveguide. Although mode overlap studies points to coupling predominantly to the fundamental plasmon mode, transmission results as well as field profiles from simulations show an oscillatory behavior. These oscillations seem to be possibly be the cause of some non-negligible coupling to leaky modes. It must be pointed out however that due to the large computation time required, multiple wavelength dispersion analysis could not be carried out which would have given some useful insights into the transmission results.

Some experimental characterization of MOS plasmon guides fabricated on a wafer was also performed, At the outset, given the low sampling of the device length, the high spread of transmission data among devices of different dyes, and the higher propagation losses it seems difficult to separate any oscillatory features from the output.

Numerical studies show that MOS propagation at higher widths is characterized by the multimode interference due to self imaging effect of higher order plasmon modes. The self imaging feature of MOS waveguides can be used to design passive plasmonic elements like WDM, routers, splitters, beam combiners of much smaller footprints than photonic devices.

Chapter 4

Modeling of Plasmon assisted Ge EA Modulators

In this chapter, we theoretically analyse the possibility of developing a plasmon assisted high speed Ge on Si electroabsorption(EA) modulator based on the Franz Keldysh effect. Numerical results encompassing the device design for both optical and electrical operation are presented to assess the critical parameters for device performance.

4.1 Introduction

The integration of optoelectronic circuits via Si based CMOS technology has been the central focus of both industry and academia for quite some time. Given the vast scale of infrastructure that already exists in the fabrication of integrated electronic circuitry on CMOS platforms, it has become necessary to design active photonic devices like sources, modulators and photodetectors that can exploit these facilities. Unfortunately however, most of the best performing photonic materials for these devices are almost exclusively III-V based compounds[86–91]. Inspite of this, III Vs have yet not emerged as the preferred choice for large scale integration of nanophotonic circuits due to the inherent complexities of integrating them into existing platforms of microelectronics. The fundamental challenge thus lies in finding materials that are compatible with the CMOS environment as well as developing devices that fulfill the stringent requirements of low footprint and high speed data transfer. A brief overview of free carrier induced index change and FK based EA effect in Ge are discussed below.

4.2 Modulation mechanisms in semiconductors

4.2.1 Free carrier index change

In a semiconductor, the two main potential sources of absorption are the interband absorption and the free carrier plasma dispersion(FCPD). The former occurs when photons with an energy greater than the band gap are absorbed, which then excite the electrons in valence band into the conduction band. Since band gap of Si lies at 1.12 eV corresponding to a wavelength of 1.1 μm, this effect would not be present for wavelengths near the C band.
The other primary source of light absorption in semiconductors might be through free carrier absorption. This type of absorption occurs mainly for frequencies below the interband absorption edge. The change in the free carrier density of Si will affect both the real and imaginary part of the refractive indices. These free carriers may be generated either by optical or electrical switching. The absorption change in Si may be described by the well-known Drude-Lorentz equation [92]

$$\Delta\alpha = \frac{e^3\lambda_0^2}{4\pi^2 c^3 \epsilon_0 n}\left(\frac{N_e}{\mu_e\left(m_{ce}^\star\right)^2} + \frac{N_h}{\mu_h\left(m_{ch}^\star\right)^2}\right) \tag{4.1}$$

where e denotes the electronic charge. μ_e and μ_h are the electron and hole electron mobilities. $m_{ce}^\star$ and $m_{ch}^\star$ are the effective masses for electrons and holes. N_e and N_h are the free electron and hole concentrations respectively. The carrier concentration also affects the change in refractive index Δn given by:

$$\Delta n = \frac{e^2\lambda_0^2}{8\pi^2 c^3 \epsilon_0 n}\left(\frac{N_e}{m_{ce}} + \frac{N_h}{m_{ch}}\right) \tag{4.2}$$

Soref and Lorenzo[93, 94] had evaluated the data for values of N in the range of 10^8 to $10^{20} cm^{-3}$ for both change in absorption $\Delta\alpha$ and refractive index Δn using the Lorentz relation, particularly for the communication wavelengths 1.3 μm and 1.55 μm. However their results were found to be in good agreement only for electrons. For holes a $(N)^{0.8}$ dependence was observed. They derived the following expressions which is now most widely used for estimating index change due to free carrier absorption in Si:

At $\lambda_0 = 1.55\mu$m

$$\Delta n = \Delta n_e + \Delta n_h = -\left[8.8 \times 10^{-22} \Delta N_e + 8.5 \times 10^{-18} \left(\Delta N_h\right)^{0.8}\right]$$
$$\Delta \alpha = \Delta n_e + \Delta n_h = 8.5 \times 10^{-22} \Delta N_e + 6 \times 10^{-18} \left(\Delta N_h\right)^{0.8} \tag{4.3}$$

And at $\lambda_0 = 1.3\mu$m

$$\Delta n = \Delta n_e + \Delta n_h = -\left[6.2 \times 10^{-22} \Delta N_e + 6 \times 10^{-18} \left(\Delta N_h\right)^{0.8}\right]$$
$$\Delta \alpha = \Delta n_e + \Delta n_h = 6 \times 10^{-22} \Delta N_e + 4 \times 10^{18} \left(\Delta N_h\right)^{0.8} \tag{4.4}$$

4.2.2 Franz Keldysh effect in Ge

This is an electroabsorption effect known to occur in bulk semiconductors when they are under the effect of an external electric field. It was first independently observed by Franz[95] and Keldysh[96]. At the band edges, the electron and hole functions are oscillatory. However, on applying a bias, these wavefunctions are transformed into airy functions. In order to better illustrate this phenomenon, (see fig. 4.1) consider a semiconductor with a direct gap ϵ_g, at the classical turning points A and B, the wavefunctions are oscillatory i.e $\psi = u^{ikx}$. On applying a field, the evanescent tails of these wavefunctions extend into the bandgap, ie. they become airy functions within the gap. This results in a certain probability of electrons tunneling into the bandgap. When there is no photon present, the electron has to tunnel through a barrier of height ϵ_g and thickness d = $\frac{\epsilon_g}{qE}$. When a photon of energy less than the bandgap is present, the tunneling barrier thickness is further reduced to $d = \frac{\epsilon_g - h\omega}{qE}$. This results in an increase in overlap of the wavefnction tails and the valence electrons which further assists the valence electron in tunneling through the bandgap. The relation between the absorption coefficient and electric field is given as[97]:

$$\alpha = K \left(E'\right)^{\frac{1}{2}} \frac{1}{8\beta} exp\left(\frac{4}{3}\beta^{\frac{3}{2}}\right) \tag{4.5}$$

$$E' = \left(\frac{q^2 h^2 E^2}{2m^\star}\right)^{\frac{1}{3}} \tag{4.6}$$

$$\tag{4.7}$$

$$\beta = \frac{\epsilon_g - h\omega}{qE} \tag{4.8}$$

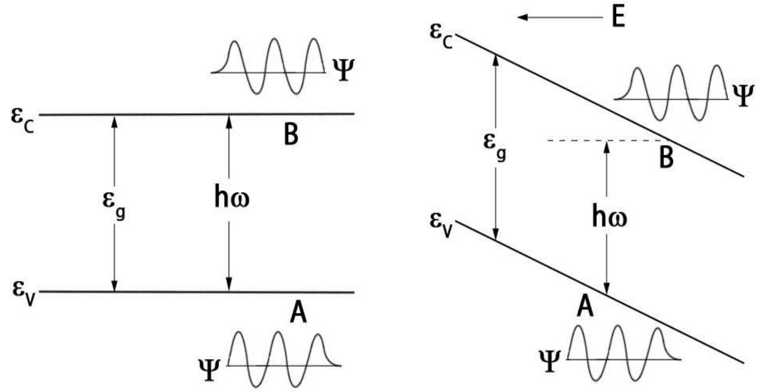

Figure 4.1: *Schematic representation of the Franz Keldysh effect, left(without field) and right(with field).*

K here is a material dependent parameter. The FK effect has been previously investigated in bulk Ge for low fields near the bandedge[98, 99] where near the direct edge of Ge, the absorption coefficient is found to have increased abrubtly from 10^2 to $10^4 cm^{-1}$. The achievable absorption contrast ratio $\Delta\alpha/\alpha$ usually due to the FK effect has typically being found to be averaged around 3[103–105]. In some cases values as high as 4 have been reported[106].

Effect of Tensile Strained Ge on Si

Ge is sometimes viewed as a quasi-direct gap material due to its unique band-structure. It has a direct gap at the Γ valley at 0.8 meV and an indirect gap at the Ł valley at 0.66 meV(fig. 4.2). This difference between the two gaps can be further reduced by introducing a biaxial tensile strain. It has been recently reported that with a 0.2% tensile strain, the direct gap is reduced by 0.03 meV [100, 101] which red shifts the absorption range of Ge on Si materials from C band ie. 1550-1560 nm to L band(1560-1630nm). The origin of this tensile strain can be explained by the difference in thermal expansion coefficients. Due to a 4% lattice mismatch, compressive strain is absent during the initial stages of growth on Ge on Si. However on decreasing the temperature from growth annealing conditions to that of room temperature, a strain builds up due to difference in thermal coefficients of Ge and Si. As Ge has a larger expansion coefficient, the decrease of Ge lattice constant is suppressed by the thick Si substrate during cooling. This hitherto results in tensile strain. In Leti we have measured the optical absorption

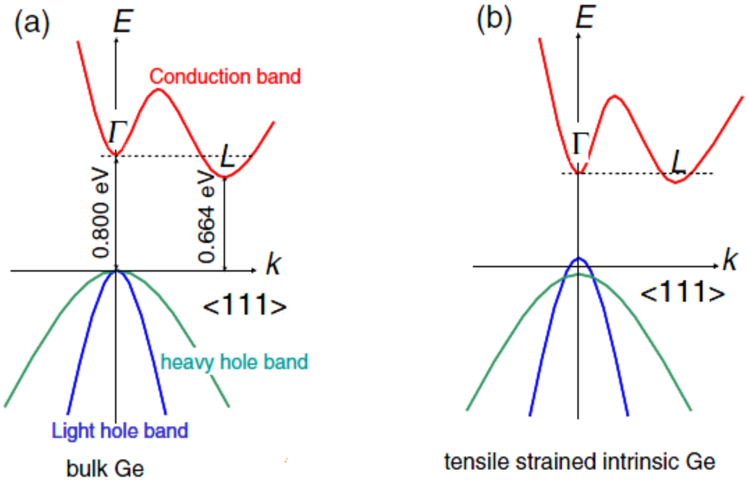

Figure 4.2: *Schematic of band gap of (a) bulk Ge and (b)strained Ge on Si. There is a 136 meV difference between direct* Γ *and indirect L valleys. This difference between the two gaps can be reduced by introducing tensile strain*(adopted from [102])

of both bulk and epitaxial Ge on Si. This data is presented in fig. 4.3 The plot indeed shows a noticible shift in the absorption edge for epitaxial Ge.

Since a detailed analysis of FK phenomenon in Ge and the effect that strain has on it is beyond the scope of this work, we shall hereby focus on the effects that this strain has on the optical properties of Ge and its relevance to photonic devices.

4.3 Modulator Overview

An optical modulator is a critical component of any integrated photonic circuit. It is a device that induces a change in the optical field due to an applied signal that is typically an electrical one. This change in the optical field is usually facilitated by a change in the refractive index of the material. In silicon the most widely accepted means of inducing a refractive index change is through the free carrier plasma dispersion, as discussed above. Apart from this other electro-optic mechanisms such as Kerr effect may also be possible although they are not so strong as the former. Thermo-optic effect which is based on thermal processes may also provide a potential mechanism for modulation although it is quite slow and can be used only upto 1MHz frequencies[107]. In FCPD, essentially a change in the free carrier density induces a change in the refractive index. FCPD based Si electro-optic modulators have been extensively researched in past. The earliest of these designs were based on a cross switched p-i-n diode in which

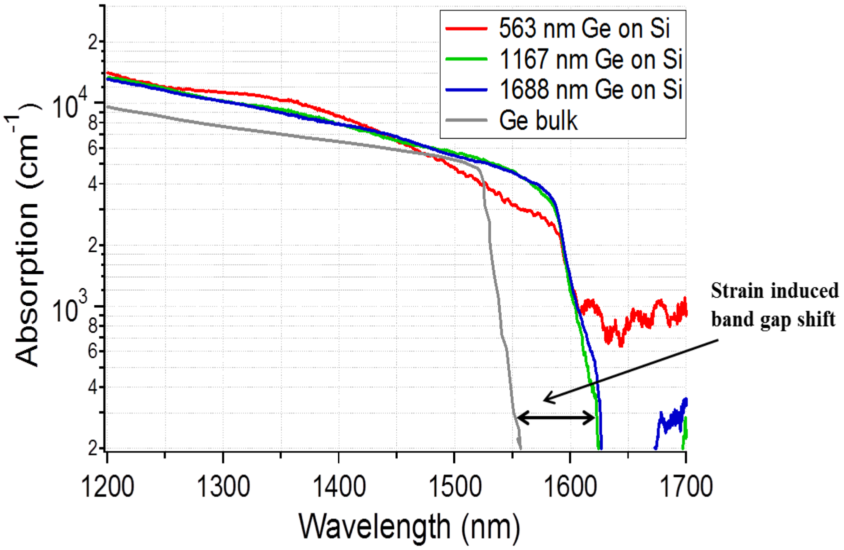

Figure 4.3: *The wavelength dependent optical absorption of bulk Ge as well as Ge on different Si substrate thicknesses(characterization data from LETI). At 1550 nm the losses are 300 cm*$^{-1}$. *There seems to be a noticible red-shift in the absorption adge for strained Ge on Si.*

active switching is achieved by carrier injection from a forward biased p+/n junction into the intersection of two crossing waveguides. Since the FCPD effect is relatively weak, this design turned out to be of several mm long and thus considered to big for chip level integration[108–111]. Later designs involved the use of a Mach Zehnder interferometer(MZI)[114–117] based structure in which light in one of the two arms was phase shifted by applying a bias and the arm length adjusted to cause constructive or destructive interference at Off or On states. The MZI design significantly reduced the device footprint, but were still several hundred microns long. In addition to that the earliest of these designs incorporated a large rib waveguide as the intrinsic region of the p-i-n layer, a result of which was the low modulation speed typically of 20 MHz due to the large free carrier recombination time in the waveguide. In subsequent designs, the width of the intrinsic ridge layer was considerably reduced[112], thereby allowing high speed operation. Metal oxide semiconductor(MOS) based designs have also been investigated in order to achieve high speed operation. In [124], Liu *et al* demonstrated 1 Gb/s speed with a MOS structure using a MZI which was the first work to show high speed modulation. However owing to the weak dependence of the silicon refractive index change on the free carrier accumulation region due to the low overlap between

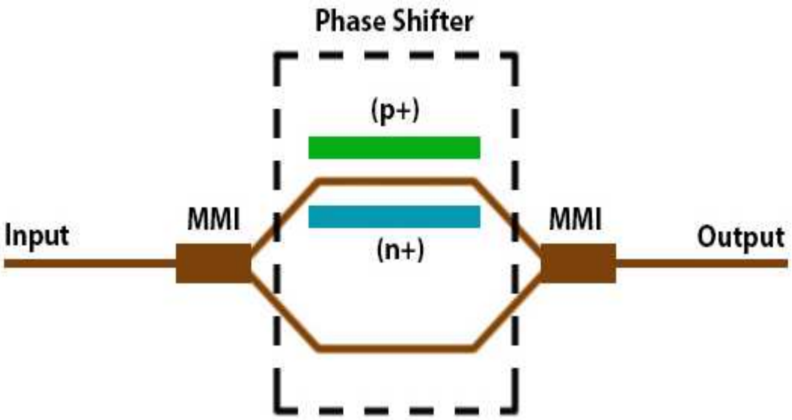

Figure 4.4: *Schematic of a MZI modulator where one of the arms is phase shifted on applying a bias(from [117]). MMI splitters are used to couple light to the reference and phase shifting arms.*

this region and the optical guided mode, these modulators also tended to be of mm sizes.

In order to reduce the effective device length, several solutions for incorporating a resonator such as a 1D FP cavity[118–120] and micro-ring resonators[121, 122] were proposed with the active region being of only sub micron dimensions. The advantage of using ring resonators is that a small change in the index of refraction is sufficient for completely detuning the resonant frequency, thus leading to a large modulation depth. These designs however come with a trade off of having an extremely narrow linewidth of operation of the order of 1 nm. Such a narrow bandwidth is extremely sensitive to bias and temperate variations, as well as very small fabrication imperfections.

With regard to the dilemma of finding a suitable material that can conform with the existing CMOS technology for photonic devices, Germanium could be an interesting candidate. Ge has been a known entity in the microelectronics industry ever since its beginning. In fact the first of transistors developed were modeled on Ge. The reasons for this was the ease of purifying Ge and its 3 times higher electron mobility as compared to Si. However Si eventually won the dual since Ge being of a lower band gap had a lower temperature tolerance and in addition there was no material that could provide diffusion masking like silicon dioxide. However the direct bandgap of Ge (E_γ = 0.8 eV) corresponds to the optical communication wavelength 1.55μm which makes it a suitable candidate for developing active photonic devices. Just as observed in the

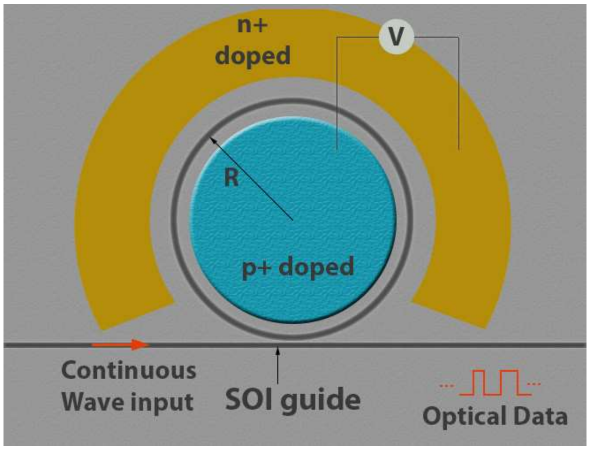

Figure 4.5: *Top view cross section of an SOI ring modulator (from [121]).*

case of III V materials, the direct gap absorption in Ge can be modified by applying an external electric field which is also known as the electroabsorption(EA) effect. The two dominant mechanisms in semiconductors for inducing the EA effect are Quantum confined Stark effect(QCSE) and Franz Keldysh(FK) effects. Both are electro-absorbtion effects i.e they induce a change in the optical absorption of the material. While the former occurs in quantum well structures, the latter is largely present in bulk materials. Electroabsorption due to QCSE in Ge has been demonstrated in the past[125–129]. Although typically QCSE is stronger than FK effect due to quantum confinement, considering that it is much easier to grow epitaxial Ge on Si than multiple Ge quantum wells on the same with CMOS process, FK effect would be the preferred choice of inducing electroabsorption for waveguide integrated modulators. The first conclusive study of inducing FK based electroabsorbtion was first done by MIT in 2007 [130] using a GeSi active layer consisting of a 30 μm heterojunction p-i-n diode butt coupled to a Si waveguide. Electro absorption is induced when an electric field is applied to GeSi under a reverse bias condition. The design also incorporates a GeSi photodetector. Since then many variants of this device have been demonstrated by different groups albeit with improved performance with speeds of upto 28 Gb/s being reported[131]. Some of this work is summarized in table 4.1.

Modulators Principle	year	Size (μm)	Extinc-tion(dB)	Speed (dB/s)	Energy (fJ/bit)	Spectrum nm
Si ring p-i-n injection[121]	2005	12	15	12.5	300	1
IBM-MZI injection p-i-n[115]	2007	200	10	10	50	-
Intel MZI reverse bias pn junction[117]	2007	3000	3	20	28000	32
MIT GeSi FK-EA[130]	2007	30	10	1.2	50	14
Oracle ring carrier depletion pn[122]	2011	7.5	5	25	7	1
Kotura GeSi FK-EA[131]	2012	55	6	28	60	35

Table 4.1: Recent work on high speed integrated optical modulators.

4.3.1 Designs based on the FCPD effect in Si

MZI Phase Change Modulators

The free-carrier index property of Si can be used to drive a Mach-Zachnder interferometer based phase change modulator. In this device, changing the refractive index change in one or both the arms induces a phase change giving rise to either constructive or destructive interference. The induced phase change is given by:

$$\delta\phi = \frac{2\pi nL}{\lambda_0} \tag{4.9}$$

Where L is the active arm length. Then using equation 1.3, for a device with uniform carrier concentration of 2.2×10^{17}, at a forward bias of 0.9V[94], would result in a index change of -8.8×10^{-4}. Subsequently, the length required to induce a π radian phase shift would be:

$$L = \frac{\lambda_0}{2\delta n} = 934\mu m \tag{4.10}$$

Even, though improving doping density can improve the phase change per unit length, it would still be in the range of several hundred microns and thus there is a need for even more integrated modulating schemes.

Si Ring Modulator

As an alternative to MZI designs, compact devices with high modulation can also be developed by making use of ring resonators. At the resonance wavelength, the resonator is able to trap light within its cavity by increasing its optical path length due to constructive interference. The cavity photon lifetime in the resonator is given by: $\tau = \frac{\lambda Q}{2\pi c}$, where $Q = \frac{\lambda}{\Delta\lambda}$ is the quality factor and $\Delta\lambda$ is the 3dB bandwidth at resonance. Typically the lifetime is the range of a few picoseconds which ensures fast modulation by the resonator. At all other wavelengths, the light interferes destructively within the cavity and is not transmitted. The transmission T is given by [112]:

$$T = \frac{T_{max}}{1 + \left(\frac{4nL}{\pi\Delta\lambda}\right)^2 sin^2\left(\frac{2\pi}{\lambda}nL\right)} \tag{4.11}$$

Where L is the total optical path traversed in the cavity. These waveguided resonators need to be only a few microns in diameters. For an index change of 10^{-3}, the resonance

wavelength can be detuned by 1 nm which is enough to ensure 100% modulation.
The main disadvantage of these modulators is the extremely narrow bandwidth of operation and sensitivity to temperature and fabrication inaccuracies. The problem of temperature sensitivity can be minimized by creating strain between Si and oxide layers to compensate for temperature induced index variation[113].

4.3.2 Plasmon optical modulators

Compared to guided photonic modes, plasmon modes have a highly confined mode volume and are thus promising candidates for implementing hybrid photonic-electronic devices such as modulators. Plasmonic devices with compact features would have a reduced footprint and hence reduce power dissipation. The energy per bit for plasmon modulators could be reduced by atleast a full order of magnitude compared with the best performing photonic ring modulators[18]. Several proposals on plasmon based modulators have already been designed and demonstrated such as all optical modulators using CdSe quantum dots where employing a pump beam (at 515 nm) changes the optical properties of the dot (at 1415 nm), thermo-plasmonic modulators[132, 133] which although display good thermally induced index modulation, however are greatly limited by their speed performance and electro-plasmonic modulators such as those based on ITO[134, 135], carrier accumulation in Si like PlasMOStor[136, 137], which due to their compatibility with CMOS integration and low device footprint are particularly interesting for this work. Some of these examples are briefly described below.

EA modulator based on transparent conducting oxides

This device consists of a MOS waveguide with an ultrathin active layer of indium tin oxide(ITO) incorporated in the insulator between the Si and metal. The ITO layer is highly doped depending on the oxygen vacancy and interstitial metal dopant concentrations. Furthermore, since this low index active layer is incorporated in the oxide gate stack, the coupling efficiency to the input photonic mode will be high. On applying a bias, the ITO carrier layer transforms from a near dielectric to quasi-metallic due to a change in its carrier density which in turn leads to a change in the complex effective index of the fundamental plasmon mode. The device was shown to have a high modulation depth of about 1 dB/μm and a low insertion loss of 0.2 dB/μm along with a large wavelength of operation of 1.2-2.2/μm. A schematic of the device is shown in

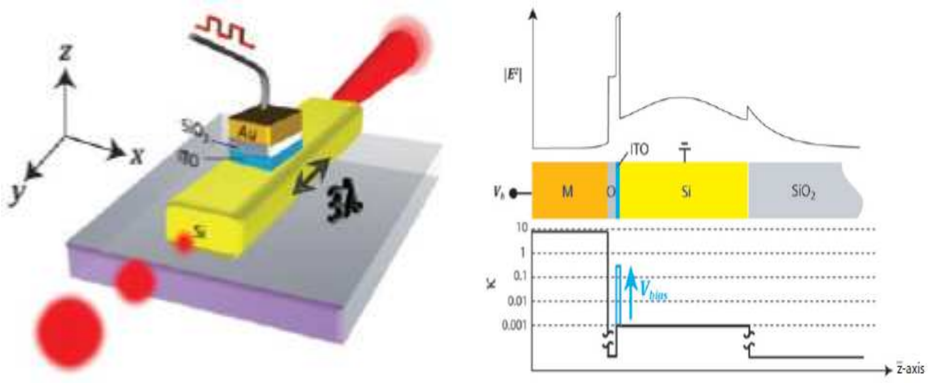

(a) (b)

Figure 4.6: *(a) A schematic of operation of the ITO based plasmonic modulator and (b) MOS cross section (from[134]).*

fig. 4.6. A critical drawback of this kind of device however is that the ITO material in itself is a known contaminant in CMOS foundaries, which can introduce defects in the fabrication process thereby inhibiting device performance.

CMOS integrated PlasMOStor

Another design also based on a MOS type design is the PlasMOStor which was first designed and conceived by CALTECH. This device works on the principal of intermodal interference. The MOS structure with a back metal supports two modes- a plasmonic mode and a photonic mode and is tailored to have a destructive interference during a normal passice state operation. In the active state a bias induced accumulation layer builds up close to the oxide layer which causes free carrier index change in the photonic mode leading to its cutoff, thereby leaving only the plasmonic mode to propagate in the device.

The concept was chosen to be adapted and developed by LETI platform for CMOS integration (see fig. 4.7) using its matured microelectronics know how in collaboration with the Atwater group at CALTECH. The electro-optical performance of the device for a butt coupled integrated configuration was however found to be very contrasting to the one observed [136] in the experimental stage using slits. The modulation depth was found to be $1.5\times10_{-3}$dB/μm with losses of about 2.6 dB/μm. This is because the power coupling to the photonic mode at cutoff was negligible compared to the

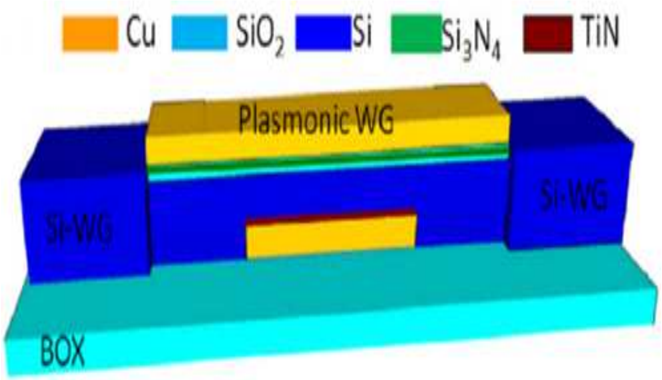

Figure 4.7: *Schematic of a CMOS integrated PlasMOStor developed by LETI (from[138]).*

fundamental SPP mode thus rendering a largely single mode operation. Although the compact features along with low power consumption (max. 120 fJ) of the device are highly desirable, the low modulation depth and higher optical losses(ostensibly due to the optical effect of the electrical contact TiN layer at the back metal)currently make device level implementation unsuitable.

4.4 Plasmon Assisted Ge on Si FK Modulator

In the following work, we propose a plasmon assisted modulator that is based on the Franz Keldysh effect in Ge effect described that was discussed in the pervious sections. Among the various plasmon guide geometries, we particularly focus on the metal slot waveguide, as in this structure, the plasmon mode is tighly confined in the slot region where depending on the gap size, there is minimal field penetration outside the physical waveguide region[139, 140]. The modal properties of such slot waveguides have been analyzed to a certain extent in the past, although not much has been done to investigate the possibility of filling this slot region with an active material.

From the fabrication point of view, bringing the metal close to the semiconductor region leads to certain amount of diffusion which requires the use of a barrier or contact material in between the metal and semiconductor. Most of the barriers like SiN, Al_2O_3 are low index materials compared to semiconductors. Since plasmons power is mostly confined at the metal dielectric interface, this might lead to less optical power traversing the semiconductor active region. Conversely most electrical contact mate-

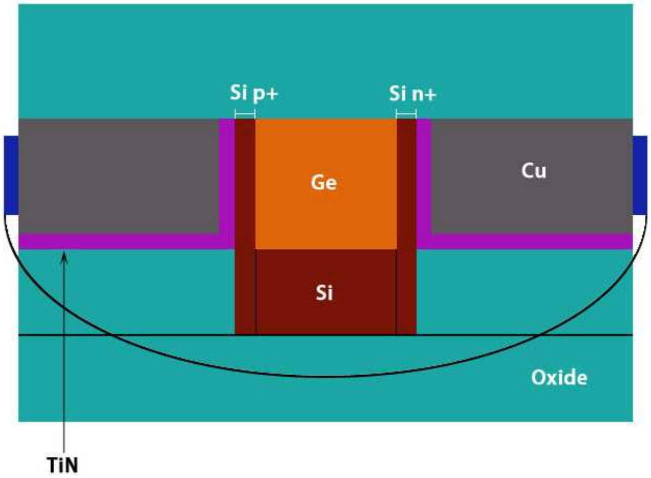

Figure 4.8: *The metal slot geometry with TiN as electrical contact. The thin dark blue films indicate the points of applying bias.*

rials which also act as barriers, tend to be optically lossy. Any design would have to address these contraints.

An ideal modulator should exhibit single mode operation, high extinction ratio, be of small device footprint and have minimal insertion losses. Even though plasmons are inherently lossy in nature, it is still possible to minimise these losses by appropriately tuning the device dimensions. To that respect a certain tradeoff could have to be achieved between confinement and optical losses. In order to do this, several parameters related to the structure will be investigated with regard to their effect on the effective mode absorption. In this study, we analyse the switching characteristics of such a waveguide by incorporating an active medium in the slot region. At each stage of analysis, we will take into account electrical performance and the limitations of device fabrications in a CMOS environment.

4.4.1 Design Considerations

For this study, we analyse two potential metal slot waveguide geometries that may be interesting for plasmon assisted optical modulation. The first one is the metal slot configuration (fig. 4.8).

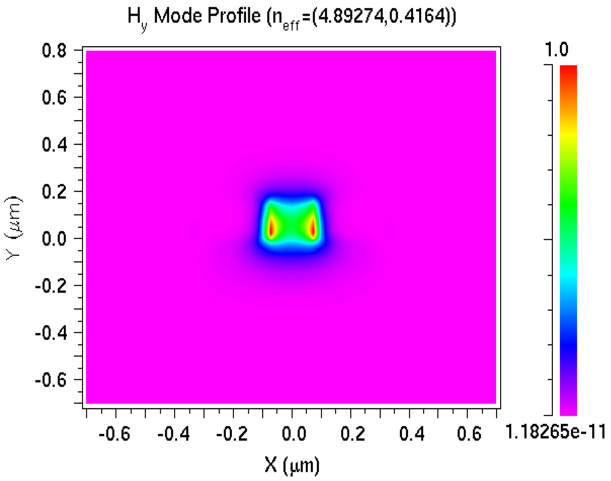

Figure 4.9: *Transverse magnetic field profile of the fundamental plasmon mode for the slot waveguide with 2 TiN contacts of 5 nm thickness. This structure would exhibit optical losses of 14 dB/μm.*

Metal slot waveguide with 2 contacts

In this design there are two Cu metal slots(each connected to a doped Ge layer through the TiN contact) with the Ge intrinsic layer in the middle. The 5 nm layer of TiN acts as the electrical contact. On applying a bias, static E field is introduced in the intrinsic Ge region, which then exhibits the Franz Keldysh effect.

Despite the high confinement of plasmons in this structure, the one main drawback of using this design is that it would be highly lossy, as shown in fig. 4.9 due to the presence of TiN layers. TiN by virtue of its optical index is highly lossy in nature. Moreover the plasmon mode will be mostly concentrated in the region around the TiN and doped interface, where the FK effect will be minimum. Since most of the electrical contacts used in the CMOS foundary as lossy, it would be necessary to find other means of applying bias, while at the same time retaining the two metal wings for better optical confinement.

Metal slot waveguide with no contacts

Keeping these considerations in mind, we invesitgate another potential geometry which we call the submarine configuration(fig. 4.10). In this structure the role of the two metal wings is limited to guiding and confining light, while there is another Cu gate

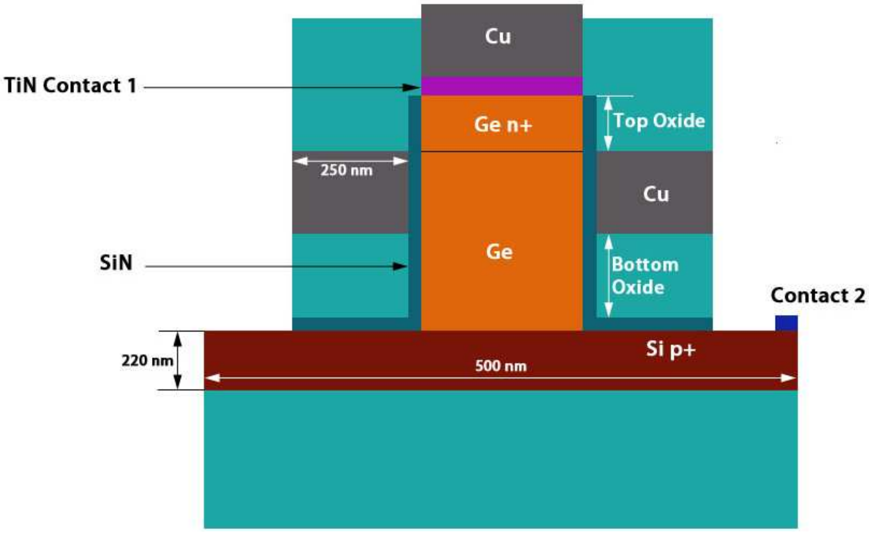

Figure 4.10: *The submarine geometry. In this case the metal slots act as an optical guide, while a Cu layer is deposited on top to serve as an electrical contact.*

metal deposited over the Ge region for the purpose of inducing the external applied E field. Contrary to the above case, a thin layer of SiN would be deposited on the metal slot guides, to prevent diffusion of Si into Ge, while the 5 nm TiN film would be instead deposited on the top Cu gate metal to make electrical contacts. The other contact would be deposited far off on the extreme end of the p+ Si inorder to minimise optical losses. The proposed design is therefore compatible with a realiable fabrication in a CMOS environment. In the following we detailed the optical analysis and give some piece of information on the electrical behavior of such a structure. On applying a bias, I will check if the E field will be induced in the Ge intrinsic region. I will also optimize the overlap between the device active region and optical mode, ie maximize the optical fields in the Ge intrinsic region by tuning the geometry of the device.

4.4.2 FEM Simulations

The mode properties of the above slot waveguide structure is studied using the finite element method(FEM) modeling package of Rsoft Inc. The optical index constants of the materials used for the simulation are as follows. Si = 3.46, Cu = 0.2+11i, SiN=2, SiO_2 = 1.44. Ge (passive state) = 4.24+0.00386, Ge (active state) = 4.24+ 0.01544i. The active state losses for Ge is taken to be 4 times that of passive state corresponding to maximum FK effect which is also consistent with the data found mostly in literature.

The wavelength of operation is taken to be 1.62 μm to account for band gap shift due to strain. The meshing is chosen to be 1 nm for the edges and 10 nm in the bulk regions. For purposes of simplicity, the FK effect is assumed to occur in the entire Ge region, although this would not be the case in the actual device since it would affect only the Ge intrinsic region. The passive state losses in dB/μm are calculated as:

$$Loss = 10log_{10}\left\{exp\left(\frac{-4 \times Im(N_{eff}) \times \pi}{\lambda}\right)\right\} \tag{4.12}$$

And the modulation depth in dB/μm as:

$$MD = 10log_{10}\left\{exp\left(\frac{-4 \times Im(N_{Pass}) \times \pi}{\lambda}\right)\right\} - 10log_{10}\left\{exp\left(\frac{-4 \times Im(N_{Act}) \times \pi}{\lambda}\right)\right\} \tag{4.13}$$

where N_{Pass} and N_{act} are the effective mode indices in passive and active states respec.

Choice of Optical Mode

A mode analysis of this device in passive state is performed, which(fig. 4.11). The analysis reveals two distinct fundamental plasmon modes, that are orthogonal to each other. For the rest of the chapter we designate the two modes as B_H and B_V corresponding to the dominant magnetic fields components in the x and y axes respectively. Either of these modes can be excited depending on the polarization state of the input SOI photonic guide. It is seen that the effective of the B_H mode is 4.81+0.5326i corresponding to a loss of 18 dB/μm. The index of the B_V mode is 3.71+0.068i corresponding to a loss of 2.2 dB/μm. Since the entire device would be encapsulated in oxide, we define the top oxide layer as the distance between the Cu metal wings and the upper TiN contact, while the bottom oxide layer is defined as the distance of the same with regard to the p+Si layer. To begin with, we first vary the top and bottom oxide layers and track the passive state losses and modulation depth of the both the B_H and B_V modes. The Cu and intrinsic Ge layer thickness is fixed at 150 nm with the width of Ge layer being 100nm. Fig. 4.12(a) and fig. 4.12(b) shows the variation of passive state optical losses of B_H mode and B_V as a function of top and bottom oxide layers in dB/μm. While fig. 4.12(c) and fig. 4.12(d) reveals their respective extinction ratios in dB/μm. From the above plots is is observed that the passive state losses of the B_H mode varies from 9 to 18 dB/μm, while the modulation depth varies from 0.26 to

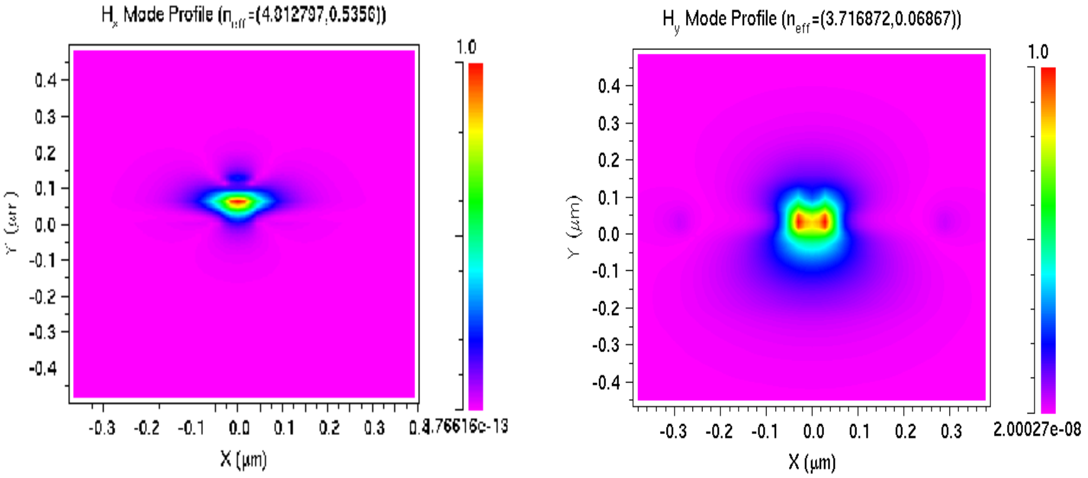

Figure 4.11: *The two fundamental plasmon modes supported by the device orthogonal to each other in passive state. On the left side is mode* B_H *with a dominant TM field in x direction and on the right side is mode* B_V *with a dominant TM in y direction due to the Cu slot guides. The passive state losses of mode* B_H *are significantly higher than that of mode* B_V

0.31 dB/μm. This would mean that a device with 3dB modulation would have to be 10 μm long and would have losses of 100 dB. This much loss would be difficult to measure and chances are that it would include too much noise. The higher losses are ostensibly due to the presence of the thin TiN film. On analysing the corresponding values for the B_V mode, it is seen that minimum loss is 1 dB/μm and maximum modulation at 0.1 dB/μm. The losses are observed to be decreased by a factor 10 since there is no TiN involved in this mode. A 3 dB device in this case would be 30 μm long but have losses of only 30 dB. The further part of this study would thus focus on optimising this B_V mode. The results indicate that there is a need to isolate the active region from the top and bottom contact levels inorder to improve both the modulation depth and decrease losses. Keeping in mind fabrication limitations, we choose the top and bottom oxide thickness for the remaining calculations to be 40 nm and 60 nm respectively. This would mean optical loss of 1 dB/μm while a modulation of 0.08 dB/μm.

Effect of Nitride barrier

As mentioned in the previous chapter of MOS waveguides, the Cu metal has a tendency to diffuse into the Si layer. To prevent this, it would have to be necessary to incorporate a thin nitride barrier. For the next calculations, it is interesting to see

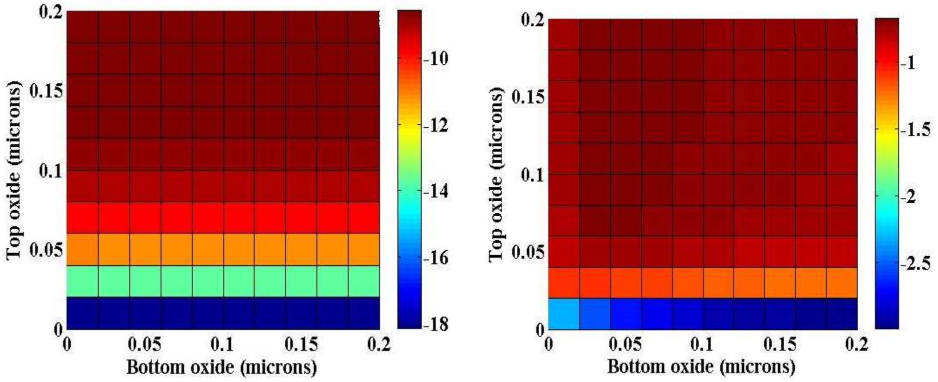

(a) $\mathbf{B_H}$ **mode** (b) $\mathbf{B_V}$ **mode**

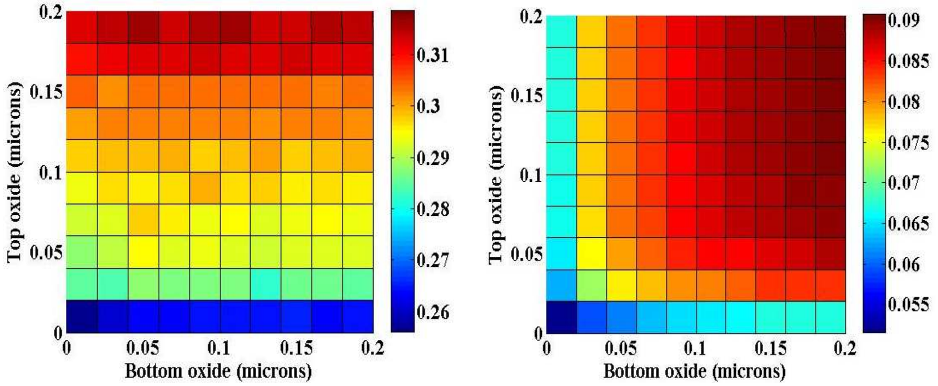

(c) $\mathbf{B_H}$ **mode** (d) $\mathbf{B_V}$ **mode**

Figure 4.12: *(a)-(b) Passive state losses of B_H and B_V modes and (c)-(d) their corresponding modulation depths as a function of top and bottom oxide layers in dB/μm respectively.*

how this nitride barrier would affect the modal properties of the plasmon mode. To that respect, fig. 4.13(a) and fig. 4.13(b) illustrate the behaviour of the B_V mode with regard to the SiN thickness. In all the calculations, the Cu thickness was fixed at 170 nm. According to these curves, a higher SiN thickness means less loss but much lesser modulation. For e.g for a Ge width 100 nm, the passive state losses are observed to be around 0.6 dB/μ while the modulation is reduced to 0.15 dB/μm. To understand this effect better, we analyse the E field profiles of the B_V mode at different SiN thicknesses, as shown in fig 4.14. It is seen that at higher SiN thicknesses, a part of mode is pushed further into the nitride barrier, due its lower index. While this would entail lower losses, it would also reduce the effectiveness of the FK induced absorption as there is less field in the Ge layer. In another sense however it is better to have a thicker

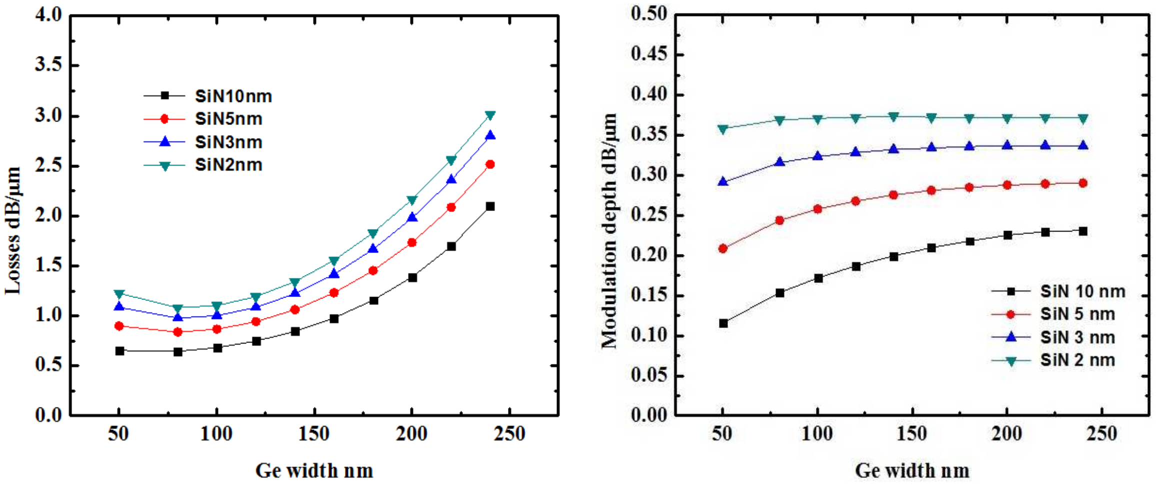

(a) (b)

Figure 4.13: *(a) Passive state optical losses of mode* B_V *and (b) extinction ratio of mode* B_V *as a function of Ge width at differet SiN thicknesses.*

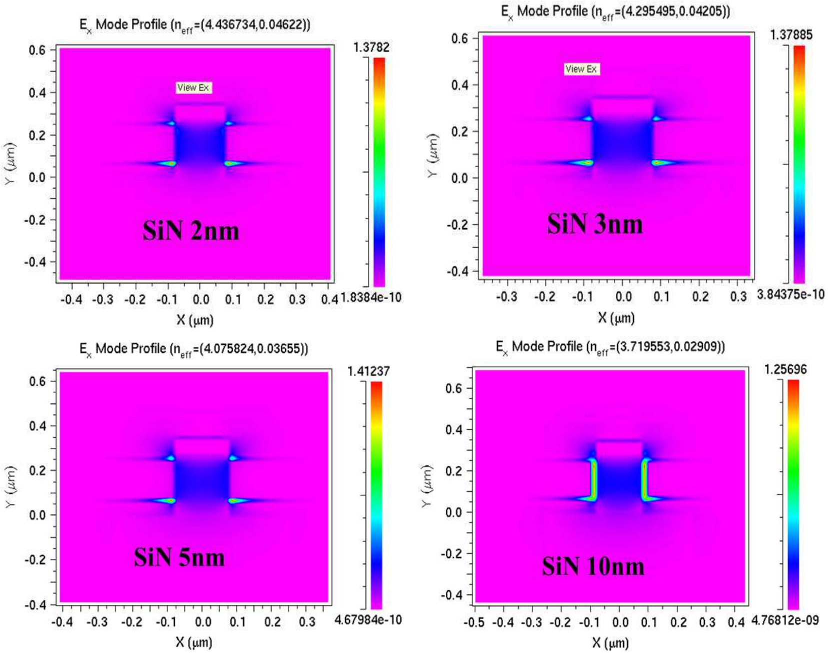

Figure 4.14: *Ex field profile(which is the dominant E field component of the* B_V *mode) for different SiN barrier thicknesses. As the SiN layer thickness increases, the imaginary part of mode index is also reduces, which inturn reduces the losses.*

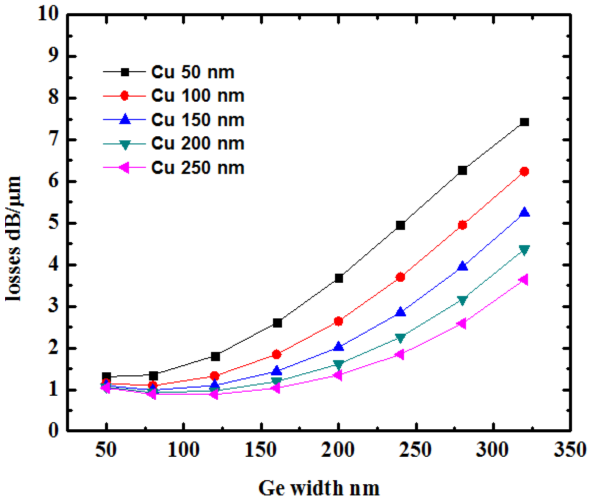

Figure 4.15: *Variation of passive losses of B_V mode as a function of Ge width at different Cu wings thicknesses. At higher the wing layer thickness, the losses are observed to saturate on the lower side.*

nitride layer as this would reduce the possibility of Cu diffusion. Again keeping in mind fabrication limitations, we believe that a nitride barrier of 3 nm thickness should be sufficient to ensure device reliability. These results indicate that a compulsory trade off in the dimension of the slot SiN layer is key for achieving a high performance modulator

Effect of Cu thickness

Finally for the remaining analysis, we study the effect of different thicknesses of Cu metal wings on the B_V mode. The details of this study are ploted in fig. 4.15 and fig. 4.16. We observe that higher the Cu metal wing thickness, lower the losses and higher the modulation. Above 250 nm Cu thickness however, both the losses and modulation depth start to saturate. Since we would like to work at minimal Ge width, to take advantage of the confinement properties of slot geometry, from the technological point of view, it would be difficult to fabricate a device with a very high thickness/width ratio. From the plot we observe that a reasonable Cu thickness would be 150 nm, which would encompass passive state losses of 1 dB/μm and an extinction of 0.3 dB/μm.

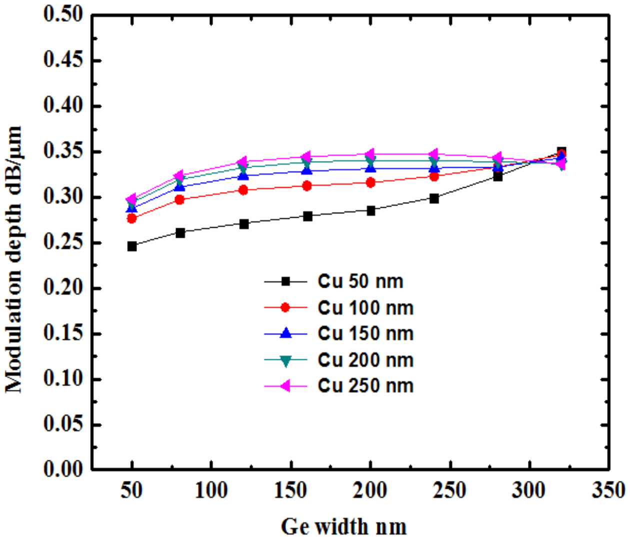

Figure 4.16: *Variation of extinction ratio of mode B_V as a function of Ge width at differet Cu wings thicknesses. The modulation depth begins to saturate at higher wing thicknesses.*

Effect of Ge layer

The above plots show that both in the case of Cu and SiN thicknesses there is no significance dependence on the Ge layer dimensions on modulation depth. The results are markedly different in the case of losses however. At higher Ge widths, the losses are observed to considerably increase. Such increase in losses has been reported previously [59] and can be attributed to the tighter field confinement in the SiN slot region and the losses due to the metal becoming more dominant. In order to minimize the losses without compromising the modulation, an optimal Ge width of 120 nm should be suitable for the final device fabrication.

4.4.3 Final Design

The final device design, which would incorporate all of the above optimised parameters. A schematic of this design is shown in fig. 4.17. This would include a Ge intrinsic layer of 120 nm width and 200 nm height on top of a doped p+ Si layer. An n^+ Ge layer of a similar width and 50 nm height would be deposited over the intrinsic Ge layer. This top side doped Ge layer would also overlap with the oxide layer, which would additionally serve to isolate the metal wings from the TiN contact above. The two Cu metal wings should be of 150 nm thickness and seperated from the Ge layer by a 3

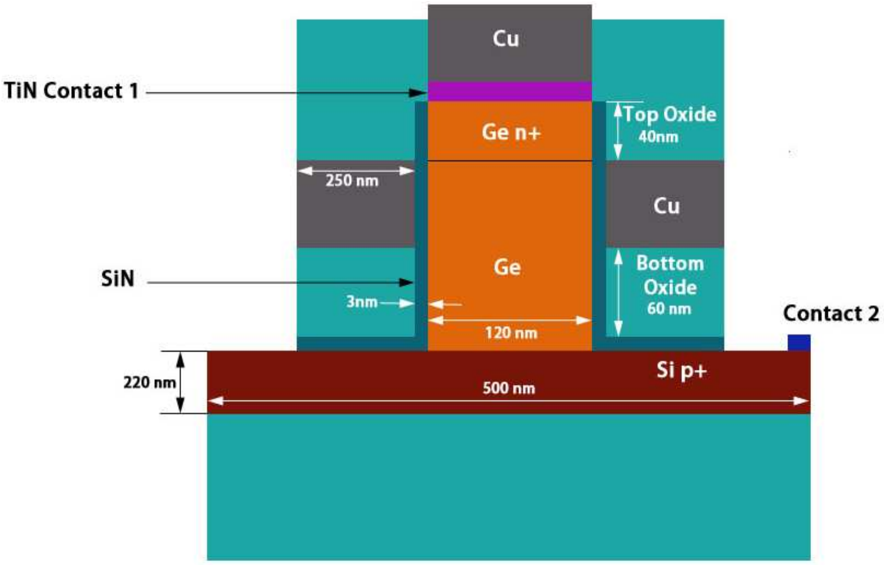

Figure 4.17: *Optimised device design for an plasmon assisted Ge modulator.*

nm nitride barrier. Also, keeping in mind the results of fig. 4.12, the intrinsic Ge layer must exceed the Cu wing thickness by 50-60 nm to minimize plasmon losses. This would entail an overall intrinsic Ge layer thickness of over 200 nm. The device would have losses of about 1 dB/μm and an extinction of 0.3 dB/μm. A 3 dB device would then be of 10 μm length and of 10 dB losses. The higher losses are due to the confinement properties of the slot waveguide as also the fact that Ge being a high index material leads to more of the plasmon mode pushed into the metal. The figure for losses does not account for coupling losses that would occur when light is coupled from an SOI guide. On comparison with recently implemented photonic modulators, we observe that this device would be of much lower size, albeit however with much higher losses.

4.4.4 Electrical Simulations

Before converging on a final device design, it is necessary to test the electrical performance of the submarine slot Ge modulator. As the FK effect is dependent on the magnitude of E field, it is necessary to channel maximum E field into the intrinsic Ge region. An electrical simulation in this regard, would best mimic the actual device operation. These simulations were performed by Delphine Marris-Morini at IEF Paris-Sud, using the Dessus package.

For the simulations, the intrinsic Ge region is chosen to be 100 nm wide and 250 nm in thickness. The n-doped Ge layer is 50 nm thick. The Cu metal wings are 50 nm thick and 500 nm wide. A bias is applied between the contact point of the top Cu metal gate and another point on the Si layer. A residual doping of $10^{16} cm^{-1}$ was considered for the p+ region and $10^{19} cm^{-1}$ for the n doped Ge layer. The simulation is performed for calculating the electric field by solving the poisson's equation and the equation of continuity for both electrons and holes. The bias voltage is varied between 0 and 5 V. The results are summarised in fig. 4.18 It is observed from this data that the static E field inside the intrinsic Ge region is minimum. A cause of this could be the two metal wings that induce screening effects of charges. To further investigate this, the calculations are again performed for a device without any metal wings. These results are depicted in fig. 4.19. In this case the static field in the intrinsic Ge region is much higher than in the case where the metal wings were present. A way to circumvent this problem might be by applying an additional third bias in one or more of the metal wings. This work is ongoing pending further results.

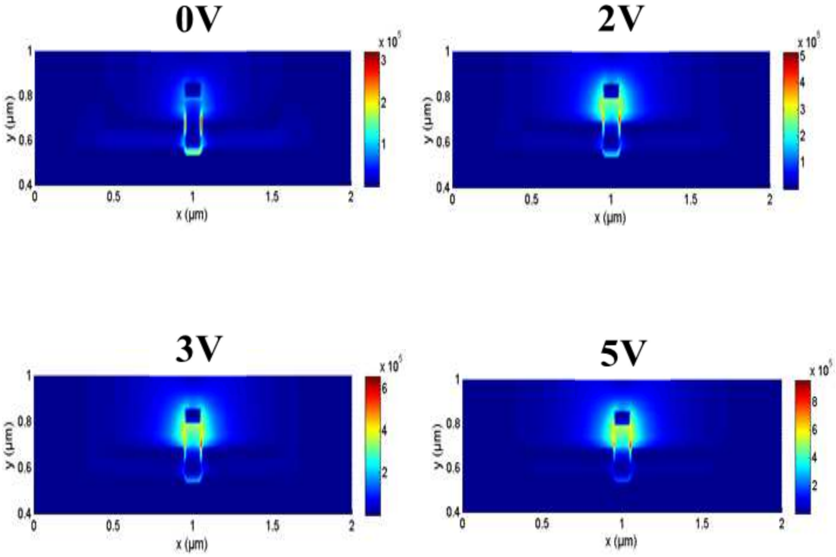

Figure 4.18: *The device static E field at different applied bias. The field inside the intrinsic Ge seems to be much less as compared to that in* n^+ *Ge.*

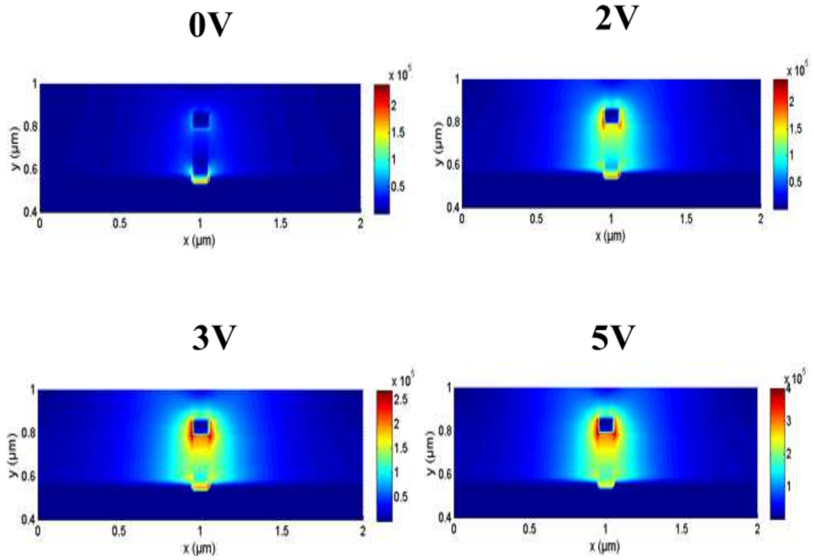

Figure 4.19: *The device static E field at different applied bias voltages for a device without any metal wings. In this case, there is considerable field inside the intrinsic Ge layer as compared to the previous case shown above.*

4.5 Conclusion

The goal of this work was to model a plasmon assisted modulator based on the Franz Keldysh effect in Ge. As such we have investigated the metal slot geometry for designing an EA modulator. On analysing the modal characteristics of this device, it is seen that for an optimal geometry for a 3dB modulation this device would have 10 dB losses. The calculated modulation, although sufficient for conceiving a compact design, is primarily offset by even higher plasmon losses.

We further also analyse the electrical behaviour of this device through simulations. It is seen that the static electric field(critical for inducing the FK effect) is present in the Ge intrinsic layer(which is also the active region) only if the metal wings are not present. To address this issue, it would be interesting to study a similar design by using low loss optical materials like TaN as electrical contacts.

On the whole, the task of designing a compact integrated EA modulator is challenging, especially given the technological constraints imposed by the CMOS environment which restricts the available options in terms of design and materials. Nevertheless, several other designs still remain to be investigated in this regard before fabricating and testing a prototype device. This work is presently being continued in the framework of the MASSTOR project.

Chapter 5

Modeling of Optical Antenna based Ge Photodetector

5.1 Introduction

The field of optical antennas has attracted wide interest in the past few years over many potential applications due to its unique properties of guiding and confining light to the nanoscale dimensions using surface plasmons. A critical challenge to developing optical antennas operating in visible and near infrared region is their small geometries, which often require sub-50 nm lithography technique for their fabrication. However with the recent development in nanotechnology, the fabrication of antenna based structures has now become feasible.

Most of the integrated circuits are based on Si due to its well developed fabrication techniques. However due to its indirect band gap being at 1.12 eV, Si is optically transparent for wavelengths above 1.1μm. This work is dedicated to optimizing an optical antenna design to improve the performance of SiGe dot based near infrared photodetector. The study would involve extensive use of computational techniques such as the boundary element method(BEM) as well as FDTD. Also discussed would be the effect of substrate on the overall antenna performance. In the beginning a brief overview of classical antenna theory is discussed. Comparisons will be drawn with optical analogies.

An antenna functions on the principle that free charge carriers that are constrained in a certain region of space may oscillate if an external AC voltage is applied or if disturbed by an EM wave in regions of space. Antennas in the field of radio frequencies were first demonstrated by Heinrich Hertz and later by Guglielmo Marconi who is credited to have pioneered the field of radio wave communication. Hertz had in 1887 demonstrated that radio signals were electromagnetic waves, like light. His experiment consisted of a very primitive RLC circuit that, when discharged, produced an oscillatory current that circulated along a wire of a length comparable to the wavelength of the current. Like the induction field, the electromagnetic wave is created by an electrical current moving in a conductor. Unlike the induction field, however, the radiated field leaves the conductor and propagates through space as an electromagnetic wave. Antenna designs have already been well developed where they are used as signal transmitters as well as receivers of radio frequencies that are now deployed extensively for commercial applications in communications as well as defence networking. The typical size of these designs range from hundred meters to a couple of millimeters.

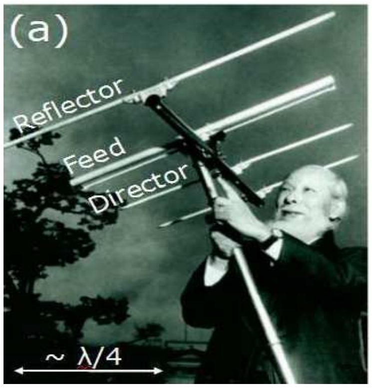

Figure 5.1: *A typical Yagi Uda RF antenna held by one of its inventors Hidetsugu Yagi. It has one reflector and two directors(adopted from[141]).*

5.2 Antenna Theory

5.2.1 Dipole Antenna

The analogy drawn by a two wire transmission line is the most simplest form when it comes to describing an antenna system[142]. It basically consists of two wires, each of length L terminated by an open end that are driven by a high frequency voltage source. The current in this case is reflected at the terminal ends, which results in a standing wave along the line. Even though this current is time harmonic with a spatially varying amplitude, it does not radiate into the far field if the gap between the wires is small. This is because the current in each wire has an opposite phase and so the

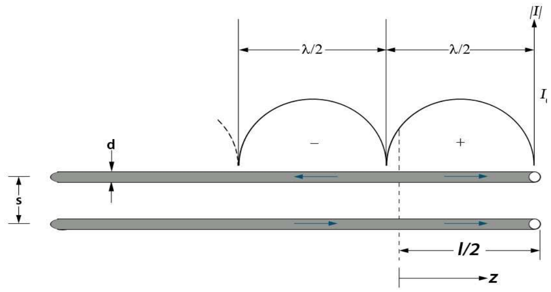

(a) A two wire transmission line

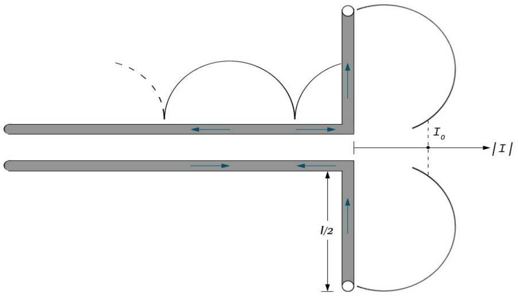

(b) Linear Dipole

Figure 5.2: *The two wire transmission line and the linear dipole.*

radiation at far-field tends to cancel each other due to destructive interference. Now, if the end of the two wires is bended at a certain distance from the ends by 90° each in opposite direction, the resulting structure is transformed into what is known as a *dipole antenna*. In this structure, the current distribution at either ends is totally in phase due to which it radiates much more efficiently. For an infinitely long transmission line the characteristic impedance Z_0 is defined as the ratio of the voltage between the transmission lines and the current in the wire i.e

$$Z_0 = \frac{U(z)}{I(z)} \tag{5.1}$$

which is independent of the position z along the line. This impedance depends solely on the materials used and the geometry of the structure. The current distribution I(z) of antennas with extremely thin wires compared to the wavelength is described by a sinosoidal relation:

$$I(z) = I_{max} sin[k(\frac{1}{2}L - |z|)] \tag{5.2}$$

This current distribution is however valid only for unbend transmission lines as opposed to bend lines which are regarded as resonant circuits having a complex impedance Z_L

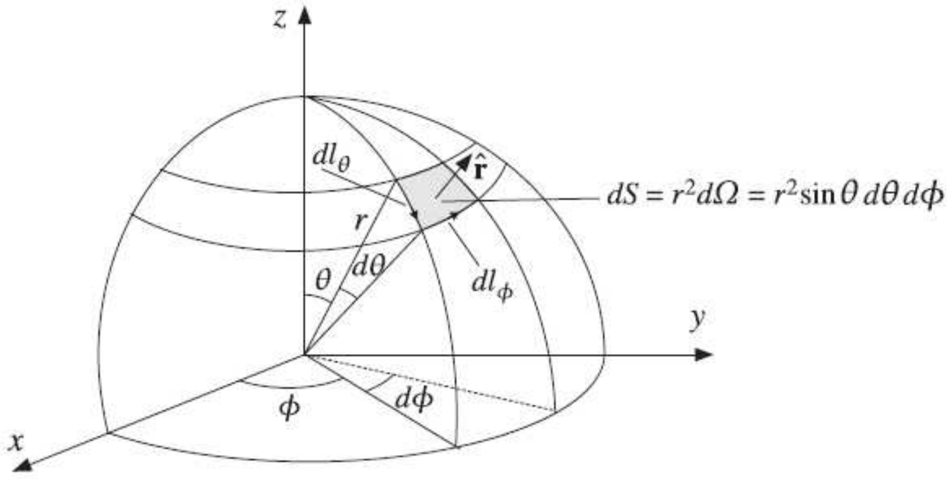

Figure 5.3: *Co-ordinate system for antenna analysis.*

resulting in some reflection at the bending points and a shift in the standing wave patterns. The impedance in this case is the ratio of the voltage at each terminals to that of the current flowing in each arms. $Z_L = \frac{U(0)}{I(0)} = R_L + iX_L$ with R_L the resistive impedance. Antenna resonance at driving frequency occurs when the complex part of impedance $X_L = 0$.

5.2.2 Antenna parameters

Now the total radiation intensity of an antenna is expressed as the time averaged Poynting vector per unit solid angle:

$$U\left(\theta, \phi\right) = \left(\frac{dP}{d\Omega}\right) \tag{5.3}$$

The total irradiated power is obtained by integrating over all solid angles $d\Omega = \sin\theta d\theta d\Phi$

$$P_{rad} = \int_0^\pi \int_0^{2\pi} U\left(\theta, \phi\right) d\Omega \tag{5.4}$$

where $d\Omega$ is the solid angle. We describe U_I as the isotropic radiation intensity over all solid angles and U_T as the total power intensity. As such

$$U_I = \frac{P_{rad}}{\Omega_{sphere}} = \frac{P_{rad}}{4\pi} \tag{5.5}$$

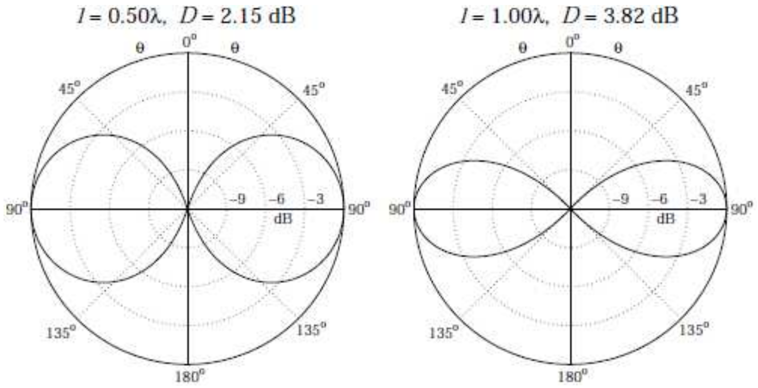

Figure 5.4: *Standing-wave dipole antenna patterns and directivities at* $l = \frac{\lambda}{2}$ *and* $l = \lambda$ *(from [142]).*

On the other hand the total power intensity may be defined as the one which also includes the non radiative intensity

$$U_T = \frac{P_{rad} + P_{nrad}}{4\pi} = \frac{P_T}{4\pi} \tag{5.6}$$

Where P_T is the total power absorbed at the antenna which also includes other loss mechanisms like ohmic losses and currents flowing in the antenna as well as losses of the surrounding dielectric media. As the total absorbed power P_{rad} is determined by the real part of antenna impedance, R_L which also includes ohmic losses R_{nr} as well as radiation losses R_{rad}, we have the radiated power, also known as the radiation resistance$P_{rad} = \frac{1}{2} R_{rad} I_0^2$ where $R_L = R_{rad} + R_{nrad}$. η known as the radiation efficiency may also be defined in terms of radiation losses as:

$$\eta = \frac{R_{rad}}{R_{rad} + R_{nrad}} \tag{5.7}$$

The antenna directivity towards a given direction $D(\theta, \phi)$ is defined as the radiation intensity normalized by the isotropic radiation intensity. This directivity is often expressed in dB.

$$directivity \;\; D(\theta, \phi) = \frac{U(\theta, \phi)}{U_I} = \frac{U(\theta, \phi)}{\frac{P_{rad}}{4\pi}} = \frac{4\pi}{P_{rad}} \frac{dP}{d\Omega} \tag{5.8}$$

Another important figure of merit is the antenna gain $G(\theta, \phi)$ which is also defined as the ratio of the radiation intensity to that of the total input power at the terminals.

$$\begin{aligned} G(\theta, \phi) &= \frac{U(\theta, \phi)}{\frac{P_{rad}+P_{nrad}}{4\pi}} \\ &= \eta D(\theta\,\phi) \end{aligned} \tag{5.9}$$

Like directivity the gain factor is also measured in dB. As both the directivity and antenna gain are frequency dependent, it is necessary to specify the bandwidth of operation.

5.3 Antennas at Optical Frequencies

In the RF regime, metals are regarded as near perfect conductors with an infinitely large negative permitivity ϵ. In the optical region however, the ϵ is a finite term with a complex value which depends strongly on the wavelength of excitation as is concrued from the plasmon dispersion relation. Any analytical description of optical antennas would have to take into account this dispersion relation due to which the surface waves at the metal dielectric interface is much smaller than the free space wavelength. In this region, it would be prudent to treat the antenna element as a strongly coupled plasma.

In the case of metal nanoparticles, of just a few nanometers size, light can easily penetrate the entire structure and cover all the conduction electrons. This leads to a displacement of the conduction band electrons with respect to the positive ion cores. As a consequence, a restoring force is developed due to the resulting electric dipole and the particle behaves like a light driven harmonic oscillator with some ohmic losses. The physical effects of surface plasmons on nanoparticles can thus be defined by the oscillator model. The associated surface plasmon resonances may be found in different regions of visible and infrared alike depending on the particle shape, size, dielectric environment and the material. When compared to the scale of incident wavelength, nanoparticle resonances are often localized and are termed as localized surface plasmon resonances(LSPRs). Here the main factor to be considered is excitation of a specific wavelength. When dealing with non spherical particles however, the polarization direc-

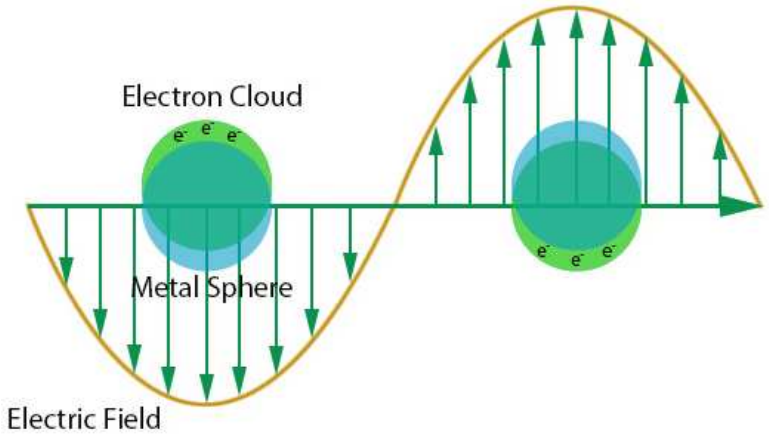

Figure 5.5: *Localised plasmon oscillations in metal nanoparticles due to coupling at resonance wavelength.*

tion also needs to be considered.

For particles with spherical geometries, the Mie theory[144] analytically predicts the scattering and absorption coefficients by determining the excitation strength of the different dipolar and multipolar modes, by expansion of the incoming field into vector harmonic functions. For particles of very small dimensions, the quasistatic approximation[145] is applied which gives a good agreement with experiments. In this approximation, the excitation field is assumed to be homogeneous over the particle volume. The polarizability α_i of an ellipsoidal particle parallel to the ellipsoidal axis i is expressed as:

$$\alpha_i = \frac{4\pi}{3} abc \frac{\epsilon_m - \epsilon_d}{\epsilon_d + A_i \left[\epsilon_m - \epsilon_d\right]} \tag{5.10}$$

Here ϵ_m and ϵ_d signify the frequency dependent dielectric functions of the metal and the surrounding dielectric respectively. A_i is a shape dependent constant. The terms a,b,c relate to the ellipsoid's half axes. This term is better described by the dipole approximation[146] in which the EM field due to plasmon modes on the metal nanoparticle is described by the EM field of an oscillating point dipole located in the center of the

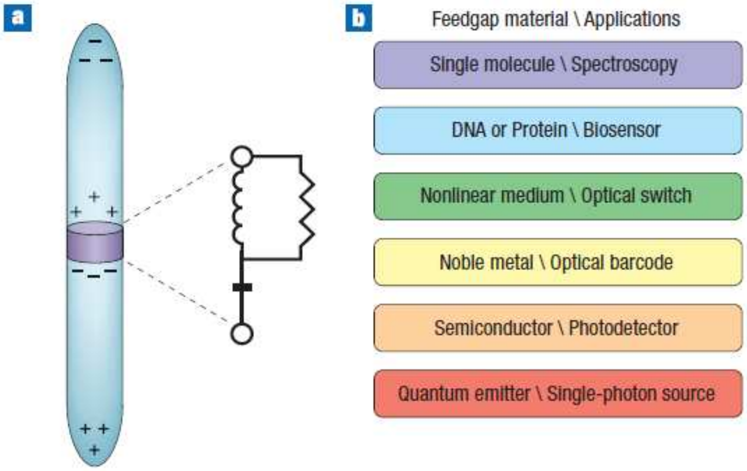

Figure 5.6: *A schematic of a nanoscale dipole optical antenna with a dielectric loaded feedgap(left).(from[143])When excited with a polarization along its dipole axis, a buildup of positive and negative charges appear on either side of the feedback. Such nanoantennas find applications in many fields.*

particle. The particle absorption and scattering cross-sections are given as:

$$C_{abs} = kIm\{\alpha\} \tag{5.11}$$

$$C_{scat} = \frac{k^4}{6\pi}|\alpha|^2 \tag{5.12}$$

Although both the scattering and absorption terms depend on the particle's polarizability α and the wave number k, their functional dependencies are different, that is to say their respective absorption and scattering maxima will be slightly different. Moreover, given the square dependency for scattering and linear dependency for absorption, for smaller particles, absorption cross section will dominate while it will be vice-versa for larger particles. It has also been shown that maximum absorption is inversely proportional to the imaginary part of particle permitivity. This could mean that lossy[144] materials like Al which are otherwise not considered for plasmonic guides, could on the other hand be used for nanoantenna applications.

At optical frequencies, the conventional half-wave dipole rule doesnt apply to thin metal rods as the metal is no longer perfectly reflecting. The half wave resonance being dependent on the material properties is incidently much shorter. The effective wavelength λ_{eff} in the case of a single infinitely long thin nanorod embedded in a homogeneous dielectric media is related to the incident radiation by the relation[147,148]:

$$\lambda_{eff} = a + b\frac{\lambda_0}{\lambda_p} \tag{5.13}$$

Here λ_p is the plasma wavelength and a and b depend on the geometry and dielectric material constants. The reduction in the plasmonic effective wavelength is a factor 2 to 6 lesser than that observed for free space for typical metals like Al, Cu for realistic antenna thicknesses.

5.3.1 Effect of Substrate

In the case of RF antennas, it is known that when an antenna is positioned over ground, the large refractive index of the substrate compared to that of air can modify the antenna emission patterns. A similar case can also be made for optical antennas. In most problems involving antennas, the resonances of nanoparticles depends mostly on the dielectric properties of the medium surrounding it.

However there are many applications that require arrays of nanoparticles to be fabricated on top of a substrate comprising glass, quartz or semiconductor with air as the cladding on top. In such cases the prediction of resonances becomes complicated and challenging. This might require tuning the substrate dimensions to match the resonance. The substrate effect can be explained in terms of the image theory[149] where there are additional image charges are produced at resonance arising from the induced polarisation in the dielectric substrate. The image theory however fails in cases where the nanoparticles are too close to the substrate, due to the effects of multipolar resonances. Recently it was shown that a higher quality factor can be achieved for the antenna by appropriately tuning the substrate spacer thickness[150].

5.4 Optical Modelling of Plasmon Photodetectors

A photodetector is a critical component of an integrated optical device whose primary function is to convert incoming radiation into electrical signal. An ideal compact integrated photodetector is expected to have a good absorption efficiency along with a fast response time. The latter quality would mean the photodetector must have a thin depletion layer which inturn increases the depletion layer capacitance and hence the response time. Thus to reduce this capacitance, it is required to reduce the photodetector active area. Most of the III-V materials are good absorbers in the near infrared region. However due to their present technological constraints, Ge (which has a comparatively lower absorption) is the preferred choice among active photodetector materials. One way to scale down the size is by employing plasmons to access the active region by employing an antenna in the photodetector vicinity. To that end plasmon based photodetectors have attracted much interest in the near[151] as well as mid-infrared regions[152–155]. It has been shown that using certain resonant antenna based geometries, such as dipole[156] and split bulls eye[157] type structures, the detector photoresponse can be considerably enhanced.

This work is based on the need to design an efficient antenna assisted near infrared photodetector. It is mainly motivated by the group of Silvano De Franceschi[158] who have been performing quantum transport measurements on a SiGe dot by contacting them with metal electrodes. These electrodes if tuned properly, can additionally serve as an optical antenna. The photodetector material for our study has been chosen to be an SiGe dot due to the fact that its lower direct bandgap of 0.8eV corresponds to the optical communication C band[159–164] and also as it is CMOS compatible, it can be easily integrated in standard foundaries. The antenna material chosen here is Al, which is also commonly used in foundaries as an electrical contact.
The standard SOI stack is used as the subsrate material consisting of an Si/SiO2 layer on which the antenna rests. Initially the BEM technique is used to optimize the 2D design. Since the 2D BEM is considerably faster as only surface meshing is required, a quick optimization of the 2D gemometry can be achieved this way. 3D FDTD simulations are then done to further investigate and optimize the 2D design obtained by BEM.

5.4.1 BEM simulation

To begin with, the optical absorption of the single SiGe quantum dot that rests on a standard SOI stack without any antenna in the vicinity is calculated. The SiGe dot is of a diameter of 80 nm and thickness 20 nm. The SOI stack consists of layers of Si of thickness t_{Si} and SiO2 thickness t_{SiO_2}. Next an antenna of length L and thickness

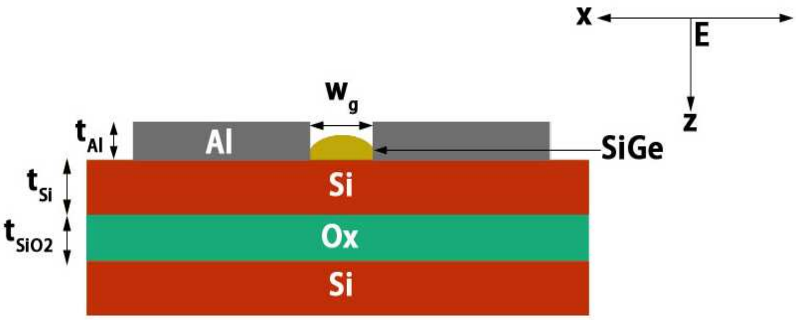

Figure 5.7: *The 2D antenna design used for the BEM study.*

t_{Al} is placed contacted to the dot. The wavelength of operation is set at 1.3 μm. A schematic of the structure is shown in fig. 5.7. The entire structure is illuminated with a linearly polarized monochromatic TM wave incident normally in which the magnetic field is perpendicular to the xz plane on which the structure rests. A convergence study is first performed to choose the optimal mesh configuration. In order to account for any spurious field divergence and scattering effects, a graded mesh configuration is chosen where the mesh in and around the dot is set at 0.5 nm as compared to the meshing of the global volume. A similar study is also done to choose the boundary of the simulation volume. The optical absorption of a quantum dot is calculated by placing an absorption box roughly of the same size as that of the dot. The optical indices used are Al=1.22+13.15i, Si=3.46, SiGe dot= 3.95+0.0001i(50 pc Ge), SiO2=1.44 [167]. The power absorbed is given as:

$$P_{abs} = \frac{1}{2} n_1 L \left\{ \frac{P_{bem}}{Z_0} \right\} \tag{5.14}$$

Where P_{bem} is the value obtained from the BEM calculation, Z_0 is the free space impedance, n_1 is the index of the incident medium and L is the lateral length of the absorption box in nm. The absorbed power is estimated in nanowatts. The standard SOI substrate chosen for this study consists of 65 nm Si and SiO2 each. Keeping in mind, fabrication limitations, the feed gap W_g which includes some part of Al overlapping on the SiGe dot is chosen to be 50 nm. Initially the absorption of this quantum dot is calculated to be 7.96e-6 nW when there is no antenna in the vicinity. Subsequently the two Al arms are placed and the absorption is then calculated as a function of thickness t_{Al} varied between 20 and 300 nm with step size of 20 nm and the length L is varied

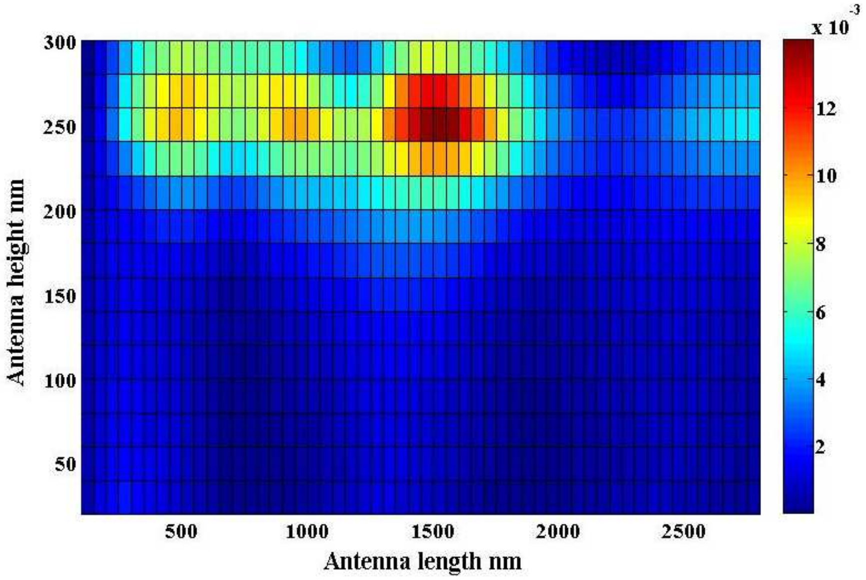

Figure 5.8: *Absorption of SiGe dot as a function of Antenna length 2L and thickness* t_{Al}*. Maximum absorption is found to be 3.71e-5 nW.*

between 50 and 1400 nm on either arms and the optical absorption is calculated in each case. The results are plotted in fig 5.8. A maximum absorption of 3.71e-5 nW is calculated for an antenna length of 1500 nm and a height of 240 nm. This would indicate a factor enhancement of about 40.

It should be pointed out that, an antenna with such thick dimensions would be difficult to fabricate. In order to thus enable an feasible design as well as improve the efficiency even further, some other factors would have to be considered.

As pointed out earlier, it would be interesting to investigate the role of the substrate. In the above calculations this substrate layer was matched to the one that is commercially available. In the following calculation the parametric sweep will be done by varying the antenna length 2L and Si thickness t_{Si}. The antenna thickness t_{Al} is fixed at 20 nm where as the total length 2L is varied between 100 and 2500 and Si thickness t_{Si} is varied between 50 and 1200 nm with a step size of 50 nm in each case. The SiO_2 thickness is set at 225 nm corresponding to approx. quarter wave plate thickness at 1.3 μm. The results are plotted in fig. 5.9(a). The maximum absorption is observed to be 8.36e-4 nW, which is for antenna length 900 nm and Si thickness 150 nm and corresponding to an absorption enhancement of 100 times.

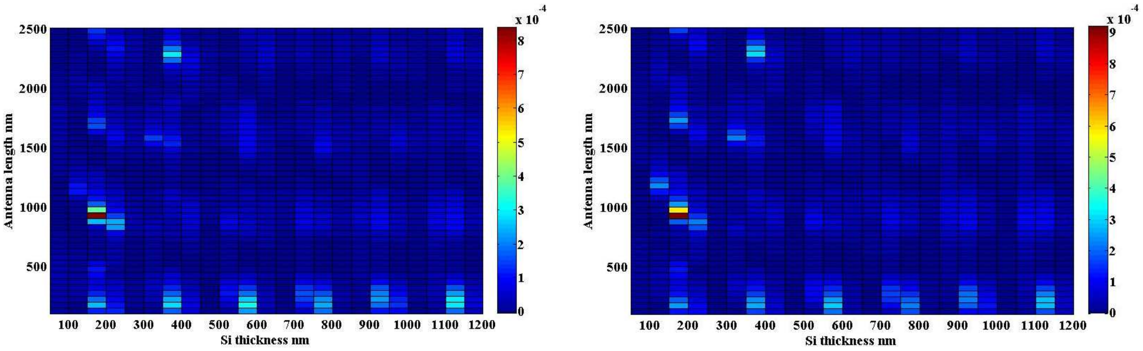

(a) $\mathbf{t_{Al}}$ **20 nm** (b) $\mathbf{t_{Al}}$ **40 nm**

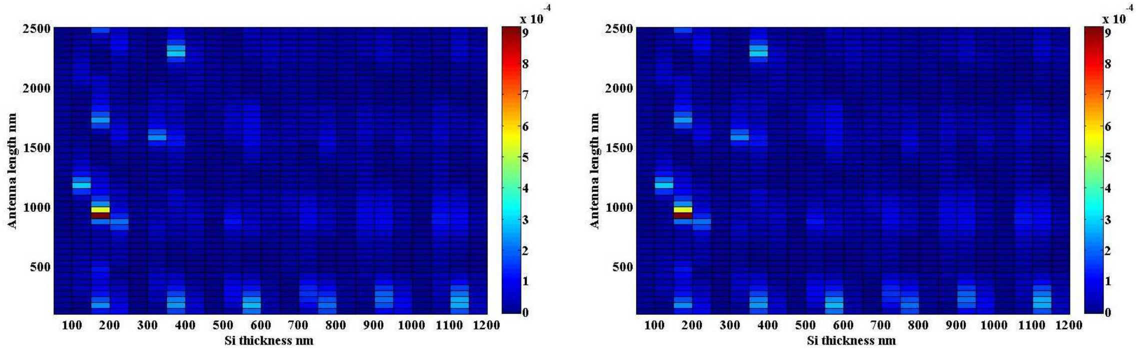

(c) $\mathbf{t_{Al}}$ **60 nm** (d) $\mathbf{t_{Al}}$ **80 nm**

Figure 5.9: *(a)-(d), Plot showing optical power absorption in nanowatts for the SiGe dot as a function of Antenna length 2L and Si thickness at different Al thicknesses. Maximum absorption observed to be for 40 nm Al thickness at 9.15e-4 nW.*

To see if there is any effect of metal thickness on the absorption, similar calculations are also performed for different thicknesses of Al(fig. 5.9).

In all the calculations at different Al thicknesses it is observed that the maxima occurs at a similar value of antenna length and Si thickness. Moreover there seems no drastic change in the value of maximum absorption. Between all the above plots, maximum absorption is recorded for antenna thicknesses 40 and 60 nm at 9.15e-4 nW. Also to be noted is that, it would be not too difficult to fabricate an Al contact of this dimension. Each of these plots also indicate a certain periodicity. To further investigate this periodicity the calculation for fig. 5.9(b) is repeated with a finer sampling in fig. 5.10. The antenna length is varied between 40 to 1800 nm while Si thickness is

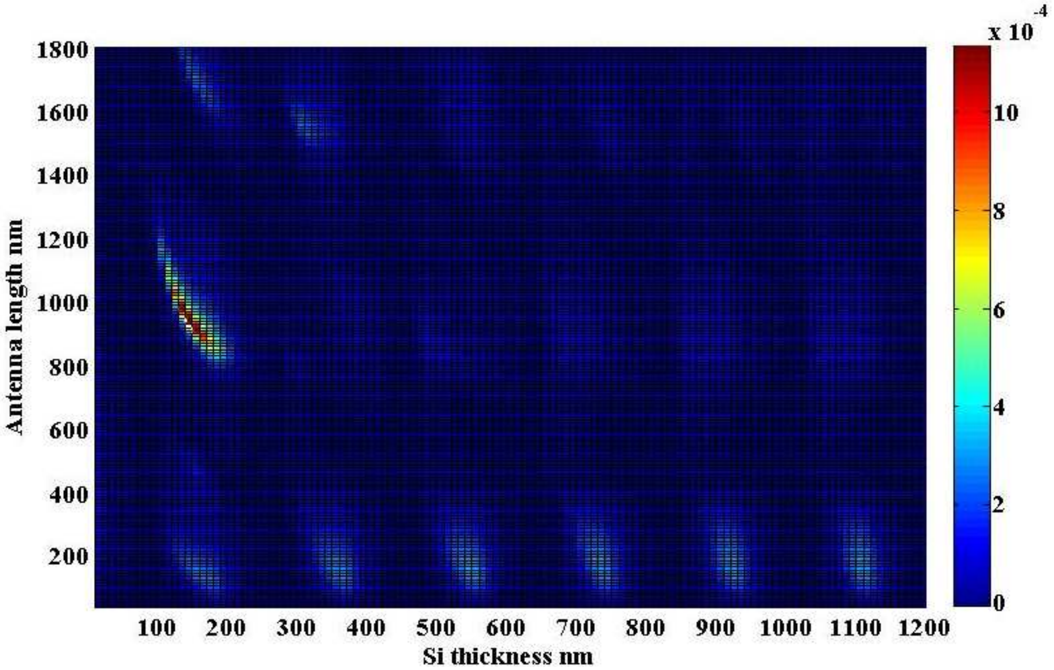

Figure 5.10: *The 2D parametric sweep of antenna thickness 40 nm repeated with finer sampling of Al and Si dimensions.*

varied between 10-1200 nm with a sampling of 10 nm for each parameter. The fig. 5.10 shows even finer periodic features for both antenna length and Si thickness. Absorption is maximum in the region encompassing antenna length 900-950 nm and Si thickness 140-150 nm.

To further optimise this geometry, another study carried out by varying only the SiO2 layer and choosing the above values for the other two parameters. The SiO2 layer is varied between 10 and 2000 nm with a step size of 10 nm. In each case the absorption is normalized to that of a single dot without any antenna. The simulation results are shown in fig. 5.11. The results seem to point to an oscillating behavior with respect to the SiO2 layer which points to the presence of an FP cavity. The first maxima occurs at an SiO_2 thickness of 250 nm. The period of oscillation observed to be around 450 nm. We now have an optimized 2D antenna geometry antenna length 900 nm Si thickness 150 nm and SiO2 thickness 250 nm. These parameters will be utilized in the remaining part of this study.

Due to the oscillatory behaviour of the absorption plot vis a vis the SOI stack, it might be interesting to see if incorporating a multilayer substrate composed of cascaded Si/Ox

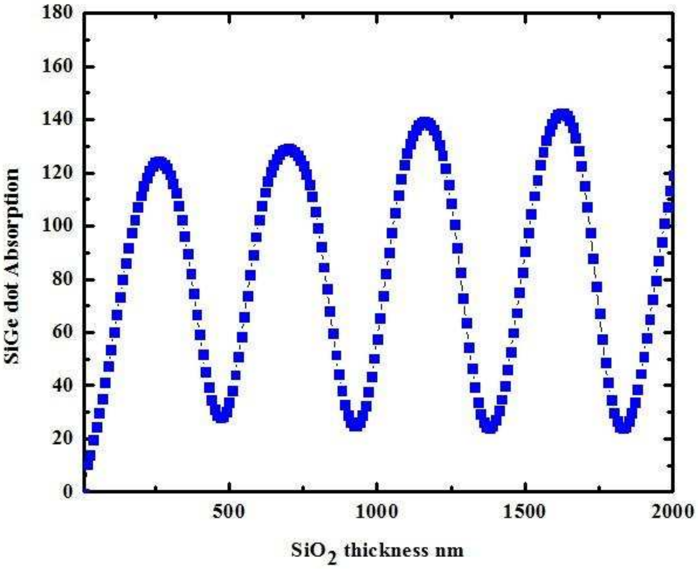

Figure 5.11: *The Normalised optical absorption as a function of SiO2 thickness. The absorption pattern appears to follow an oscillatory behaviour which might point to cavity effects due to oxide layer*

No. Si/SiO2 interf.	Absorption enhancement (BEM)
1.	120
2.	151
3.	56.6
4.	23.3

Table 5.1: Asborption enhancement as function of multistack layers of substrate.

layers, could improve the absorption. As such by using the above optimized paramters of antenna structure($Si = 150$ nm and $SiO_2 = 250$ nm), the calculation is repeated for different layers of Si/SiO_2interfaces as shown in fig. 5.12. These results are shown in table 5.1. The absorption increases for 2 periods of Si/SiO_2 and then starts to reduce. This absorption is found to be 1.19e-3 nW which is a little more than that of absorption of a single layer SOI stack.

5.4.2 FDTD

The above BEM calculation has been performed for a 2D geometry. In order to design an optimal geometry however, it is also necessary to evaluate the corresponding values of antenna parameters for a 3D structure. Doing so will also entail a deeper understanding

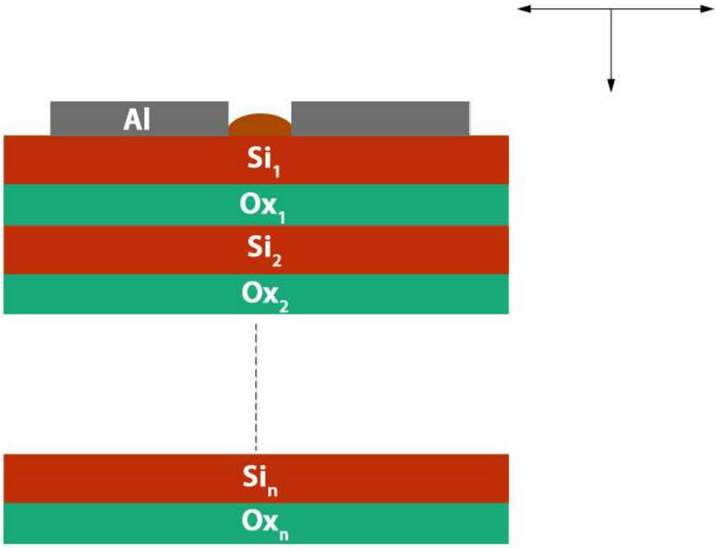

Figure 5.12: *The 2D design may be improved upon by incorporating a cascaded layer in the substrate consisting of alternating* Si/SiO_2 *layers.*

of the factors affecting the antenna resonance conditions. To do that fully vectorial 3D FDTD simulations using the Lumerical package are performed utilizing the 2D values obtained by the above optimised geometry from BEM. As such, all the parameters of the structure ie. thickness and length of Al, thickness of Si and SiO_2 which lie in the xz plane are derived from the BEM results. Since the Al is contacted on the dot, a finer mesh for the SiGe dot and its immediate surroundings is chosen at 0.5 nm. A TM polarised plane wave with the H field polarised in the y direction is selected to be incident normally on the structure. To calculate the dot absorption, a 3D field monitor is placed to match the dimensions of the SiGe dot and another index monitor is placed ovelapping the former. Field monitors are also placed in various locations to extract and study the field maps. The total power absorbed[165, 166] by the dot is given as :

$$P_{abs} = \frac{\omega}{2} Im(\epsilon)|E|^2 \tag{5.15}$$

Planar design

At first the planar rectangular geometry(fig. 5.13) of finite width is considered since this would closely aprroximate the BEM study where the antenna possesses infinite width.

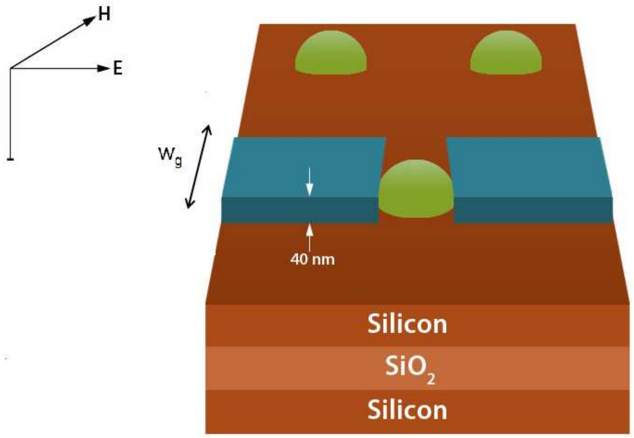

Figure 5.13: *3D planar design used for the FDTD study.*

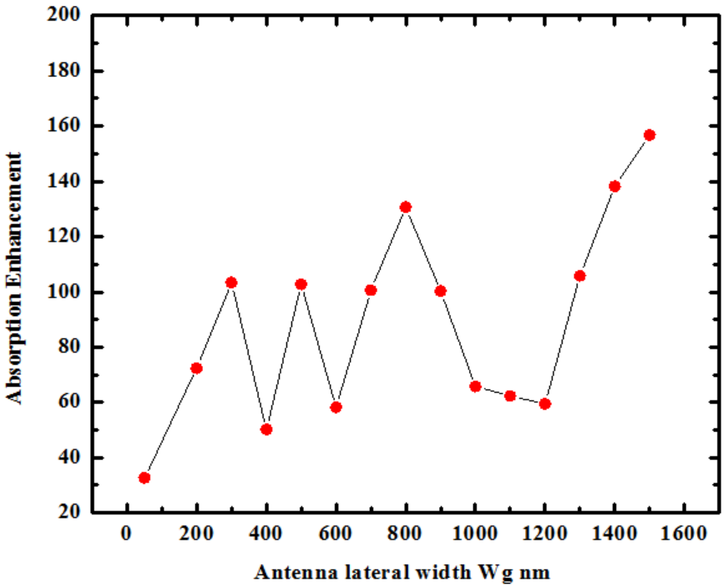

Figure 5.14: *Normalised antenna absorption as function of antenna width W_g.*

Next, the SiGe absorption is calculated as a function of the width W_g of the Al arms. The results of this study are plotted in fig. 5.14. In each case the antenna assisted dot absorption is normalised to that of absorption by a single dot without any antenna in the vicinity. Maximum absorption enhancement is observed for a width of 1500 nm with an enhancement factor of 150 times.

Bow-tie design

It might be interesting to see if incorporating a bow tie type geometry can further improve the optical absorption. Bow-tie antennas are considered to have higher field enhancement in the gap compared with two-wire antennas because of larger lightning-rod effect at the apex[168–172]. A schematic of the 3D geometry is shown in fig. 5.15. The tip width is fixed at 50 nm which is same as the gap distance between the two arms. A series of simulations are performed, wherein each case only the bow tie flare angle theta is varied between 0 and 120 in steps of 5 deg each. These simulations are done for both a single and two layer SOI stacks.

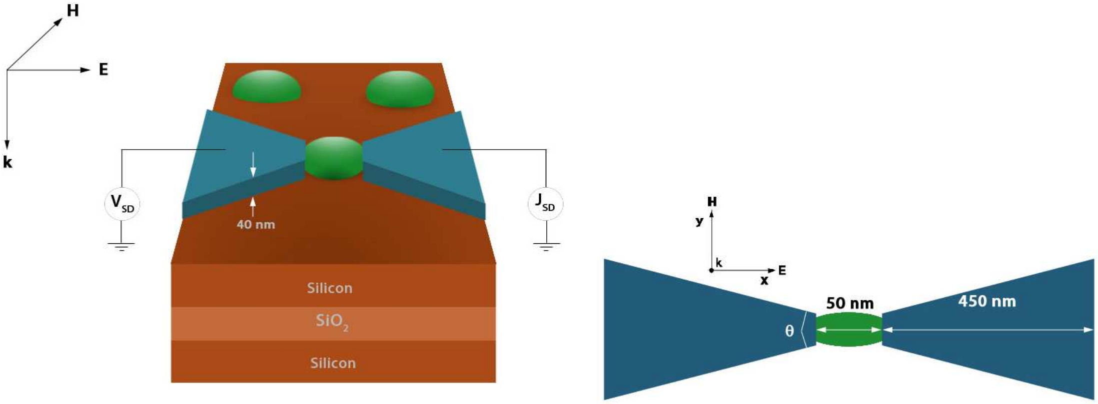

(a) *3D geometry* (b) *2D cross section*

Figure 5.15: *FDTD simulation layout. The depicted applied bias is for illustrational purpose only.*

5.5 Results and discussion

The results show a maximum absorption enhancement of over 500 times for a bow tie geometry with a tip angle 60 deg with a single layer SOI stack. The corresponding

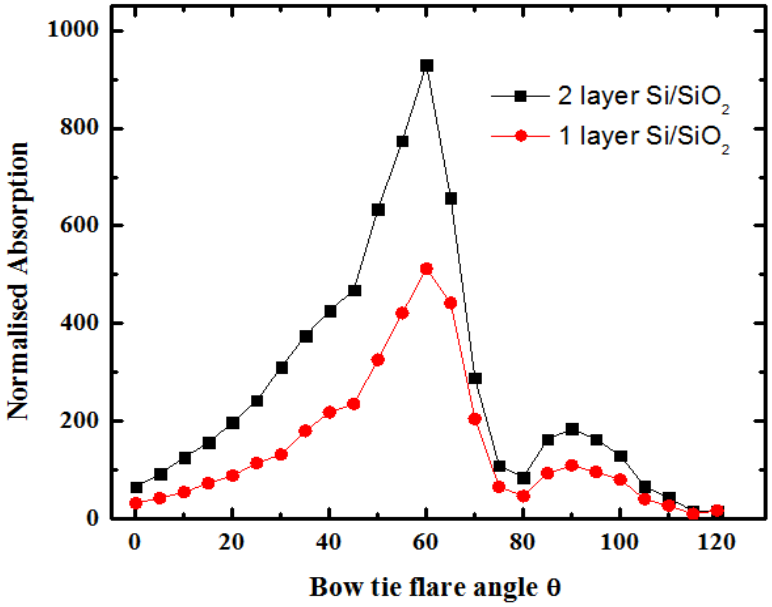

Figure 5.16: *Ge absorption as a function of bow tie angle θ for single and two layer SOI stacks.*

enhancement for a 2 layer SOI stack is 930 times. The different field maps extracted from field monitors are presented in the following fig. 5.17 and 5.18 which show the E intensity field profile of an SiGe dot on a standard SOI stack without any antenna surrounding it and that of a dot surrounded by a bow tie antenna with a 60° tip on a two layer optimized SOI stack, corresponding to maximum absorption in two separate cross sectional views. A rough comparison of the field pattern does indeed show a strong field enhancement in the antenna feed gap when compared to the case without antennas when no plasmons are present. An overlook of the field maps shown in fig. B.2(Appendix-B) shows a TM signature of the field pattern which in turn suggests the existence of guided surface waves at the Al/Si interface that are responsible for the resonant field enhancement at the feed gap. These surface waves that are coupled from the incident light are strongly dependent on parameters such as antenna geometry, dielectric composition as well as polarization as well as excitation wavelength. Furthermore a closer look at fig. 5.17(b) show bumps in the field patterns which could be a result of higher order multipolar resonances[173, 174]. To analyse in detail the effect that the substrate has on this resonance, a further simulation((fig. 5.19) is carried out by retaining the structural geometry of optimized bowtie antenna geometry but tuning the Si substrate thickness corresponding to low absorption as obtained from the BEM

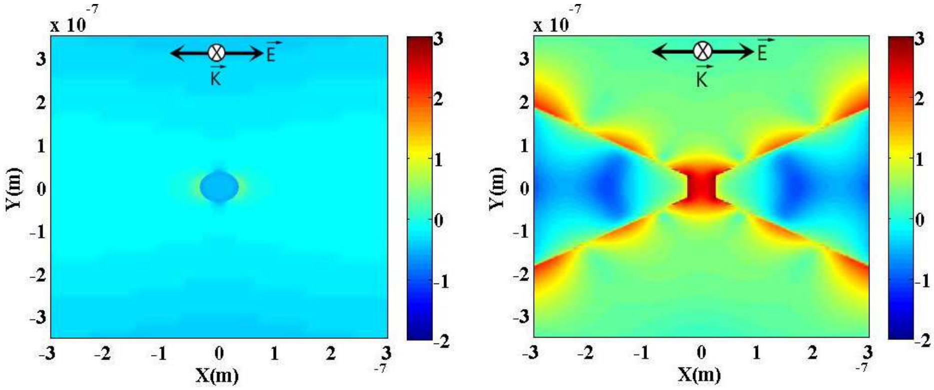

(a) *Without antenna* (b) *With antenna*

Figure 5.17: *The E field intensity (log) perpendicular to plane of incidence(xy) from a monitor placed in the antenna.*

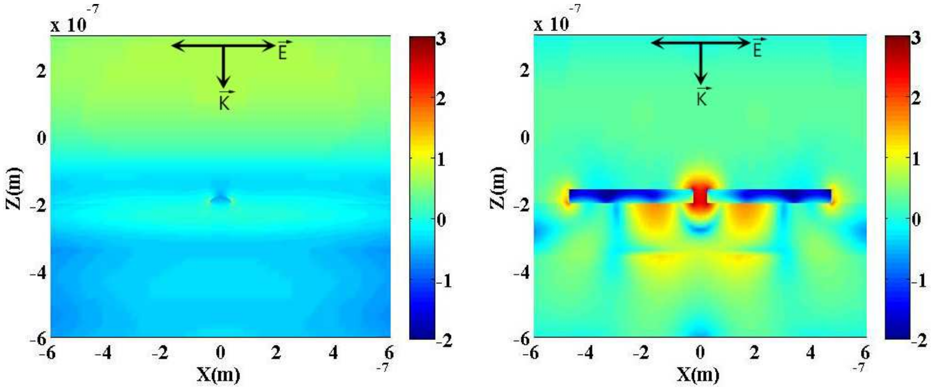

(a) *Without antenna* (b) *With antenna*

Figure 5.18: *The E field intensity (log) along the antenna axis(xz).*

plot. The field patterns in fig. 5.19(b) shows that there is some residual field in the unoptimized substrate region. For the optimized substrate however, no such field is observed. This feature could be explained by the existence of guided photonic modes in the unoptimized substrate stack to which the incident EM wave is coupled. The optimized substrate however allows only the presence of plasmon and leaky modes. Near field engineering of substrate dimensions is therefore critical to take advantage of resonant antenna properties. Fig. B.3(Appendix-B) shows the E field intensity profiles at different cascaded substrate layers of the opimized antenna. There seems to be more near field in the feed gap for the 2 layer antenna than for other cascaded SOI stacks. This as well as the results of table 5.2 are in good agreement with BEM results(table 5.1) depicted in the previous section.

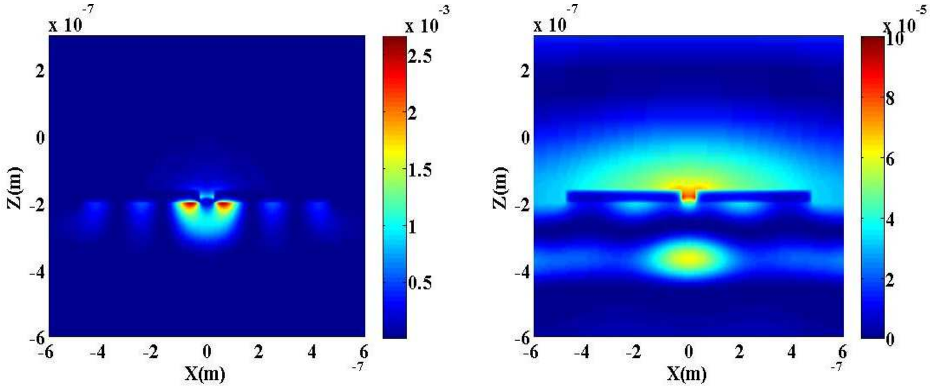

(a) (b)

Figure 5.19: *Magnetic field intensity (linear) in the case of resonant antenna (a) with and (b) without optimized SOI substrate. In the case of latter, some residual field in the substrate region is observed.*

No. of Si/Ox interf	Absorption enhancement (FDTD)	
	bow tie 0 deg.	bow tie 60 deg.
1	32.71	512
2	66	930
3	59.76	691
4	16	227

Table 5.2: FDTD calculation of normalised dot absorption for different substrate stacks at different bow flare angles.

For these calculations I have investigated the case of a single polarization angle which is maximum along the antenna dipole axis resembling the calculations performed in BEM. It might also be interesting to study the effect of this angle on the antenna near field properties at different bow flare angles. Also likewise, it would be interesting to see if incroporating certain cross-resonant structures, leads to further field enhancement in the antenna feed gap region. It must be pointed out that a gap dependent study has been excluded from this work keeping in mind the goal of designing a device based on current fabrication limitations. Such a study however would have probably yeilded more physical insight into the various factors affecting plasmon resonances, and shall now be left for future works.

5.6 Conclusion

This chapter was largely focussed on the optical modelling of an antenna based photodetector using the BEM and FDTD techniques in the near infrared region of optical communication. At first the BEM technique was used to investigate the dependence of optical absorption of an SiGe quantum dot with an Al layer in the vicinity as a function of different antenna parameters. For an optimal 2D design, comprising both the Al and SOI layers, the total absorption enhancement is found to be 150 times. A further improvement in 3D design is observed while performing FDTD simulations on a bow-tie structure.

The results suggest that through proper tuning of both antenna geometry and substrate dimensions, a higher radiative coupling can be achieved in the antenna feed gap region. For the final optimized structure, an absorption enhancement of over 900 times is achieved by the SiGe dot photodetector. The observed field maps seem to be in confirmation with the calculated data. By combining the faster BEM technique with FDTD, we have been able to derive an optimal 3D antenna geometry with significantly reduced computation time and memory.

Such design could be readily developed using existing fabrication techniques to see if the observed field enhancement transpires into improved photodetector responsivity

Conclusions and Perspectives

The interest of using plasmons for CMOS plasmonic active devices has been investigated throughout this work.

The third chapter is dedicated to a rigorous numerical investigation of a metal oxide semiconductor plasmonic waveguide. Here emphasis was mostly laid on the modal and propagation characteristics of this structure. The plasmon propagation characteristics of a MOS waveguide has been analysed in detail numerically. Both modal properties and transmission results from FDTD simulations suggested a largely single mode behavior at short waveguide widths with some leaky contributions. At larger widths, self-imaging due to MMI effect is observed. There is an enormous potential to integrate plasmonic elements into photonic circuits. The MMI effect evidenced here in a MOS waveguide can be exploited to develop passive elements like splitters, routers, multiplexers just like photonic guides albeit with much lesser dimensions. Throuhout those developments, it should be paid attention to possible leaky modes non negligible contributions, such as the one we observed and discussed here in the case of a canonical butt coupler.

Chapter four dealt with optimising a metal slot waveguide based design for an electroabsorption modulator based on the Franz Keldysh effect in Ge, while preserving a CMOS compatible fabrication scheme. Simulations were performed using the finite element method to investigate the modal characteristics of this design. The use of metal slot guides for designing plasmon modulators show that there are definite technological limitations. Here the main issue to be addressed is that of plasmon propagation losses. A fine balance is required when it comes to achieving higher mode confinement and reducing propagation losses. Another issue here is the diffusion of metals. While low index barriers can provide some cushion in this regard, they may also act as low loss channels for plasmons, which may affect the overall device extinction ratio. A very compact design is reached, at the cost of some compromise on the losses of the device, opening some perspective for the reduction of energy consumption modulators for integrated photonic circuits. Alternatively other designs and or low loss contact materials may also be explored.

The fifth and final chapter is focussed on conceiving a novel nanoantenna design for a Ge dot photodetector. Extensive use was made of both the BEM and FDTD techniques. While BEM was used to optimise the 2D design, FDTD was used for the 3D. The Ge dot antenna optimisation has by and large demonstrated the efficiency of using the boundary element method in near field engineering of nanoplasmonic antennas for near infra-red photodetection. So far the boundary element method has been mostly applied to nanomatellic structures of arbitrary shapes in homogenous media in the visible spectrum. Here we have extended this formulation to simulate of nanoantennas on an SOI substrate. Moreover the fast and efficient use of the boundary element method together with an optimization algorithm, can greatly reduce the computational time required for simulations. The 2D BEM results seem to be in good agreement with 3D FDTD results. The BEM technique may in future be adapted to analyse more complex geometries in both visible and infra-red regimes. On the scientific point of view, an issue with nanoantennas so far not addressed in previous works has been the effect of substrates on its near field properties. The results from BEM and FDTD show that through a proper choice of geometry as well as substrate dimensions, an almost 3 order absorption enhancement was noticed for the optimised design. That result stems from the radiative engineering of the Ge dot environment, obviously including the plasmonic antenna, but also the SOI substrate structure. Calculated geometries could be easily implanted, so as to check whether this enhancement may transpose into increased detector responsivity.

Appendix A-Overlap Analysis

Any field can be decomposed into the corresponding output fields as a basis of orthogonal modes. Hence expressing the electric and magnetic fields E_{out} and H_{out} as:

$$E_{out} = \sum_i p_i E_i \tag{5.16}$$

$$H_{out} = \sum_i q_i H_i \tag{5.17}$$

Applying the continuity of the tangential components accross the interface and assuming the reflected fields are small we have:

$$E^{\perp}_{inp} = E^{\perp}_{out} \tag{5.18}$$

$$H^{\perp}_{inp} = H^{\perp}_{out} \tag{5.19}$$

The input fields may now be expresed as:

$$E_{inp} = \sum_i p_i E_i \tag{5.20}$$

$$H_{inp} = \sum_i q_i H_i \tag{5.21}$$

Multiplying the first of the above by H^*:

$$E_{inp} \times H^*_i = \sum_i p_i E_i \times H^*_i \tag{5.22}$$

$$p_i = \frac{\int E_{inp} \times H^*_i . dS}{\int E_i \times H^*_i dS} \tag{5.23}$$

Similarly

$$q^*_i = \frac{\int E_i \times H^*_{inp} . dS}{\int E_i \times H^*_i . dS} \tag{5.24}$$

Now the total power in the input and output fields may be expressed as:

$$P_{inp} = \frac{1}{2}Re\left\{\int E_{inp} \times H_{inp}^{*}\right\}.dS \tag{5.25}$$

$$P_{out} = \frac{1}{2}Re\left\{\int \left(\sum_{i} p_i E_i\right) \times \left(\sum_{i} q_i H_i\right)^{*}\right\}.dS \tag{5.26}$$

Substituting the terms p_i and q_i

$$P_{out} = \frac{1}{2}Re\left\{\frac{\left(\int E_{inp} \times H_{i}^{*}.dS\right)\left(\int E_{i} \times H_{inp}^{*}.dS\right)\left(\int E_{i} \times H_{i}^{*}.dS\right)}{\left(\int E_{i} \times H_{i}^{*}.dS\right)\left(\int E_{i} \times H_{i}^{*}.dS\right)}\right\} \tag{5.27}$$

$$= \frac{1}{2}Re\left\{\frac{\left(\int E_{inp} \times H_{i}^{*}.dS\right)\left(\int E_{i} \times H_{inp}^{*}.dS\right)}{\left(\int E_{i} \times H_{i}^{*}.dS\right)}\right\} \tag{5.28}$$

The overlap integral is then the ratio of the total power of the i^{th} mode propagating in the output guide to that of the power in the input guide:

$$\frac{P_{out}}{P_{inp}} = Re\left\{\frac{\left(\int E_{inp} \times H_{i}^{*}.dS\right)\left(\int E_{i} \times H_{inp}^{*}.dS\right)}{\left(\int E_{i} \times H_{i}^{*}.dS\right)}\right\}\frac{1}{Re\left\{\left(\int E_{inp} \times H_{inp}^{*}.dS\right)\right\}} \tag{5.29}$$

Appendix B-FDTD Field Maps of Optical Antenna

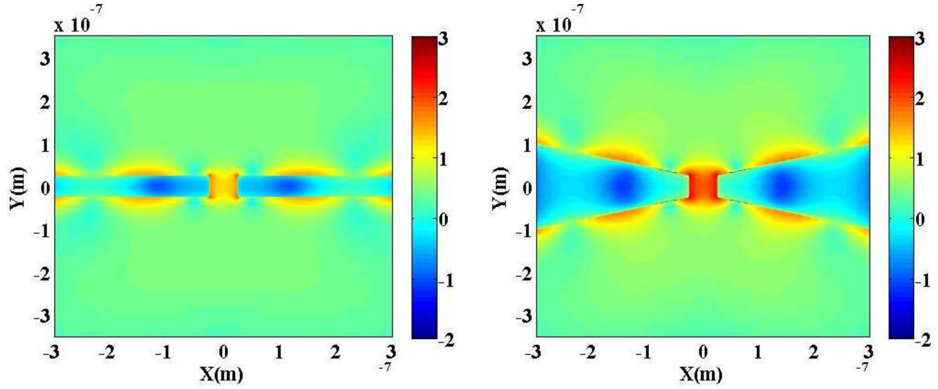

(a) **0°** (b) **30°**

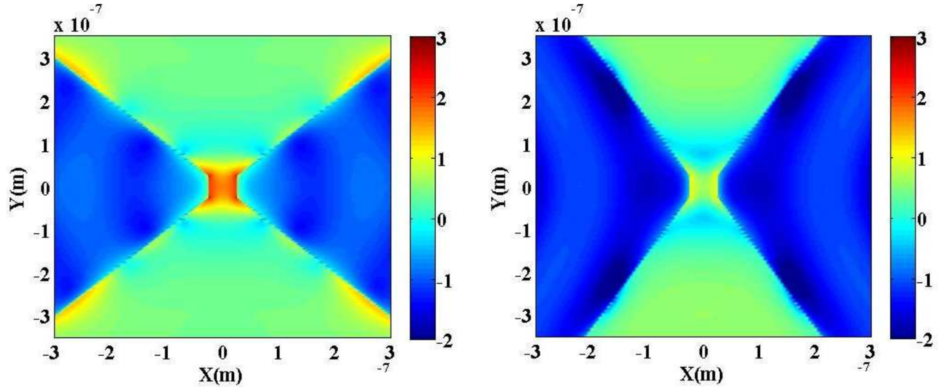

(c) **90°** (d) **120°**

Figure B.1 *The E field intensity profile in log scale for different bow flare angles for the for antennas with optimised length and 2 layer substrate. These field profiles are in good agreement to the data plotted in figure 5.16*

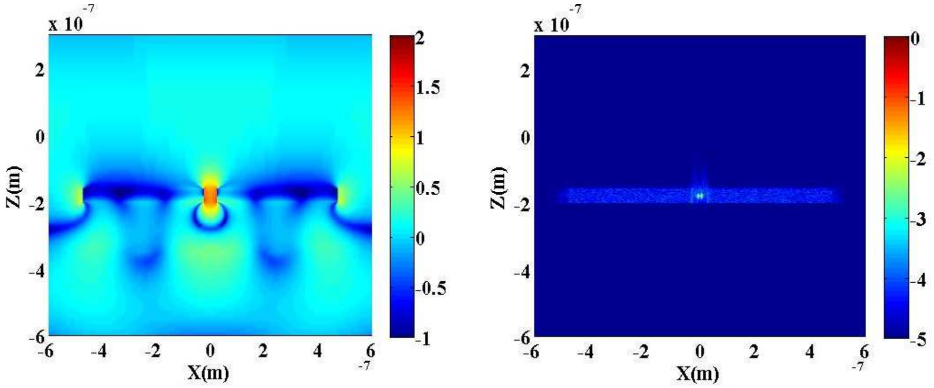

(e) **Ex**

(f) **Ey**

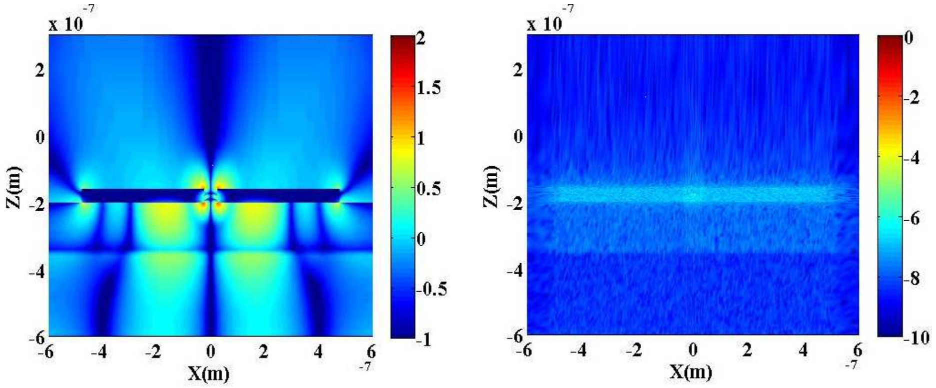

(g) **Ez**

(h) **Hx**

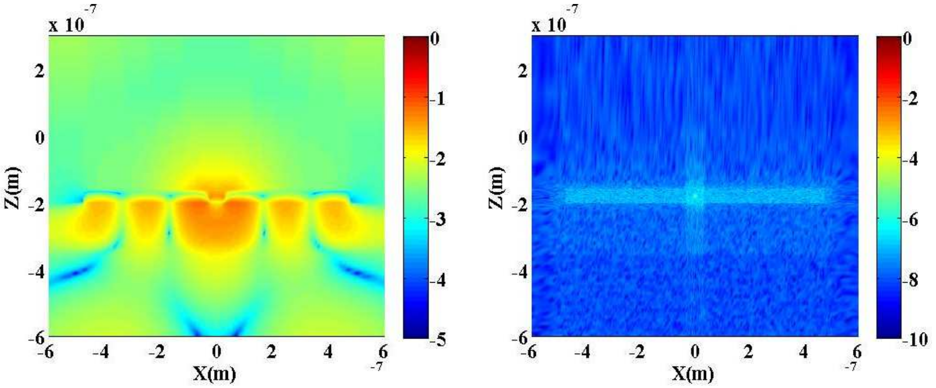

(i) **Hy**

(j) **Hz**

Figure B.2 *The different E and H field magnitudes for the optimised antenna in absolute log scale. The dominant components are Ex, Ez and Hy implying a resonant plasmon excitation at Al/Si interface.*

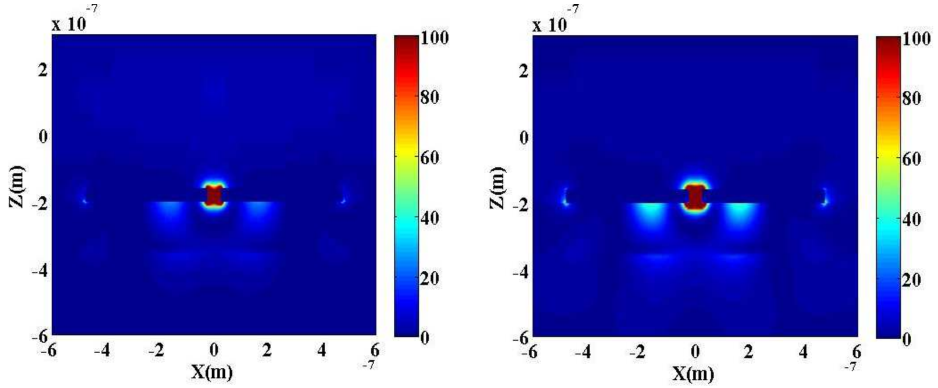

(k) **1 layer** (l) **2 layer**

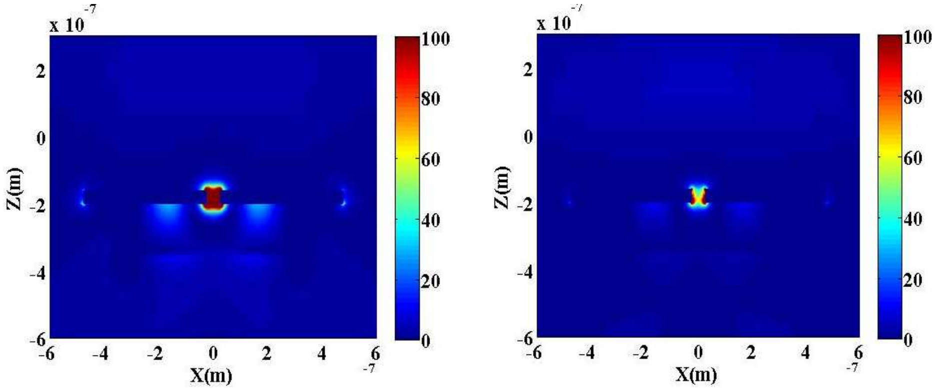

(m) **3 layer** (n) **4 layer**

Figure B.3 *The E field intensity profile in linear scale extracted from a monitor cutting across the antenna axis along the xz plane for the optimised bow tie design for cascaded layers of Si/Ox interfaces. There appears to be a clear correspondance with the results of table 5.2*

Bibliography

[1] Eric C Le Ru, Pablo G. Etchegoin, *Principles of Surface-Enhanced Raman Spectroscopy and Related Plasmonic Effects*, Elsevier Amsterdam (2009)

[2] Haibo Li, Shuping Xu, Yu Liu, Yuejiao Gu, Weiqing Xu, *Directional emission of surface-enhanced Raman scattering based on a planar-film plasmonic antenna*, Thin Solid Films Vol. 520 Issue 18 pp 6001-6 (2012)

[3] N I Cade, T Ritman-Meer, K A Kwakwa, D Richards, *The plasmonic engineering of metal nanoparticles for enhanced fluorescence and Raman scattering*, Nanotechnology 20 pp 285201-5 (2009)

[4] Tam F, Goodrich, G P, Johnson B R, Halas N J, *Plasmonic enhancement of molecular fluorescence*, Nano Lett. Vol. 7 Issue 2 pp 496-501 (2007)

[5] Bakker R M et al, *Enhanced localized fluorescence in plasmonic nanoantennae*, Appl. Phys. Lett. Vol. 92 Issue 4 pp 043101-1-3 (2008)

[6] Gerard D., J. Wenger, N Bonod, E. Popov, H. Rigneault, F. Mahdavi, S. Blair, J. Dintinger, T W. Ebbesen , *Nanoaperture-enhanced fluorescence: Towards higher detection rates with plasmonic metals*, Phys. Rev. B Vol. 77 Issue 4 pp 045413-20 (2008)

[7] Taminiau T H, Stefani F D, Segerink F B, van Hulst N, *Optical Antennas Direct Single Molecule Emission*, Nphoton Vol. 2 pp 234-237 (2008)

[8] Reuben M Bakker, Vladimir P Drachev, Zhengtong Liu, Hsiao-Kuan Yuan1, Rasmus H Pedersen, Alexandra Boltasseva, Jiji Chen, Joseph Irudayaraj, Alexander V Kildishev Vladimir M Shalaev1, *Nanoantenna array-induced fluorescence enhancement and reduced lifetimes*, IOP New J. Phys. Vol. 10 pp 1-16 (2008)

[9] A. Kinkhabwala, Z. Yu, S. Fan, Y. Avlasevich, K. Mllen, W. E. Moerner, *Large Single-Molecule Fluorescence Enhancements Produced by a Bowtie Nanoantenna*, Nphoton Vol. 3, 654-657 (2009)

[10] Ferry, V. E. Sweatlock, L. A. Pacifici, D. Atwater, H, *Plasmonic Nanostructure Design for Efficient Light Coupling into Solar Cells*, Nano Lett., Vol. 8 Issue 12 pp 43914397 (2008)

[11] Harry A. Atwater, Albert Polman, *Plasmonics for improved photovoltaic devices*, Nature Materials Vol. 9 Issue 3 pp 205213 (2010)

[12] Leonid Khriachtchev, *Silicon Nanophotonics: Basic Principles Present Status and Perspectives* World Scientific Publishing Co. Pte. Ltd (2009)

[13] L. C. Kimerling *et al* Invited *Electronic-photonic integrated circuits on the CMOS platform*, Proc. of SPIE Vol. 6125 pp 612502-1-10 (2006)

[14] JM. Fedeli, J.Marti, D.Van Thourhout, G.Reed, T.White, *Silicon Photonics Developments in Europe*, Proc. of SPIE Vol. 7220 pp 72200A-1-12 (2009)

[15] J. Warga, R. Li, S.N. Basu, L. Dal Negro, *Erbium-doped silicon nanocrystals in silicon/silicon nitride superlattice structures: Light emission and energy transfer*, Physica E Vol. 41 No. 6 pp 10401043 (2009)

[16] Jifeng Liu, Xiaochen Sun, Rodolfo Camacho-Aguilera, Lionel C. Kimerling, Jurgen Michel, *Ge-on-Si laser operating at room temperature*, Opt. Lett. Vol. 35 Issue 5 pp 679-681 (2010)

[17] E. Ozbay, Plasmonics: Merging photonics and electronics at nanoscale dimensions, Science, Vol. 311, No. 5758 pp 189-193 (2006)

[18] Wassel H.M.G., Daoxin Dai, Tiwari M., Valamehr J.K., Theogarajan L., Dionne J., Chong F.T., Sherwood, T., *Opportunities and Challenges of using Plasmonic Components in Nanophotonic Architectures*, IEEE Journal: Emerging and Selected Topics in Circuits and Systems Vol. 2 Issue 2 pp 154-168 (2012)

[19] Shiyang Zhu, Guo-Qiang Lo, Dim-Lee Kwong, *CMOS-Compatible Silicon Nanoplasmonics for On-Chip Integration*, World Academy of Science, Engineering and Technology 69 pp 486-492 (2012)

[20] J.A. Conway, S. Sahni, T. Szkopek, *Plasmonic interconnects versus conventional interconnects: a comparison of latency, crosstalk and energy costs*, Opt. Exp. Vol. 15, Issue 8 pp 4474-4484 (2007)

[21] S A Maier, *Plasmonics, Fundamentals and Applications*, Springer (2007)

[22] Andreas Otto., *Excitation of nonradiative surface plasma waves in silver by the method of frustrated total reflection*, Z. Phys. Vol. 216 Issue 4 pp 398-410 (1968)

[23] E. Kretschmann and H. Raether, *Radiative decay of nonradiative surface p1asmons excited by light*, Z. Naturforsch. A Vol. 23 2135 (1968)

[24] Heinz Rather, *Surface Plasmons on Smooth and Rough Surfaces and on Gratings*, Springer-Verlag Berlin (1988)

[25] J. Burke, G. Stegeman, T. Tamir, *Surface-polariton-like waves guided by thin, lossy metal films*, Phys. Rev. B Vol. 33 Issue 8 pp 5186-5201 (1986)

[26] Themistos C., Rahman B.M.A., Rajarajan M., Rakocevic, V., Grattan K.T.V., *Finite Element Solutions of Surface-Plasmon Modes in Metal-Clad Dielectric Waveguides at THz Frequency*, Journal of Lighwave Tech. Vol. 24 Issue 12 pp 5111-5118 (2006)

[27] Min Yan, Min Qiu, *Analysis of Surface Plasmon Polariton Using Anisotropic Finite Elements*, Phot. Tech. Lett. Vol. 19 Issue 22 pp 1804-1806 (2007)

[28] A. Krishnan, L. Grave de Peralta, M. Holtz, A. A. Bernuss, *Finite Element Analysis of Lossless Propagation in Surface Plasmon Polariton Waveguides With-Nanoscale Spot-Sizes*, Journal of Lightwave Tech. Vol. 27 Issue 9 pp 1114-1121 (2009)

[29] Sven Burger, Lin Zschiedrich, Jan Pomplun, Frank Schmidt, *Finite element method for accurate 3D simulation of plasmonic waveguides*, Proc. SPIE Vol. 7604 (2010)

[30] John Leonidas Volakis, Arindam Chatterjee, and L. C. Kempel, *Finite element method for electromagnetics: antennas, microwave circuits, and scattering applications*, Wiley-IEEE, (1998)

[31] Xinchao Lu, Carsten Rockstuhl, and Weili Zhang, *Far-infrared properties of hybrid plasmonic geometries*, J. Opt. Soc. Am. A Vol. 29 Issue 4 pp 644-648 (2012)

[32] Miguel Navarro-Cia, Stefan A. Maier, *Broad-Band Near-Infrared Plasmonic Nanoantennas for Higher Harmonic Generation* ACS Nano Lett. Vol. 6 No. 4 pp 35373544 (2012)

[33] Olivier J. F. Martin, Christian Girard, Alain Dereux, *Generalized Field Propagator for Electromagnetic Scattering and Light Connement*, Phys. Rev. Lett. Vol. 74, No. 4 526-529 (1995)

[34] Michael Paulus, Oliver J. F. Martin, *Light propagation and scattering in stratified media: a Greens tensor approach*, J. Opt. Soc. Am. A Vol. 18 Issue 4 pp 854-861 (2001)

[35] Esteban Moreno Daniel Erni, Christian Hafner, Ru diger Vahldieck, *Multiple multipole method with automatic multipole setting applied to the simulation of surface plasmons in metallic nanostructures*, J. Opt. Soc. Am. A Vol. 19, Issue 1 pp 101-111 (2002)

[36] P. Liu *et al*, *Polarization properties of single metallic nano-spheroid using 3-D boundary element method*, Optik Vol. 123 Issue 11 pp 9961000 (2012)

[37] S. Mazzucco, O. Stephan, C. Colliex, I. Pastoriza-Santos, L.M. Liz-Marzan, J. Garcia de Abajo, and M. Kociak, *Spatially resolved measurements of plasmonic eigenstates in complex-shaped, asymmetric nanoparticles: gold nanostars*, Eur. Phys. J. Appl. Phys. Vol. 54 Issue 3 pp 33512-p1-p9 (2011)

[38] Ulrich Hohenester, Andreas Trgler, *MNPBEM A Matlab toolbox for the simulation of plasmonic nanoparticles* Compt. Phys. Comm. Vol. 183 Issue 2 (370381) 2012

[39] A A Maradudin T. Michael, A R McGurn, E R Mendez *Enhanced backscattering of light from a random grating*, Ann. Phys. (NY) Vol. 203 Issue 2 pp 255-307 (1990)

[40] Vincenzo Giannini, Jose A Sanchez Gil *Calculations of Light scatterin from Isolated and interacting Metallic nanowires of arbitrary cross-sections by means of Green's theorem surface integral equation in parametric form*, J. Opt. Soc. Am A Vol 24 No. 9 pp 2822-2830 (2007)

[41] J A Sanchez Gil, J V Garcia-Ramos E R Mendez *Near Field Electromagnetic wave scattering from random self-affine fractal metal surfaces: Spectral dependence of local field enhancement and their statistics in connection with surface enhanced Raman scattering*, Phys. Rev. B Vol. 62 Issue 15 pp 1051510525 (2000)

[42] K Yee, *Numerical solution of initial boundary-value problems involving Maxwells equations in isotropic media*, IEEE Trans. Ant. Prop., Vol. 14 Issue 3 pp. 302307 (1966)

[43] J.P. Berenger, *Perfectly matched layer for the FDTD solution of wavestructure interaction problems*, IEEE Trans. Ant. Prop., Vol. 44, Issue 1, pp. 110117, (1996)

[44] Luebbers R J, Hunsberge F, Kunz K S, *A frequency-dependent finite- difference time-domain formulation for transient propagation in plasma* IEEE Trans. Ant. Prop., Vol. 39 Issue 1 pp 2934, (1991)

[45] Dennis M. Sullivan, *Electromagnetic simulation using the FDTD Method*, IEEE press (2000)

[46] Allen Taflove *Computational electrodynamics: The finite-difference time-domain method*, Artech House (Boston) (1995)

[47] F. Ouyang and M. Isaacson, Ultramicroscopy, 31, 245, (1989)

[48] M. G. Arajo, J. M. Taboada, J. Rivero, D. M. Sols, F. Obelleiro, *Solution of large-scale plasmonic problems with the multilevel fast multipole algorithm*, Opt. Lett. Vol. 37, Issue 3, pp 416-418 (2012)

[49] A V Krasavin, Anatoly V. Zyats, *Silicon based plasmonic waveguides*, Opt. Exp. Vol. 18, Issue 11 pp 11791-11799 (2010)

[50] Tobias Holmgaard, Sergey I. Bozhevolnyi, Laurent Markey, Alain Dereux, *Dielectric-loaded surface plasmon-polariton waveguides at telecommunication wavelengths: Excitation and characterization*, Appl. Phys. Lett. Vol. 92, Issue 1 pp 011124-1-3 (2008)

[51] Tobias Holmgaard and Sergey I. Bozhevolnyi, *Theoretical analysis of dielectric-loaded surface plasmon-polariton waveguides*, Phys. Rev. B Vol. 75 Issue 24 pp 245405-1-12 (2007)

[52] Michael Hochberg, Tom Baehr-Jones, Chris Walker, Axel Scherer, *Integrated plasmon and dielectric waveguides*, Opt. Exp. Vol. 12, Issue 22 pp 5481-5486 (2004)

[53] Tobias Holmgaard, Sergey I. Bozhevolnyi, Laurent Markey, Alain Dereux, Alexey V. Krasavin, Pdraig Bolger, and Anatoly V. Zayats, *Efficient excitation of dielectric-loaded surface plasmon-polariton waveguide modes at telecommunication wavelengths*, Phys. Rev. B 78, pp 165431-1-8 (2008)

[54] S. Sederberg, V. Van, and A. Y. Elezzabi, *Monolithic integration of plasmonic waveguides into a complimentary metal oxide semiconductor and photonic compatible platform*, Appl. Phys. Lett. Vol. 96, Issue 12 pp 121101-1-3 (2010)

[55] Ilya V. Shadrivov,a Sergey I. Bozhevolnyi,b and Yuri S. Kivshara ,*Backward and forward modes guided by metal-dielectric-metal plasmonic waveguides*, Journal of Nanophotonics, Vol. 4, 043509 (2010)

[56] Michael J. Preiner, Ken T. Shimizu, Justin S. White, and Nicholas A. Melosh *Efficient optical coupling into metal-insulator-metal plasmon modes with subwavelength diffraction gratings*, Appl. Phys. Lett. Vol. 92 Issue 11 pp 113109-1-3 (2008)

[57] Ning-Ning Feng, Luca Dal Negro *Plasmon mode transformation in modulated-index metal-dielectric slot waveguides*, Opt. Lett. Vol. 32, Issue 21 pp 3086-3088 (2007)

[58] Georgios Veronis, Shanhui Fan, *Modes of Subwavelength Plasmonic Slot Waveguides*, Journal of Lightwave Technology, Vol. 25, Issue 9, pp 2511-2521 (2007)

[59] Dany-Sebastien Ly-Gagnon, Sukru Ekin Kocabas, David A. B. Miller, *Characteristic Impedance Model for Plasmonic Metal Slot Waveguides*, IEEE Journal of Selected Topics in Quantum Electronics, Vol. 14 Issue 6, pp 1473-1478 (2008)

[60] Shiyang Zhu, T. Y. Liow, G. Q. Lo, D. L. Kwong, *Silicon-based horizontal nanoplasmonic slot waveguides for on-chip integration*, Opt. Exp. Vol. 19 Issue 9 pp 8888-8902 (2011)

[61] J. A. Dionne, L. A. Sweatlock, H. A. Atwater, A. Polman, *Plasmon slot waveguides: Towards chip-scale propagation with subwavelength-scale localization*, Phys. Rev. B 73 pp 035407-1-9 (2006)

[62] Min-Suk Kwon, *Metal-insulator-silicon-insulator-metal waveguides compatible with standard CMOS technology*, Opt. Exp. Vol. 19, Issue 9 pp 8379-8393 (2011)

[63] Aaron C. Hryciw, Young Chul Jun, Mark L. Brongersma, *Plasmon-enhanced emission from optically-doped MOS light sources*, Opt. Exp. Vol. 17, Issue 1 pp 185-192 (2009)

[64] Lucas B. Soldano and Erik C. M. Pennings, *Optical Multi-Mode Interference Devices Based on Self-Imaging : Principles and Applications*, Journal of Lightwave Technology Vol. 13 Issue 4 pp 615-627 (1995)

[65] Amir Hosseini, David Kwong, Che-Yun Lin, Beom Suk Lee, Ray T. Chen, *Output Formulation for Symmetrically Excited One-to-N Multimode Interference Coupler*, IEEE Journal of Selected Topics in Quantum Electronics, Vol. 16, Issue 1 pp 61-69 (2010)

[66] Kin Seng Chiang, Member, IEEE, Qing Liu, *Formulae for the Design of Polarization-Insensitive Multimode Interference Couplers*, IEEE Photonics Technology Letters Vol. 23 Issue 18 pp 1277-1279 (2011)

[67] Brian R. West and Seppo Honkanen, *MMI devices with weak guiding designed in three dimensions using a genetic algorithm*, Opt. Exp. Vol. 12, Issue 12 pp 2716-22 (2004)

[68] Snyder and Love, *Optical Waveguide Theory* (1983)

[69] Guanghui Yuan, Pei Wang, Yonghua Lu, Hai Ming *Multimode interference splitter based on dielectric-loaded surface plasmon polariton waveguides*, Opt. Exp. Vol. 17, Issue 15 pp 12594-12600 (2009)

[70] Yu-Ju Tsai, Aloyse Degiron, Nan M. Jokerst, and David R. Smith, *Plasmonic Multi-Mode Interference Couplers*, Opt. Exp. Vol. 17, Issue 20 pp 17471-17482 (2009)

[71] Andr G. Edelmann, Stefan F. Helfert, Jrgen Jahns, *Analysis of the self-imaging effect in plasmonic multimode waveguides*, Appl. Opt. Vol. 49, Issue 7 pp A1-A10 (2010)

[72] Andr G. Edelmann Stefan F. Helfert Jrgen Jahns, *Transmission characteristics in plasmonic multimode Waveguides*, Springer Opt. Quant. Electron Vol. 42 Issue 8 pp 531-540 (2011)

[73] Yao Kou and Xianfeng Chen, *Multimode interference demultiplexers and splitters in metal-insulator-metal waveguides*, Optics Exp. Vol. 19, No. 7 pp 6042-6047 (2011)

[74] Yi Song, Jing Wang, Min Yan and Min Qiu, *Efficient coupling between dielectric and hybrid plasmonic waveguides by multimode interference power splitter*, J. Opt. Vol. 13 No. 7 pp 075002 (2011)

[75] T. Nakamura, C. L. Xu, X. Li , W.-P. Huang, *A Spot-Size Transformer Based on Mode Interference*, IEEE Photonics Technology Letter, Vol. 10 Issue 3 pp 325-327 (1998)

[76] Guang Wei Yuan, Matthew D. Stephens, David S. Dandy, and Kevin L. Lear *Direct Imaging of Transient Interference in a Single-Mode Waveguide Using Near-Field Scanning Optical Microscopy*, IEEE Photonics Technology Letters Vol. 17 Issue 11 pp 2382-2384 (2005)

[77] Rongjin Yan, Guangwei Yuan, Matthew D. Stephens, Xinya He, Charles S. Henry *Evanescent field response to immunoassay layer thickness n planar waveguides*, Appl. Phys. Lett. Vol. 93, Issue 10 101110-1-3 (2008)

[78] M. R. Dennis, N. I. Zheludev, and F. J. G. de Abajo, *The plasmon Talbot effect*, Opt. Exp. Vol. 15 Issue 15 pp 96929700 (2007)

[79] H. F. Talbot, *Facts relating to optical science, No. IV*, Philos. Mag. Vol. 9 Issue 56 pp 401407 (1836)

[80] A. W. Lohmann and D. A. Silva, *An interferometer based on the talbot effect*, Opt. Commun. Vol. 2 Issue 9 pp 413415 (1971)

[81] Yoshiaki Nakano and Kazumi Murata, *Talbot interferometry for measuring the focal length of a lens*, Appl. Optics, Vol. 24, Issue 19, pp 3162-3166 (1985)

[82] J. Jahns, E. ElJoudi, D. Hagedorn, and S. Kinne, *Talbot interferometer as a time filter*, Optik (Jena) Vol. 112 Issue 7 pp 295298 (2001).

[83] Hyun Seok Lee, Chawki Awada, Salim Boutami, Fabrice Charra, Ludovic Douillard, Roch Espiau de Lamaestre *Loss mechanisms of surface plasmon polaritons propagating on a smooth polycrystalline Cu surface*, Opt. Exp. Vol. 20, Issue 8, pp 8974-8981 (2012)

[84] Alexandros Emboras, Adel Najar, Siddharth Nambiar, Philippe Grosse, Emmanuel Augendre, Charles Leroux, Barbara de Salvo, Roch Espiau de Lamaestre *MNOS stack for reliable, low optical loss, Cu based CMOS plasmonic devices*, Opt. Exp. Vol 20 Issue 13 pp 13612-13621 (2012)

[85] A. Emboras, R.Briggs, A. Najar, S. Nambiar, C. Delacour, Ph. Grosse, E. Augendre, J.M. Fedeli, B. de Salvo, H.A Atwater, R. Espiau de Lamaestre *Efficient coupler between silicon photonic and metal-insulator-silicon-metal plasmonic waveguides*, Appl. Phys. Lett. Vol. 101, Issue 25 251117-1-4 (2012)

[86] Isamu Kotaka, Koichi Wakita, Osamu Mitomi, Hiromitsu Asai, Yuichi Kawamura*High-speed InGaAlAdInAlAs Multiple Quantum Well Optical Modulators with Bandwidths in I Excess of 20 GHz at 1.55 μm*, IEEE Photonics Technology Lett. Vol. 1, Issue 5 pp 100-101 (1989)

[87] Chad Husko, Alfredo De Rossi, Sylvain Combri, Quynh V Tran, Fabrice Raineri, Chee Wei Wong *Ultrafast all-optical modulation in GaAs photonic crystal cavities*, Appl. Phys. Lett. Vol. 94 Issue 2 pp 021111-1-3 (2009)

[88] Petter Holmstrm *Electroabsorption Modulator Using Intersubband Transitions in GaNAlGaNAlN Step Quantum Wells*, IEEE Journal of Quantum Electronics Vol. 42, Issue 8 pp 810-819 (2006)

[89] S. Y. Hu, J. K, and L. A. Coldren *Resonant-cavity InGaAs/InAlGaAs/InP photodetector arrays for wavelength demultiplexing applications*, Appl. Phys. Lett. Vol. 70 Issue 18 pp 2347-2349 (1997)

[90] D. Pasquariello, J. Piprek, D. Lasaosa, and J. E. Bowers *InP-based Waveguide Photodetector with Integrated Photon Multiplication*, Proc. SPIE Semiconductor Optoelectronic Devices for Lightwave Communication Vol. 5248 pp 258-266 (2003)

[91] G. Roelkens, D. Van Thourhout, and R. Baets, R. Ntzel, and M. Smit *Laser emission and photodetection in an InP/InGaAsP layer integrated on and coupled*

to a Silicon-on-Insulator waveguide circuit, Opt. Exp. Vol. 14, Issue 18 pp 8154-8159 (2006)

[92] T S Moss, G J Burell and B Ellis *Semiconductor Opto-electronics*, Butterworth, London. (1973)

[93] Richard A Soref Brian R Bennett, *Kraemer Kronig Ananlysis of Electro-Optic Switching in Silicon*, SPIE 704 Int. Optical Engineering Circuit IV (1986)

[94] Graham Reed *Silicon Photonics Introduction* John Wiley and Sons (2004)

[95] W Franz Z*Naturforsch* Vol. 13a pp 484 (1958)

[96] Sov. Phys. JETP Vol.7 pp 788 (1958)

[97] E. O. Kane, *Band Structure of Indium Antimonide*, J. Phys. Chem. Solids, Vol. 1, pp. 249261, (1957)

[98] A G Aronov, I V Mochan, V I Zemskii *Influence of electric field on exciton absorption in Ge* Phy.s Stat Sol. B Vol. 45 (1971)

[99] J A V Vechten, D E Aspenes*Franz Keldysh contributions to thrid order optical susceptibilities* Physics Letters. A Vol 30 Issue 6 pp 346-347 (1969)

[100] Yashiko Ishikawa, Kazumi Wada, Doughlas D Cannon, Jifeng Liu, Hsin Chiao Luan, Lionel C Kimerling, *Strain induced band gap shrinkage in Ge grown on Si substrate* Appl. Phys. Lett. Vol 82 issue 13 pp 2044-2046 (2003)

[101] J.M. Hartmann, A.M. Papona, V. Destefanisb, T. Billona, *Reduced pressure chemical vapor deposition of Ge thick layers on Si(0 0 1), Si(0 1 1) and Si(1 1 1)* Journal of Crstal Growth Vol. 310, Issue 24 pp 52875296 (2008)

[102] Jifeng Liu, Rodolfo Camacho-Aguilera, Jonathan T. Bessette, Xiaochen Sun, Xiaoxin Wang, Yan Cai, Lionel C. Kimerling , Jurgen Michel, *Ge-on-Si optoelectronics* Thin Solid Films Vol. 520 Issue 8 pp 33543360 (2012)

[103] Andy Eu-Jin Lim, Tsung-Yang Liow, Fang Qing, Ning Duan, Liang Ding, Mingbin Yu, Guo-Qiang Lo, Dim-Lee Kwong,*Novel evanescent-coupled germanium electro-absorption modulator featuring monolithic integration with germanium p-i-n photodetector*, Opt. Exp. Vol. 19, No. 6 pp 5040-5046 (2011)

[104] Li Ya-Ming, Hu Wei-Xuan, Cheng Bu-Wen, Liu Zhi, Wang Qi-Ming, *Remarkable Franz-Keldysh Effect in Ge-on-Si p-i-n Diodes* Chin. Phys. Lett. Vol. 29, No. 3 pp 034205-1-3 (2012)

[105] Ning-Ning Feng, Shirong Liao, Dazeng Feng, Xin Wang, Po Dong, Hong Liang, Cheng-Chih Kung, Wei Qian, Yong Liu, Joan Fong, Roshanak Shafiiha, Ying Luo, Jack Cunningham, Ashok V. Krishnamoorthy, Mehdi Asghari, *Design and fabrication of 3m silicon-on-insulator waveguide integrated Ge electro-absorption modulator*, Opt. Exp. Vol. 19, Issue 9 pp 8715-8720 (2011)

[106] S. Jongthanmmanurak, J. F. Liu, K. Wada, D. D. Cannon, D. T. Danielson, D. Pan, L. C. Kimeriling J. Michel, *Large electro-optic effect in tensile strained Ge-on-Si films*, Appl. Phys. Lett. Vol 89 Issue 16 pp 34-36 (2006)

[107] Cocorullo G, Iodice M, Rendina I *All-silicon FabryPerot modulator based on the thermo-optic effect*, Opt. Lett. Vol. 19 Issue 6 pp 420-422 (1994)

[108] Lorenzo J P and Soref R A *1.3 m electro-optic silicon switch*, Appl. Phys. Lett. Vol. 51 Issue 1 pp 6-8 (1987)

[109] B. R. Hemenway, O. Solgaard, and D. M. Bloom *All-silicon integrated optical modulator for 1.3 μm fiber-optic interconnects*, Appl. Phys. Lett. Vol. 55, Issue 4, pp 349350 (1989)

[110] G. V. Treyz, P. G. May, and J. M. Halbout *Silicon optical modulator at 1.3 μm based on free-carrier absorption*, IEEE Electron. Device Lett. Vol. 12 Issue 6 pp 276278 (1991)

[111] G. V. Treyz, P. G. May, and J. M. Halbout *Silicon Mach-Zehnder waveguide interferometers based on the plasma dispersion effect*, Appl. Phys. Lett. Vol. 59, Issue 7 pp 771773 (1991)

[112] Michal Lipson *Compact Electro-Optic Modulators on a Silicon Chip*, IEEE Journal of Selected Topics in Quantum Electronics Vol. 12 Issue 6 pp 1520-1526 (2006)

[113] S. M. Weiss, M. Molinari, and P. M. Fauchet, *Temperature stability for silicon-based photonic band-gap structures*, Appl. Phys. Lett. Vol. 83, Issue 10, pp. 19801982 (2003)

[114] Antonello Cutolo, Mario Iodice, Paolo Spirito, Luigi Zeni, *Silicon Electro-Optic Modulator Based on a Three Terminal Device Integrated in a Low-Loss Single-Mode SOI Waveguide*, Journal of Lightwave Technology, Vol. 15, Issue 3 pp 505-518 (1997)

[115] William M. J. Green, Michael J. Rooks, Lidija Sekaric, Yurii A. Vlasov, *Ultra-compact, low RF power, 10 Gb/s silicon Mach-Zehnder modulator*, Opt. Exp. Vol. 15 Issue 25 pp 17106-17113 (2007)

[116] A. Brimont, D. J. Thomson, P. Sanchis, J. Herrera, F.Y. Gardes, J. M. Fedeli, G. T. Reed, J. Mart,*High speed silicon electro-optical modulators enhanced via slow light propagation*, Opt. Exp. Vol. 19, Issue 21, pp 20876-20885 (2011)

[117] Ansheng Liu, Ling Liao, Doron Rubin, Hat Nguyen, Berkehan Ciftcioglu, Yoel Chetrit, Nahum Izhaky, and Mario Paniccia, *High-speed optical modulation based on carrier depletion in a silicon waveguide*, Opt. Exp. Vol 15 Issue 2 pp 660-668 (2007)

[118] Mark Y. Liu, Stephen Y. Chou*High-modulation-depth and short-cavity-length silicon FabryPerot modulator with two grating Bragg reflectors*, Appl. Phys. Lett. Vol. 68 Issue 2 pp 170-172 (1996)

[119] Carlos Angulo Barrios, Vilson Rosa de Almeida, Michal Lipson *Low-Power-Consumption Short-Length and High-Modulation-Depth Silicon Electrooptic Modulator*, Journal of Lightwave Technology, Vol. 21, Issue 4 pp 1089-1098 (2003)

[120] Bradley Schmidt, Qianfan Xu, Jagat Shakya, Sasikanth Manipatruni, Michal Lipson *Compact electro-optic modulator on silicon-oninsulator substrates using cavities with ultrasmall modal volumes*, Opt. Exp. Vol. 15, Issue 6 pp 3140-3148 (2007)

[121] Qianfan Xu, Bradley Schmidt, Sameer Pradhan, Michal Lipson *Micrometre-scale silicon electro-optic modulator*, Nature Lett. Vol. 435 Iss. 19 pp 325-327 (2005)

[122] Guoliang Li, Xuezhe Zheng, Jin Yao, Hiren Thacker, Ivan Shubin, Ying Luo, Kannan Raj, John E. Cunningham, Ashok V. Krishnamoorthy *25Gb/s 1V-driving CMOS ring modulator with integrated thermal tuning*, Opt. Exp. 20435 Vol. 19, Issue 21 pp 20435-20443 (2011)

[123] Qianfan Xu, Brad Schmidt, Jagat Shakya, Michal Lipson *Cascaded silicon microring modulators for WDM optical interconnection*, Opt. Exp. Vol. 14, No. 20 pp 9431-9435 (2006)

[124] Ansheng Liu, Richard Jones, Ling Liao, Dean Samara-Rubio, Doron Rubin, Oded Cohen, Remus Nicolaescu, Mario Paniccia*A high-speed silicon optical modulator based on a metaloxide semiconductor capacitor* Nature Vol. 427 pp 615-618 (2004)

[125] O. Qasaimeh, P. Bhattacharya, *SiGeSi Quantum-Well Electroabsorption Modulators*, IEEE Photonics Tech. Let., Vol. 10 Issue 6 pp 807-809 (1998)

[126] Yu-Hsuan Kuo, Yong Kyu Lee, Yangsi Ge, Shen Ren, Jonathan E. Roth, Theodore I. Kamins, David A. B. Miller, James S. Harris*Quantum-Confined Stark Effect in Ge/SiGe Quantum Wells on Si for Optical Modulators*, IEEE Journal of Selected Topics in Quantum Eelectronics, Vol. 12 Issue 6 pp 1503-1513 (2006)

[127] Jonathan E. Roth, Onur Fidaner, Rebecca K. Schaevitz, Yu-Hsuan Kuo, Theodore I. Kamins, James S. Harris, Jr, and David A. B. Miller *Optical modulator on silicon employing germanium quantum wells*, Opt. Exp. Vol. 15, Issue 9 pp 5851-5859 (2007)

[128] Leon Lever, Zoran Ikonic, Alex Valavanis, Jonathan D. Cooper, Robert W. Kelsall *Design of GeSiGe Quantum-Confined Stark Effect Electroabsorption Heterostructures for CMOS Compatible Photonics*, Journal of lightwave Tech., Vol. 28, Issue 22 pp 3273-3281 (2010)

[129] Chaisakul P, Marris-Morini D, Rouifed MS, Isella G, Chrastina D, Frigerio J, Le Roux X, Edmond S, Coudevylle JR, Vivien L *23 GHz Ge/SiGe multiple quantum well electro-absorption modulator* Opt. Exp. Vol. 20 Issue 3 pp 3219-3224 (2012)

[130] Jifeng Liu, Dong Pan, Samerkhae Jongthammanurak, Kazumi Wada, Lionel C. Kimerling, Jurgen Michel*Design of monolithically integrated GeSi electroabsorption modulators and photodetectors on an SOI platform*, Opt. Exp. Vol. 15, Issue 2 pp 623-628 (2007)

[131] Dazeng Feng, Shirong Liao, Hong Liang, Joan Fong, Bhavin Bijlan, Roshanak Shafiiha, B. Jonathan Luff, Ying Luo, Jack Cunningham, Ashok V. Krishnamoor-

thy, Mehdi Asghari, *High speed GeSi electro-absorption modulator at 1550 nm wavelength on SOI waveguide*, Opt. Exp. Vol. 20, Issue 20 pp 22224-22232 (2012)

[132] J. Gosciniak, S. I. Bozhevolnyi, T. B. Andersen, V. S. Volkov, J. Kjelstrup-Hansen, L. Markey, A. Dereux, *Thermo-optic control of dielectric-loaded plasmonic waveguide components*, Opt. Exp., Vol. 18 Issue 2 pp. 12071216 (2010)

[133] T. Nikolajsen, K. Leosson, and S. I. Bozhevolnyi, *Surface plasmon polariton based modulators and switches operating at telecom wavelengths*, Appl. Phys. Lett., Vol. 85 Issue 24 pp 5833-5835 (2004)

[134] Volker J. Sorger, Norberto D. Lanzillotti-Kimura, Ren-Min Ma, Xiang Zhang, *Ultra-compact silicon nanophotonic modulator with broadband response* Nanophotonics, Volume 1, Issue 1, pp 17-22 (2012)

[135] A. Melikyan, N. Lindenmann, S. Walheim, P. M. Leufke, S. Ulrich, J. Ye, P. Vincze, H. Hahn, Th. Schimme, C. Koos, W. Freude, and J. Leuthold, *Surface plasmon polariton absorption modulator*, Opt. Exp. Vol 19 Issue 9 8855-8869 (2011)

[136] Jennifer A. Dionne, Kenneth Diest, Luke A. Sweatlock, Harry A. Atwater, *PlasMOStor: A Metal Oxide Si Field Effect Plasmonic Modulator* Nano Lett. Vol 9 (2), pp 897902 (2009)

[137] Shiyang Zhu, G. Q. Lo, D. L. Kwong, *Electro-absorption modulation in horizontal metal-insulator-silicon-insulator-metal nanoplasmonic slot waveguides*, Appl. Phys. Lett. Vol. 99 Issue 15 pp 151114-1-3 (2011)

[138] Alexandros Emboras, *CMOS Integration of plasmon field effect devices* PhD. (2012)

[139] Wenshan Cai, Wonseok Shin, Shanhui Fan, Mark L. Brongersma, *Elements for Plasmonic Nanocircuits with Three-Dimensional Slot Waveguides*, Adv. Mater., Vol. 22 Issue 45 pp 51205124 (2010)

[140] Jin Tae Kim, *CMOS-Compatible Hybrid Plasmonic Slot Waveguide for On-Chip Photonic Circuits*, IEEE Phot. Tech. Lett., Vol. 23, No. 20, pp 1481-1483 (2011)

[141] G. Lerosey. *Nano-Optics: Yagi-Uda antenna shines bright*, Nphoton Vol. 4 pp 267-267 (2010)

[142] Orfanidis S J *Electromagnetic waves and Antennas* (2002)

[143] Mark L Brongersma *Plasmonics: Engineering Optical Nanoantennas*, Nphoton. Vol. 2 pp 270-272 (2008)

[144] Bohren C F and Huffman D R, *Absorption and Scattering of Light by Small Particles* vol 1 New York: WileyInterscience (1983)

[145] U. Kreibig, M. Vollmer, *Optical Properties of Metal Clusters* Springer-Verlag, Berlin, (1995)

[146] Mark Brongersma, Peter Kik *Surface Plasmon Nanophotonics*, Springer series in Optical Sciences (2007)

[147] Bharadwaj P, Deutsch B, Novotny L. *Optical antennas* Adv Opt Photon Vol. 1, Issue 3 pp 438-483 (2009)

[148] Novotny L. *Effective wavelength scaling for optical antennas.* Phys Rev Lett, Vol. 98 Issue 26 pp 266802 4, (2007)

[149] Yamaguchi T, Yoshida S and Kinbara A *Optical effect of the substrate on the anomalous absorption of aggregated silver films*, Thin Solid Films Vol. 21 Issue 1 pp 173 187 (1974)

[150] Tae Joon Seok, Arash Jamshidi, Myungki Kim, Scott Dhuey, Amit Lakhani, Hyuck Choo, Peter James Schuck, Stefano Cabrini, Adam M. Schwartzberg, Jeffrey Bokor, Eli Yablonovitch, Ming C. Wu, *Radiation Engineering of Optical Antennas for Maximum Field Enhancement* Nano Lett., 11, pp 2606 2610, (2011)

[151] Huifeng Li and Xing Chenga *Optical antennas: A boost for infrared detection*, J. Vac. Sci. Tech. B Vol 26 Issue 6 pp 2156-2159 (2008)

[152] Jessie Rosenberg, Rajeev V. Shenoi, Thomas E. Vandervelde, Sanjay Krishna, Oskar Painter*A multispectral and polarization-selective surface-plasmon resonant midinfrared detector* Appl. Phys. Lett. 95, 161101 (2009)

[153] Lee S.C. Krishna S., Brueck S.R.J., *Plasmonic-Enhanced Photodetectors for Focal Plane Arrays* Phot. Tech. Lett., IEEE Vol. 23 Issue 7 pp 935-937 (2011)

[154] J. Le Perchec, Y. Desieres, R. Espiau de Lamaestre, *Plasmon-based photosensors comprising a very thin semiconducting region*, Appl. Phys. Lett. Vol. 94, Issue 18 pp 181104-1-3 (2009)

[155] S. C. Lee, S. Krishna, and S. R. J. Brueck, *Plasmonic-Enhanced Photodetectors for Focal Plane Arrays*, IEEE Phot. Tech. Lett. Vol. 23, No. 14, 935-937 2011

[156] Liang Tang, Sukru Ekin Kocabas, Salman Latif, Ali K. Okyay, Dany-Sebastien Ly-Gagnon, Krishna C. Saraswat, David A. B. Miller *Nanometre-scale germanium photodetector enhanced by a near-infrared dipole antenna*, Nphoton Vol. 2, pp 226-229 (2008)

[157] Fang-Fang Ren, Kah-Wee Ang, Jiandong Ye, Mingbin Yu, Guo-Qiang Lo, Dim-Lee Kwong, *Split Bulls Eye Shaped Aluminum Antenna for Plasmon-Enhanced Nanometer Scale Germanium Photodetector*, Nano Lett., 11, pp 1289 1293, (2011)

[158] G. Katsaros, P. Spathis, M. Stoffel, F. Fournel, M.Mongillo, V. Bouchiat, F. Lefloch, A. Rastelli, O. G. Schmidt, S. De Franceschi, *Hybrid superconductor semiconductor devices made from self-assembled SiGe nanocrystals on silicon*, Nature Nanotech. Vol. 5 pp 458-464 (2010)

[159] J. Konle, H. Presting, H. Kibbel, K. Thonke, R. Sauer *Enhanced performance of silicon based photodetectors using silicon/germanium nanostructures*, Solid-State Electronics Vol. 45 Isue 11 pp 1921-1925 (2001)

[160] M. Elkurdi, P. Boucaud, S. Sauvage, O. Kermarrec, Y. Campidelli, D. Bensahel, G. Saint-Girons, I. Sagnes, *Near-infrared waveguide photodetector with Ge/Si self-assembled quantum dots*, Appl. Phys. Lett. Vol. 80 Issue 3, pp 509-511 (2002)

[161] A. Elfving, G. V. Hansson *SiGe (Ge dot) heterojunction phototransistors for efficient light detection at 1.3-1.55 μm* Physica E Vol. 16 No. 3 pp 528-532 (2003)

[162] A. I. Yakimov, A. V. Dvurechenski, V. V. Kirienko, N. P. Stepina, A. I. Nikiforov, V. V. Ulyanov, S. V. Chakovski, V. A. Volodin, M. D. Efremov, M. S.

Seksenbaev, T. S. Shamirzaev, and K. S. Zhuravlev, *Ge/Si Waveguide Photodiodes with Built-In Layers of Ge Quantum Dots for Fiber-Optic Communication Lines* Semiconductors, Vol. 38, No. 10, pp. 12251229 (2004)

[163] Shi Wen-Hua, Mao Rong-Wei, Zhao Lei, Luo Li Ping, Wang Qi-Ming, *Fabrication of Ge Nano-Dot Heterojunction Phototransistors for improved light Detection at 1.55vμm*, Chinese Physical Letters Vol. 23, No.3 pp 735-737 (2006)

[164] A. Elfving, A. Karim, G. V. Hansson, and W.-X. Ni *Three-terminal Ge dot/SiGe quantum-well photodetectors for near-infrared light detection*, Appl. Phys. Lett. 89, pp 083510-1-3 (2006)

[165] E. Castani, R. Vincent, R. Pierrat, and R. Carminati, *Absorption by an Optical Dipole Antenna in a Structured Environment* International Journal of Optics Vol. 2012 (2011)

[166] Dmitri K. Gramotnev, Anders Pors, Morten Willatzen, Sergey I. Bozhevolnyi, *Gap-plasmon nanoantennas and bowtie resonators* Phys. Rev. B Vol. 85, Issue 4 pp 045434-1-9 (2012)

[167] Palik: *Handbook of Optical Constants*, Vol 2 April 4 1991

[168] P. J. Schuck, D. P. Fromm, A. Sundaramurthy, G. S. Kino, and W. E. Moerner *Improving the Mismatch between Light and Nanoscale Objects with Gold Bowtie Nanoantennas*, Phys. Rev. Lett. Vol. 94,Issue 1 pp 017402-1-4 (2005)

[169] Yu-Ming Wu, Le-Wei Li, Bo Liu, *Optical Resonance of Nanometer Scale Bow-tie Antenna and Bow-tie Shaped Aperture Antenna*, 978-1-4244-2802-1 IEEE (2009)

[170] S. Sederberg and A. Y. Elezzabi, *Nanoscale plasmonic contour bowtie antenna operating in the mid-infrared* Opt. Exp., Vol. 19, Issue 16, pp 15532-15537 (2011)

[171] W. Zhong Y.Wang R. He X. Zhou, *Investigation of plasmonics resonance infrared bowtie metal antenna*, Appl Phys B Vol 105 Issue 2 pp 231-237 (2011)

[172] Dmitri K. Gramotnev, Anders Pors, Morten Willatzen, Sergey I. Bozhevolnyi, *Gap-plasmon nanoantennas and bowtie resonators*, Physical Review B 85, 045434 (2012)

[173] Wei Ding, Renaud Bachelot, Sergei Kostcheev, Pascal Royer, and Roch Espiau de Lamaestre, *Surface plasmon resonances in silver Bowtie nanoantennas with varied bow angles*, Journal of Appl. Phys. 108, 124314, (2010)

[174] Yoshito Tanaka, Akio Sanada, Keiji Sasaki, *Nanoscale interference patterns of gap-mode multipolar plasmonic fields*, Nature Scientific Reports, July (2012)

Abstract

Interest in the field of plasmonics has been primarily driven by the need to guide and confine light in the subwavelength scale. The past few years has witnessed a huge interest in this field largely due to the may advances that have occured in nanofabrication techniques. The field of plasmonics is often touted as the next generation platform that could interface nanoscale electronics and Si photonics.

With current electronic systems nearing saturation, the migration to photonic systems would become inevitable. Crucial to achieving this integration is to design reliable plasmonic components within nanophotonics circuits. This however requires an accurate estimation of the electromagnetic response of these components. Numerical modeling tools are one way to gauge this response.

By and large the thesis deals with numerically analysing the propagation and near field characteristics of plasmon based components for Si photonics. The two principal EM modelling tools used in this regard are the boundary element method as well as the finite difference time domain. Two main kind of active plasmonic active devices were investigated: integrated modulators, and free space radiation photodetectors. The critical issue of an efficient coupling of light into a very confined guided plasmonic mode was first investigated so as to isolate the main modal governing contributions. Next, a new structure of plasmon assisted modulator was proposed and a complete optical design taking into the technological constraints of a CMOS foundry is provided and discussed.

Finally a design optimizing the radiative coupling to the absorption of a Ge dot, using a plasmonic dipolar antenna, is studied. In particular the radiative engineering of the supporting SOI substrate is shown to have a tremendous effect on the final performance of the device.

Résumé

Bien que les propriétés optiques des métaux nanostructurés soit connues depuis de nombreuses décennies, ce n'est que dans les dernières années que ce domaine a suscité un grand intérêt. Ceci est en partie dû aux nombreux progrès des techniques de nanofabrication. Le domaine de la plasmonique est souvent présentée comme la support de la prochaine génération de dispositifs de traitement de l'information, mélageant la nanoélectronique et la photonique silicium pour obtenir des disposotifs plus performants.

Les systèmes microélectroniques actuels approchant de la saturation en terme de bande passante et de consomation énergétique, la migration vers les systèmes photoniques semble inévitable. La prédiction de la réponse électromagnétique de ces composants nano-photoniques est essentiels au succès de leur intégration réaliste. Les outils numériques de simulation électromagnétiques sont le moyen par excellence de calculer précisement er de manière réaliste les propriétés optiques de composants nanophotoniques, et en particulier ceux utilisant des plasmons de surface.

Ce travail de thèse rend compte de l'analyse numérique de la propagation et des caractéristiques de champ proche de composants à base de plasmons pour la photonique en technologie CMOS. Les deux principaux outils de modélisation EM utilisés à cet égard sont la méthode des éléments des moments, ainsi que la FDTD. Deux types principaux de dispositifs actifs plasmoniques actifs ont été étudiés : d'une part les modulateurs électro-optiques intégrés et d'autre part des détecteurs à base de quantum dot de Ge, le tout dans la gamme du proche infrarouge. La question cruciale d'un couplage efficace de la lumière dans un mode très confiné plasmonique a d'abord été étudiée de manière à isoler la part modale des principales contributions. Ensuite, une nouvelle structure de modulateur assisté plasmon a été proposée et une conception optique complète prenant en compte les contraintes technologiques d'une fonderie CMOS est proposée et discutée.

Enfin une conception optimisée du couplage radiatif de l'absorption d'un point de Ge, en utilisant une antenne dipolaire plasmonique, est étudiée. En particulier, l'ingénierie radiative du substrat SOI permet de démontrer un effet considérable sur la performance finale du dispositif.